

Chapter 1

The QCD phase diagram and Beam Energy Scan physics: a theory overview

Lipei Du,^{1,2*} Agnieszka Sorensen,^{3†} and Mikhail Stephanov^{4,5‡}

¹*Department of Physics, McGill University, Montreal, Quebec H3A 2T8, Canada*

²*Nuclear Science Division, Lawrence Berkeley National Laboratory, Berkeley, CA 94270, USA*

³*Institute for Nuclear Theory, University of Washington, Seattle, WA 98195, USA*

⁴*Department of Physics and Laboratory for Quantum Theory at the Extremes, University of Illinois, Chicago, IL 60607, USA*

⁵*Kadanoff Center for Theoretical Physics, University of Chicago, Chicago, Illinois 60637, USA*

We review recent theoretical developments relevant to heavy-ion experiments carried out within the Beam Energy Scan program at the Relativistic Heavy Ion Collider. Our main focus is on the description of the dynamics of systems created in heavy-ion collisions and establishing the necessary connection between the experimental observables and the QCD phase diagram.

Contents

1. Introduction	2
2. Multistage description of bulk dynamics	5
2.1. Prehydrodynamic stage	5
2.2. Hydrodynamics with multiple conserved charges	14
2.3. Freeze-out and particlization	34
2.4. Hadronic afterburner	43
3. Microscopic transport description of dense nuclear matter dynamics	48
3.1. Selected prominent observables for extracting the equation of state	51
3.2. Microscopic transport models	59

*lpei.du@mail.mcgill.ca

†amsorens@uw.edu

‡misha@uic.edu

3.3. Recent developments relevant to constraining the dense nuclear matter equation of state	66
3.4. Constraints on the equation of state	81
4. Fluctuations: critical point, hydrodynamics, freeze-out	88
4.1. Fluctuations in thermodynamics, critical fluctuations	89
4.2. Fluctuations in hydrodynamics	93
4.3. Freeze-out of fluctuations and observables	101
5. Summary and outlook	107
References	108

1. Introduction

Quantum Chromodynamics (QCD) is a non-abelian gauge theory describing a vast range of the strong interaction phenomena using a tight set of fundamental principles. However, extracting theoretical predictions from QCD is remarkably difficult due to the non-perturbative nature of the dominant fundamental strong interaction phenomena: quark and gluon confinement and spontaneous chiral symmetry breaking. One of the most challenging and still open questions is the full structure of the QCD phase diagram at finite temperature and finite baryon density, a tentative sketch of which is shown in Fig. 1. The exploration of the QCD phase diagram proceeds along several intertwined directions.

On the purely theoretical side, the most prominent approach is based on first-principle lattice calculations. While the equation of state (EOS) at finite temperature and *zero* chemical potential can be reliably calculated, the notorious sign problem prevents lattice simulations from extending this first-principle method to *finite* baryon density. The recent advances and challenges in this area of the QCD phase diagram research, covered in reviews such as Ref. ¹ are not within the scope of this chapter. Among other theoretical attempts to shed light on the QCD phase diagram are microscopic approaches such as the Functional Renormalization Group (FRG)² as well as various calculations based on models as simple as the Random Matrix Model (RMM)³ or Nambu–Jona-Lasinio (NJL) models^{4,5} and as sophisticated as models based on applications of gauge-gravity (or AdS/CFT) duality to QCD.⁶

Experiments involving heavy-ion collisions can be utilized to explore the QCD EOS and phase diagram. By colliding heavy nuclei at center-of-mass energies per nucleon pair, $\sqrt{s_{NN}}$, ranging from a few GeV to a few TeV, one can scan and explore the range of temperatures and baryon chemical potentials where the most theoretically challenging phenomena associated with the transition between the two major QCD phases — the

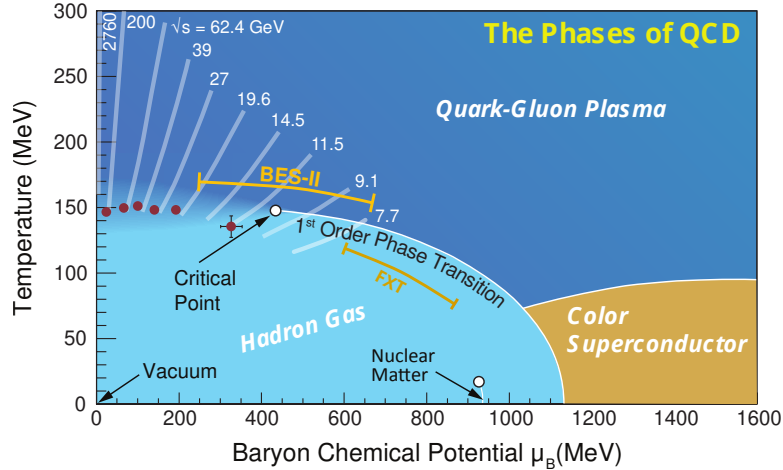


Fig. 1.: The QCD phase diagram as conjectured based on the current understanding. Red circles mark the location of freeze-out points determined experimentally. Trajectories followed by hydrodynamically expanding matter in the fireball are indicated schematically by white lines. These trajectories are labeled by the initial collision energies $\sqrt{s_{NN}}$ in GeV, demonstrating how a beam-energy scan translates into the scan of the QCD phase diagram. The range covered by the second phase of the Beam Energy Scan program is marked as “BES-II” (collider mode) and “FXT” (fixed target). Figure modified from Ref.⁷

Quark-Gluon Plasma (QGP) and Hadron Resonance Gas (HRG) — occur (see Fig. 1). Another avenue for exploration of the QCD phase diagram has been recently opened by gravitational wave observations of neutron star mergers.^{8,9} While, in contrast to laboratory experiments, these natural phenomena cannot be planned or controlled, they have the advantage of probing the QCD phase diagram in the regime complementary to that explored by heavy-ion collisions, that is at high baryon densities and low temperatures as well as at substantial isospin fractions.

The ultimate goal of research centered on the QCD phase diagram is to determine the QCD EOS quantitatively. In using heavy-ion collision experiments to explore the QCD phase diagram, the challenge for theory is predicting the experimental signatures of the phenomena associated with the QCD phase structure and interpreting experimental observations in terms of the QCD EOS. The task of connecting theory and experiment is

the main focus of this review.

One question central to our understanding of the QCD phase diagram is the existence and the location of the QCD critical point, see Fig. 1. This point anchors the expected first-order phase transition separating the QGP and HRG phases of QCD. Discovering this QCD first-order phase transition has been a key objective of heavy-ion collision research since its inception. It is now understood, largely due to lattice calculations, that such a discontinuous transition does not take place at zero baryon chemical potential, $\mu_B = 0$. Instead, at $\mu_B = 0$, the transition between the two phases happens gradually, or smoothly, *via* a crossover at a temperature of approximately 150–160 MeV, as shown in Fig. 1. While lattice calculations are unfortunately impeded by the sign problem, most theoretical approaches — from RMM to FRG to AdS/CFT — consistently indicate that the transition becomes discontinuous above a certain critical baryon chemical potential, where, by definition, the QCD critical point is located.

Heavy-ion collisions have the potential to answer the question of the existence of the QCD critical point and to determine its location by scanning the QCD phase diagram *via* varying the crucial experimental control parameter: the beam energy, or the center-of-mass collision energy per nucleon pair $\sqrt{s_{NN}}$, as shown in Fig. 1. This is the major motivation behind the Beam Energy Scan (BES) program at the Relativistic Heavy Ion Collider (RHIC).

The basic theoretical strategy for translating the experimental measurements into the knowledge of the QCD phase diagram is as follows.¹⁰ Using a putative QCD EOS one can describe the evolution of the hot and dense system created in heavy-ion collisions — the fireball — which expands and cools hydrodynamically and then breaks up, or freezes out, into observed particles. The predicted multiplicities as well as their fluctuations and correlations depend on the EOS. Establishing this dependence theoretically allows one to connect experimental observations to the QCD EOS. This is not a simple task due to the highly dynamic nature of the collisions, and this chapter will cover several key ingredients needed to complete it. We briefly outline these ingredients below.

For heavy-ion collisions at intermediate and high energies, the system's evolution is captured by multistage hydrodynamic simulations. This includes modeling various stages such as the initial collision, hydrodynamic expansion of the fireball, the transition from thermodynamic degrees of freedom to particles, and the inclusion of hadronic rescatterings. These aspects will be discussed in Section 2.

At low collision energies, microscopic degrees of freedom play a prominent role in the dynamics which proceeds out-of-equilibrium for substantial fractions of the evolution time. Modeling heavy-ion collisions in this regime, which probes the highest density regions of the QCD phase diagram available in laboratory experiments, is the subject of Section 3.

Finally, many experimental signatures of the QCD critical point are based on fluctuation and correlation phenomena. The description of fluctuations in a dynamical environment characteristic of relativistic heavy-ion collisions and, importantly, the translation of hydrodynamic fluctuations into fluctuations of observables has been developed only recently, as discussed in Section 4.

We aim to cover recent and ongoing developments in these areas and hope this chapter will serve as a comprehensive yet concise guide for researchers engaged or planning to engage in the subject.

2. Multistage description of bulk dynamics

Heavy-ion collisions generate highly dynamic systems undergoing various phases. Multistage descriptions, incorporating diverse physics, have become the “standard model” for characterizing these collisions.^{11–18} A crucial aspect is the quantitative understanding of bulk dynamics, representing the final soft hadrons with transverse momenta below 3 GeV/c (constituting more than 99% of all particles produced in the collisions). This understanding forms the foundation for exploring other facets of heavy-ion physics, including critical phenomena,^{19,20} hard probes,²¹ and electromagnetic probes.^{22–26} Previous comprehensive reviews on multistage descriptions with hydrodynamics as a core can be found in Refs.^{27–29} Here, we focus on recent theoretical developments related to Beam Energy Scan (BES) physics for collisions at $\sqrt{s_{NN}} \gtrsim 7$ GeV, with particular attention to considerations of finite charge densities. It is important to note that there are also microscopic descriptions, such as JAM,³⁰ PHSD,^{31,32} EPOS,³³ AMPT,³⁴ SMASH,³⁵ UrQMD,^{36,37} and PHQMD,³⁸ which are not covered in this section. Among these, the pure hadronic descriptions hold particular significance for low-energy collisions at $\sqrt{s_{NN}} \lesssim 7$ GeV, as discussed in Sec. 3.

2.1. Prehydrodynamic stage

During the initial phase in a heavy-ion collision, the two colliding nuclei first penetrate each other, and, subsequently, the produced system un-

dergoes hydrodynamization—a phase referred to as the prehydrodynamic stage. During this stage, the nucleons or partons initially at beam rapidity (y_b) undergo collisions that result in the loss of some of their initial energy and longitudinal momentum. This lost energy and momentum contribute to the formation of the quark-gluon plasma. As these particles collide and lose energy and longitudinal momentum, their rapidities shift away from the beam rapidity and distribute continuously within the range from beam rapidity to midrapidity. Additionally, the charges, including baryon number, strangeness, and electric charge, carried by the partons also undergo redistribution processes during this phase.^a A deep understanding of the energy loss and charge stopping mechanisms plays a pivotal role in determining the initial distributions of quantities such as energy density, flow velocity, and baryon density. These initial conditions serve as the foundation for the entire subsequent evolution of the collision, making this stage the fundamental basis for comprehending the overall dynamic evolution of a heavy-ion collision.³⁹

In ultra-relativistic collisions, the energy deposition is often modeled using the Glauber model.⁴⁰ The model is based on the assumption that each nucleon or parton can either participate in a collision or remain a spectator. The determination of whether nucleons or partons interact is governed by probabilistic considerations based on collision geometry and cross sections. In ultra-relativistic scenarios, the colliding nuclei are significantly Lorentz-contracted in the beam direction. Consequently, it is reasonable to assume that all collisions happen nearly instantaneously. The subsequent expansion in the longitudinal direction is assumed to be boost-invariant and undergo the so-called Bjorken expansion.⁴¹ In this scenario, it is common to model a (2+1)-dimensional system and analyze the observables measured at midrapidity. In practice, when building the initial transverse energy or entropy distribution, an overall normalization factor is often adjusted to match the measured charged particle multiplicity around midrapidity. Moreover, the baryon density is routinely assumed to be negligible in this region, as it is predominantly occupied by partons with small x -values, primarily composed of gluons.

However, when we consider heavy-ion collisions at the BES and lower energies, the dynamics of the initial stage become considerably more intricate. This complexity becomes evident when we examine the overlap

^aBaryon, strangeness, and electric charges are key observables in heavy-ion collisions owing to their conservation laws and their relevance to the study of strong and electromagnetic interactions and the properties of the QGP.

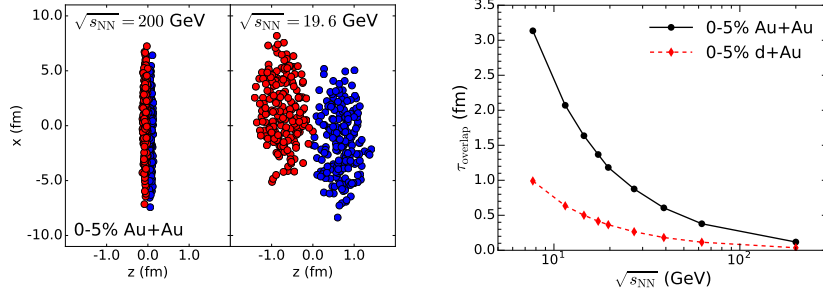


Fig. 2.: *Left*: Nucleon positions plotted against transverse (x) and longitudinal (z) coordinates for two distinct collision energies. Note that the thickness in z at 19.6 GeV is visually exaggerated due to the aspect ratio of the plot. *Right*: The nuclear overlapping time for 0-5% central d+Au and Au+Au collisions depicted as a function of collision energy. Figures from Ref.⁴²

time⁴² between the two colliding nuclei in the center-of-mass frame, which is determined by the formula:

$$t_{\text{overlap}} = \frac{2R}{\gamma v_z} = \frac{2R}{\sinh(y_b)}. \quad (1)$$

Here, R is the radius of the colliding nuclei, $\gamma = 1/\sqrt{1-v_z^2}$ represents the Lorentz contraction factor, and y_b is the beam rapidity, calculated as $y_b = \text{arccosh}(\sqrt{s_{NN}}/(2m_p))$. As collision energy decreases, the overlap time significantly extends and may even become comparable to the duration of the QGP stage (see Fig. 2). Consequently, in such scenarios, the collision locations in space and time vary considerably, necessitating the construction of dynamic, (3+1)-dimensional initial conditions. Moreover, it's important to note that the net baryon number is non-zero and highly non-uniform, as evidenced by the experimentally measured varied distribution of net proton yields in rapidity.⁴³ Therefore, it becomes imperative to model the initial distributions of baryon charge as an integral aspect of the initial conditions. At present, the primary challenge in constructing (3+1)-dimensional dynamic initial conditions lies in the lack of a comprehensive understanding of the mechanisms governing baryon stopping and energy deposition during this prehydrodynamic phase. This, in turn, makes the extraction of hydrodynamic transport coefficients from experimental measurements an extremely difficult task.

2.1.1. *Parametric initial conditions*

A straightforward yet effective approach to address the previously mentioned challenges is the use of parametric initial conditions. This method often involves supplementing transverse distributions with longitudinally parametrized profiles. The transverse distributions of energy or entropy and baryon densities are typically derived from nuclear thickness functions through Glauber-like models, while the longitudinal profiles are parametrized to account for specific observables sensitive to longitudinal bulk dynamics, such as longitudinal decorrelation and rapidity-dependent identified particle yields. These initial conditions are employed in subsequent hydrodynamic evolution at a specific initial time (τ_0), and the initial longitudinal flow is initiated as Bjorken flow. These models become less reliable at lower beam energies, where the overlap time is long and the Bjorken boost-invariant approximation becomes less appropriate. However, they retain their strength in a different way by enabling the identification of favored longitudinal profiles from experimental data more cleanly, compared to dynamical models with stochastic fluctuations. These extracted profiles can provide valuable insights into the mechanisms of energy deposition and baryon stopping.

For symmetric collision systems, the initial energy or entropy density in spacetime rapidity is often parametrized using a plateau-like function. This function is flat around midrapidity and smoothly transitions to half of a Gaussian function in the forward and backward spacetime rapidity (η_s) regions.^{44–48} These initial profiles are tuned to match the measured charged particle multiplicity in pseudorapidity (η), while the resulting profile can be influenced by various factors in the subsequent hydrodynamic evolution, such as the equation of state, initial time, and shear viscosity.^{49–51}

It was later recognized that the presence of a nonzero directed flow of charged particles, $v_1^{\text{ch}}(\eta)$, indicates the need to break symmetry in the reaction plane. This can be achieved by introducing asymmetry in either the initial flow or the initial density, or in both.⁵² The underlying reason for this is that the left- and right-going participants within the projectile and target at a given point in the transverse plane possess an imbalance in momentum, resulting in a nonzero total longitudinal momentum. To account for this total longitudinal momentum, a shift in the longitudinal density profile, as seen in the shifted initial densities, was introduced.⁴⁸ However, this shifted initial profile was found to yield a $v_1^{\text{ch}}(\eta)$ with an incorrect dependence on rapidity.⁵² Nevertheless, a recent study that im-

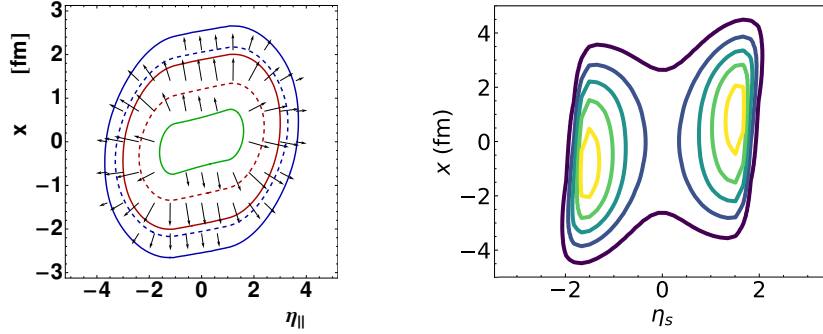


Fig. 3.: Parametric initial distributions for *left*: energy density⁵² and *right*: baryon density⁵⁶ in the reaction plane.

posed local energy-momentum conservation by introducing a similar shift can generate correct rapidity-dependent v_1 for pions.⁵³ Furthermore, the authors also introduced an initial longitudinal flow velocity in addition to the shift in initial energy density to ensure local energy-momentum conservation. Their findings indicated that a concurrent explanation of both the global polarization of the Λ hyperon and the slope of the pion's directed flow $v_1^\pi(y)$ can substantially constrain the longitudinal flow at the initial stages of hydrodynamic evolution.^{54,55}

An alternative category of initial conditions considers a preference for gluon emission near the rapidity of the participant nucleon.⁵² For example, in this framework, nucleons from the projectile with positive rapidity emit more gluons in the forward rapidity regions than in the backward regions.^{57–60} The initial energy density is constructed as a sum of contributions from both forward- and backward-moving participant nucleons, and possibly binary collisions that are assumed to contribute symmetrically. This discrepancy in forward and backward emission results in a tilt of the source within the reaction plane (see the left panel of the Fig. 3), breaking symmetry in the longitudinal direction and generating directed flow $v_1(y)$ with a negative slope around midrapidity for charged particles and mesons. The asymmetric deposition of entropy also results in a rapidity-dependent orientation for the event plane angle,⁶¹ making it useful for exploring longitudinal decorrelation.^{62,63} Such tilted initial conditions continue to be widely used in current studies on directed flows.^{56,64,65} Initial conditions that aim for realistic event-by-event simulations, like the TRENTo 3D model,^{66,67} build upon similar ideas of extending two-dimensional transverse profiles around midrapidity⁶⁸ with the inclusion of longitudinal pro-

files.

The initial profile of baryon density has received considerably less attention in the community. This could be attributed to several factors, with two notable ones as follows: From an experimental standpoint, investigating baryon charge necessitates the measurement of baryons' excess over antibaryons (typically, proton and antiproton), which requires particle identification. This, in turn, leads to a limited number of available measurements for studying the longitudinal baryon profile. On the theoretical side, investigating the evolution of the baryon distribution significantly adds to the complexity of simulations. The initial longitudinal baryon profile is parametrized as the sum of two Gaussian functions with peaks symmetrically centered around midrapidity.^{45,47,69} This parametrization is motivated by the double-humped structure observed in the net-proton yields in rapidity. In some cases, experimentalists employ a similar approach by fitting the net proton yields with the sum of two Gaussian functions, enabling them to reconstruct the entire distribution (see, e.g., Ref.⁷⁰). In recent studies, similar initial baryon profiles are still commonly used, while the Gaussian function associated with the projectile or target has been generalized into an asymmetric Gaussian function.^{53-55,71-73} This function features a peak with half-Gaussian functions on each side, and it allows for asymmetric widths and thereby enhances flexibility.

The baryon profile described above can easily reproduce the double-humped net proton yields in rapidity. However, it tends to yield a $v_1(y)$ with a notably positive slope, and its magnitude significantly exceeds experimental measurements.⁵³ This occurs because the directed flow of baryons is primarily due to the initial asymmetric baryon distribution with respect to the beam axis driven by the transverse expansion.⁵⁶ To tackle this problem, Ref.⁵⁶ introduced an additional rapidity-independent plateau component within the baryon profile (see the right panel of Fig. 3).⁵⁶ This component symmetrically contributes to the baryon density with respect to the beam axis in the reaction plane, resulting in a substantial reduction in $v_1(y)$ magnitude for baryons while effectively reproducing the net proton yields. With this component, the authors found that the primary characteristic features of $v_1(y)$ are naturally explained, including the sign change in the slope of $v_1(y)$ around midrapidity. The inclusion of a plateau component in the baryon profile implies a new baryon stopping mechanism, which can possibly be attributed to the string junction conjecture.^{74,75} Other studies also exist intending to understand the splitting of proton-antiproton directed flow by adjusting the initial baryon profile.^{65,76}

2.1.2. Dynamical initialization

As previously discussed and evident in Fig. 2, collisions occurring at center-of-mass energies in the range of tens of GeV and below exhibit long overlapping time due to reduced Lorentz contraction of the colliding nuclei and, consequently, spacetime-dependent interactions among nucleons or partons. This phenomenon results in different regions of the fireball “hydrodynamizing” at various times. Thus, transitioning to a hydrodynamic description inherently necessitates a (3+1)-dimensional dynamical initial condition. The application of this approach was initially explored during the SPS era.^{77,78} Recently, there has been a resurgence in the development of more intricate models aimed at achieving quantitative simulations for collisions at BES.^{42,79–82}

In this dynamical initialization approach, a spacetime-dependent transition occurs from a microscopic partonic description to a macroscopic hydrodynamic one once certain criteria are met, such as reaching a specified energy density. Throughout this transition, conservation laws persist for energy-momentum and charges accounting for contributions from both the partons and the subsequent fluid. Expressed through the local conservation laws for energy-momentum and conserved charges, the following dynamical initialization equations can be obtained:

$$\partial_\mu T_{\text{fluid}}^{\mu\nu}(x) = J_{\text{source}}^\nu(x) \equiv -\partial_\mu T_{\text{part}}^{\mu\nu}(x), \quad (2)$$

$$\partial_\mu N_{\text{fluid}}^\mu(x) = \rho_{\text{source}}(x) \equiv -\partial_\mu N_{\text{part}}^\mu(x), \quad (3)$$

where J_{source}^ν and ρ_{source} represent the *dynamical sources* contributed by the partons to the fluid.^b These equations illustrate that, as collisions occur among partons, additional energy-momentum and charges (represented by J_{source}^ν and ρ_{source}) are deposited into the fluid. This leads to a progressive increase in the densities of the fluid component within the collision fireball during the prehydrodynamic stage. On average, these densities peak once the collisions conclude, marking the transition to a purely hydrodynamic description (see Fig. 4).

Implementing Eqs. (2, 3) practically involves constructing $J_{\text{source}}^\nu(x)$ and $\rho_{\text{source}}(x)$ or continuous $T_{\text{part}}^{\mu\nu}(x)$ and $N_{\text{part}}^\mu(x)$ from discrete partons. This construction requires modeling collision dynamics, which encompasses energy or rapidity loss, typically described by stochastic processes during collisions. The energy loss of colliding partons carrying baryon charges

^bThis resembles modeling how the medium responds when energetic partons traverse through it in some studies focused on jet-medium interactions.

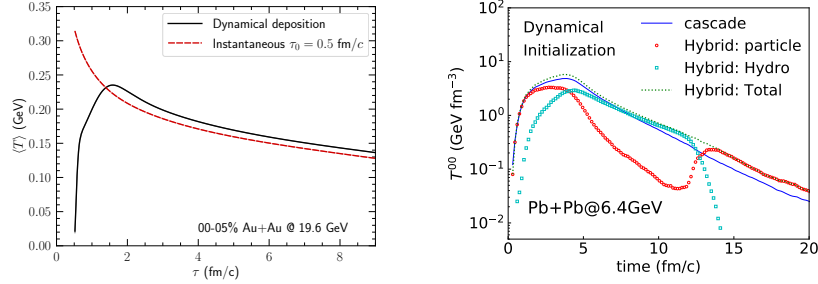


Fig. 4.: *Left:* Time evolution of the averaged temperature in Au+Au collisions at $\sqrt{s_{NN}} = 19.6$ GeV for both dynamical initialization and instantaneous hydrodynamization scenarios.²⁶ *Right:* Time evolution of the energy density from JAM hybrid simulations in central Pb+Pb collisions at $\sqrt{s_{NN}} = 6.4$ GeV.⁸¹ Circles represent the contribution from particles, while squares represent the fluid contribution to the energy density.

might contribute to initial baryon stopping, thereby correlating energy deposition with baryon stopping. Understanding these mechanisms involves phenomenological studies, as these processes are not clear from first principles. Modeling these mechanisms often draws insights from longitudinal profiles preferred by experimental measurements used in parametric initial conditions discussed in Sec. 2.1.1. These mechanisms are significant in grasping baryon fluctuations during the initial stage, which contribute to measured proton cumulants and thus are pivotal for their interpretation.⁴²

Recent advances in dynamical initialization have encompassed diverse approaches like color string dynamics^{42,79} and transport models such as UrQMD⁸⁰ and JAM.⁸¹ We note that these approaches are unable to elucidate the mechanisms of thermalization^{83,84} or even hydrodynamization. The criteria for the time-dependent transition between initial conditions and hydrodynamics are somewhat ad hoc. Nevertheless, these methods are crucial for comprehending boost-noninvariant dynamics and establishing correlations between rapidities in both coordinate and momentum spaces during the prehydrodynamic stage.^{42,79,85,86} Such correlations are often oversimplified in parametric initial conditions that assume Bjorken flow, where the rapidity (y) is equated with the spacetime rapidity (η_s). The non-Bjorken prehydrodynamic flows can significantly impact the subsequent hydrodynamic evolution and thus warrant a more thorough investigation. Additionally, the nontrivial impact of initial dissipative effects on the system's evolution through the phase diagram should also be investigated (see

Sec. 2.2.3).

There is another category of initial conditions that incorporate longitudinal dependence, yet the transition to hydrodynamics occurs at a fixed time. For instance, some studies utilize initial conditions derived from transport models, including UrQMD,^{15,87} SMASH,⁸⁸ and AMPT.⁸⁹ The exploration of baryon or energy stopping has also been conducted using Color Glass Condensate approaches,^{90–92} holographic approaches,^{93–96} and the parton-based Gribov-Regge model NEXUS.^{97,98} These models offer more intricate longitudinal distributions than parametric ones while maintaining a fixed-time transition to hydrodynamics, thereby avoiding the complexity of a dynamical initialization scheme.

Hydrodynamic descriptions with dynamical sources find various applications on diverse topics. The three-fluid hydrodynamic model^{99–102} characterizes interactions among the fluids of the target, projectile, and fireball via friction terms, which serve a comparable role to the dynamical source terms. The utilization of Eqs. (2, 3) extends beyond modeling the prehydrodynamic stage in nuclear collisions at lower beam energies. They have been utilized in various contexts, including modeling core-corona interactions^{103,104} and investigating the impact of mini-jets on the bulk dynamics.^{105,106}

Expanding initial conditions from 2-dimensional transverse distributions at a fixed time to a (3+1)-dimensional framework encompassing both time and rapidity dependence presents considerable challenges, yet ongoing advancements show promise. This extension is crucial for laying the foundational groundwork to understand the thermodynamic and transport properties of QCD matter at finite chemical potentials created in Beam Energy Scan collisions. Comprehensive understanding hinges on rapidity-dependent measurements, including crucial observables like identified particle yields, anisotropic flow coefficients, event plane decorrelation, and Hanbury-Brown-Twiss (HBT) interferometry. Additionally, 3-dimensional jet tomography serves as a means to scrutinize the longitudinal structure of initial conditions.^{107,108} A systematic exploration across various measurements in rapidity, covering a range of collision centralities, beam energies, and system sizes, becomes imperative. Such an analysis is critical to evaluate which description of the initial state yields a more coherent and comprehensive explanation for various available rapidity data.

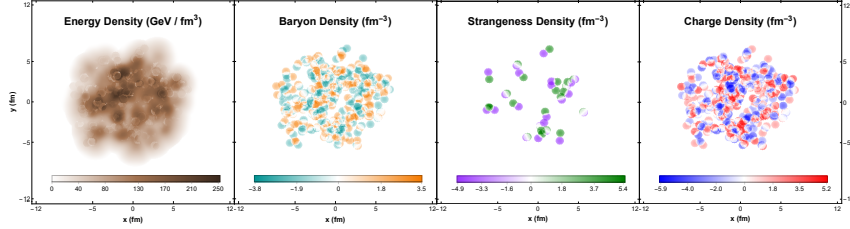


Fig. 5.: Energy and charge density distributions for an ICCING event with Green's function evolution of energy and charge perturbations from gluon to quark-antiquark splittings.^{109,110}

2.2. Hydrodynamics with multiple conserved charges

As mentioned previously, in the context of ultra-relativistic nuclear collisions, the primary focus often centers on the midrapidity charge-neutral region that is formed through the interaction of low- x gluons, which do not carry conserved charges. However, at BES and lower energies, there is a growing need to investigate the longitudinal dynamics across both forward and backward rapidity regions, where the baryon density can be notably higher, and, in fact, a significant fraction of the incoming baryon charge can be stopped even near midrapidity. The measurements of hadron species with different charges indicate that the fluid created in intermediate- and low-energy collisions carries various quantum numbers, where we must consider the conservation of baryon number (B), strangeness (S), and electric charge (Q), which are conserved by the strong interaction and all hold significant relevance in the phenomenology of heavy-ion collisions (see Fig. 5). Consequently, it becomes imperative to develop a hydrodynamic framework that accounts for the dynamic evolution of multiple conserved charges.

2.2.1. Conservation equations

For the systems involving N_q types of charges, hydrodynamics serves as a macroscopic theory that describes the spacetime evolution of the energy-momentum tensor $T^{\mu\nu}$ and the charge currents N_q^μ , encompassing a total of $10 + 4N_q$ independent components (10 from $T^{\mu\nu}$ and 4 from each charge current). A set of evolution equations that govern these components can be derived from the conservation laws for energy, momentum, and charges:

$$\partial_\mu T^{\mu\nu} = 0, \quad \partial_\mu N_q^\mu = 0, \quad (4)$$

where $q \in \{B, Q, S\}$, and ∂_μ represents the covariant derivative in a general curvilinear coordinates. In the current context involving BQS charges, we

shall take $N_q = 3$ from now on.

The independent components of $T^{\mu\nu}$ and N_q^μ have a more physical representation in terms of the hydrodynamic decomposition of these tensors, given by:

$$T^{\mu\nu} = \epsilon u^\mu u^\nu - (p + \Pi) \Delta^{\mu\nu} + \pi^{\mu\nu}, \quad (5)$$

$$N_q^\mu = n_q u^\mu + n_q^\mu, \quad q \in \{B, Q, S\}. \quad (6)$$

Here, the flow four-velocity $u^\mu(x)$, normalized with $u^\mu u_\mu = 1$, is defined as the time-like eigenvector of the energy-momentum tensor:

$$T^{\mu\nu} u_\nu = \epsilon u^\mu, \quad (7)$$

and it specifies the local rest frame (LRF) of the fluid at point x ; this definition employs the so-called ‘‘Landau frame.’’^c The tensors $u^\mu u^\nu$ and $\Delta^{\mu\nu} \equiv g^{\mu\nu} - u^\mu u^\nu$ are projectors on the temporal and spatial directions in the LRF. ϵ and n_q represent the energy and net charge densities in the LRF, and they can be obtained as the following projections of $T^{\mu\nu}$ and N_q^μ :

$$\epsilon = u_\mu T^{\mu\nu} u_\nu, \quad n_q = u_\mu N_q^\mu. \quad (8)$$

From these quantities, the local equilibrium pressure p is determined using the equation of state, $p = p(\epsilon, n_B, n_Q, n_S)$, at finite charge densities (see Sec. 2.2.5 for more discussion). The shear stress tensor $\pi^{\mu\nu}$, bulk viscous pressure Π , and net charge diffusion currents n_q^μ describe dissipative flows that account for deviations from local equilibrium. The shear stress tensor $\pi^{\mu\nu}$ is subject to the conditions of tracelessness, $\pi^\mu_\mu = 0$, and orthogonality, $\pi^{\mu\nu} u_\mu = 0$; thus, it has 5 unknowns. The diffusion currents satisfy $u_\mu n_q^\mu = 0$ and represent the flow of charges in the local rest frame; thus, they have $3N_q$ unknowns. The bulk viscous pressure Π is another unknown. Therefore, we have $6 + 3N_q$ unknown dissipative components.

Using the decomposition (5,6) the conservation laws (4) can be brought into the physically intuitive form¹¹⁴

$$D\epsilon = -(\epsilon + p + \Pi)\theta + \pi_{\mu\nu}\sigma^{\mu\nu}, \quad (9)$$

$$(\epsilon + p + \Pi) Du^\mu = \nabla^\mu(p + \Pi) - \Delta^{\mu\nu} \nabla^\sigma \pi_{\nu\sigma} + \pi^{\mu\nu} Du_\nu, \quad (10)$$

$$Dn_q = -n_q \theta - \nabla_\mu n_q^\mu. \quad (11)$$

^cIn the Landau frame, the total energy-momentum diffusion current (or heat flow vector) is zero, i.e., $W^\mu \equiv u_\nu \delta T^{\mu\nu} = 0$. Alternatively, one might opt for the Eckart frame to define the local rest frame by requiring that the net charge diffusion current is zero.¹¹¹ However, in scenarios where a charge-neutral fluid is produced in ultra-relativistic collisions or in a fluid with multiple conserved charges generated in lower-energy collisions, the definition of such a frame is less suitable or even ill-defined.¹¹² One can also define the theory in a general hydrodynamic frame.¹¹³

Here $D = u_\mu \partial^\mu$ denotes the time derivative in the LRF, $\theta = \partial_\mu u^\mu$ is the scalar expansion rate, $\nabla^\mu = \partial^{\langle\mu}$ (where generally $A^{\langle\mu} \equiv \Delta^{\mu\nu} A_\nu$) denotes the spatial gradient in the LRF, and $\sigma^{\mu\nu} = \nabla^{\langle\mu} u^{\nu\rangle}$ (where generally $B^{\langle\mu\nu} \equiv \Delta_{\alpha\beta}^{\mu\nu} B^{\alpha\beta}$, with the traceless spatial projector $\Delta_{\alpha\beta}^{\mu\nu} \equiv \frac{1}{2}(\Delta_\alpha^\mu \Delta_\beta^\nu + \Delta_\alpha^\nu \Delta_\beta^\mu) - \frac{1}{3} \Delta^{\mu\nu} \Delta_{\alpha\beta}$) is the shear flow tensor. Note that there are $1+3+N_q = 7$ independent conservation equations in Eqs. (9-11), and the pressure p is determined from the equation of state. These equations provide a clear insight into the underlying physics, especially when considered in the local rest frame.

Notably, the bulk viscous pressure, denoted as Π , is always added to the equilibrium pressure p , making $p+\Pi$ the effective pressure. Eq. (9) demonstrates that, in the ideal scenario, the energy density ϵ decreases within expanding fluids, as indicated by the fact that $D\epsilon$ is negative when the expansion rate θ is positive. The presence of the shear viscous term, $\pi_{\mu\nu} \sigma^{\mu\nu}$, mitigates the decrease in energy density when it is positive, a phenomenon known as “viscous heating.” However, in the case of far-off-equilibrium fluids, this term can turn negative, indicating what is referred to as “viscous cooling”.¹¹⁵ Eq. (11) conveys a similar message regarding charge densities n_q as Eq. (9) does for energy density. A diffusion current n_q^μ can either reduce or increase the charge density by carrying away or bringing in charges to a particular location via the divergence term. Eq. (10) bears a resemblance to Newton’s second law: the acceleration of the flow velocity Du^μ is driven by the gradient of the effective pressure $\nabla^\mu(p+\Pi)$, while the effective enthalpy density $(\epsilon+p+\Pi)$ serves as the inertia. The bulk viscous pressure Π tends to reduce the driving force of the radial flow, if it is negative. Moreover, the presence of the shear viscous term, $\pi^{\mu\nu} Du_\nu$, couples the flow evolution in different directions.

As previously mentioned, once the equation of state (EOS) is given, there remain $10 + 4N_q$ independent unknowns in $T^{\mu\nu}$ and N_q^μ , and $4 + N_q$ evolution equations arising from the conservation laws (9)-(11). To complete the equation system, we require additional $6 + 3N_q$ evolution equations for the dissipative components. The current state-of-the-art in relativistic dissipative hydrodynamic formalism is built upon the pioneering work of Müller¹¹⁶ and Israel-Stewart¹¹⁷ (for comprehensive overviews, see Refs. ^{113,118}). For instance, the Denicol-Niemi-Molnár-Rischke (DNMR) approach¹¹⁹ derives the equations of motion from the Boltzmann equation using the method of moments, applying a systematic power-counting scheme in Knudsen and inverse Reynolds numbers. This method is applied to a fluid with a single conserved charge. Using the same methodology,

Ref.¹¹² has derived multicomponent relativistic second-order dissipative hydrodynamics for a reactive mixture of various particle species with N_q conserved charges. The dynamic equations for the *BQS* diffusion currents were obtained (see also Ref.¹²⁰). Additionally, the stability conditions associated with these equations were examined, as discussed in Refs.^{121,122} Earlier efforts to derive these equations encompassed the pioneering work in Refs.^{123–126} Together with the $4 + N_q$ evolution equations arising from the conservation laws, the resulting $6 + 3N_q$ second-order equations of motion for the dissipative quantities can close the system.

2.2.2. Hydrodynamic quantities from kinetic theory

The macroscopic hydrodynamic formalism can be derived from the underlying microscopic kinetic theory governed by the Boltzmann equation.¹¹⁸ In the case of a mixture consisting of various particle species, each species i is characterized by its single-particle distribution function, $f_{i,\mathbf{p}} \equiv f(x, p_i)$. The spacetime evolution of these distribution functions is governed by the relativistic Boltzmann equation, given as:

$$p_i^\mu \partial_\mu f_{i,\mathbf{p}} = C[f_{i,\mathbf{p}}], \quad (12)$$

where external forces are neglected, and $C[f_{i,\mathbf{p}}]$ represents the collision term, which depends on all the distribution functions. As indicated by the Boltzmann *H*-theorem, collisions on the right-hand side drive the system towards the local equilibrium state $f_{i,\mathbf{p}}^0$, where entropy is maximized. Meanwhile, the derivatives on the left-hand side push the distribution $f_{i,\mathbf{p}}$ away from the local equilibrium state $f_{i,\mathbf{p}}^0$ with a deviation $\delta f_{i,\mathbf{p}}$, denoted as

$$f_{i,\mathbf{p}} \equiv f_{i,\mathbf{p}}^0 + \delta f_{i,\mathbf{p}}. \quad (13)$$

Here, collisions and derivatives compete in the evolution towards local equilibrium. When the collision terms exhibit large cross sections, and/or when the thermodynamic and flow gradients are relatively small, the influence of collisions becomes dominant in the competition. In such cases, the distribution $f_{i,\mathbf{p}}$ tends to approach the equilibrium state $f_{i,\mathbf{p}}^0$, leading to a small out-of-equilibrium part $\delta f_{i,\mathbf{p}}$.

The equilibrium state $f_{i,\mathbf{p}}^0$ is given by the Jüttner distribution function

$$f_{i,\mathbf{p}}^0 = \left[\exp \left(\frac{u_\mu(x) p_i^\mu - \mu_i(x)}{T(x)} \right) + a_i \right]^{-1}. \quad (14)$$

Here $a_i = \pm 1$ accounts for the fermionic (+) or bosonic (−) quantum statistics of the particle species i , and $u^\mu(x)$ is the fluid flow velocity, $T(x)$

the local temperature and $\mu_i(x)$ the local chemical potential at point x . In local equilibrium, the chemical potential $\mu_i(x)$ of a given chemically equilibrated species i can be expressed as

$$\mu_i = B_i\mu_B + Q_i\mu_Q + S_i\mu_S, \quad (15)$$

where (B_i, Q_i, S_i) are the baryon number, electric charge, and strangeness carried by particle species i , and (μ_B, μ_Q, μ_S) are the associated baryon, electric and strangeness chemical potentials. In a formal sense, solving Eq. (12) provides the spacetime evolution of $f_{i,\mathbf{p}}$ and, consequently, the evolution of $\delta f_{i,\mathbf{p}}$. This further serves as a basis for determining the evolution of the macroscopic dissipative variable.

To establish a connection between the microscopic phase-space distribution and macroscopic hydrodynamic fields, we introduce the notation for the following momentum integrals:

$$\langle \cdots \rangle_{i,0} \equiv \int dP_i (\cdots)_i f_{i,\mathbf{p}}^0, \quad \langle \cdots \rangle_{i,\delta} \equiv \int dP_i (\cdots)_i \delta f_{i,\mathbf{p}}, \quad (16)$$

where $dP_i \equiv d^3p_i / [(2\pi)^3 p_i^0]$ is the Lorentz-invariant integration measure. The total fluid net charge currents and energy-momentum tensor of the mixture of particle species can be expressed as follows:^d

$$T^{\mu\nu} \equiv \sum_i \int dP_i p_i^\mu p_i^\nu (f_{i,\mathbf{p}}^0 + \delta f_{i,\mathbf{p}}) = \sum_i (\langle p^\mu p^\nu \rangle_{i,0} + \langle p^\mu p^\nu \rangle_{i,\delta}), \quad (17)$$

$$N_q^\mu \equiv \sum_i q_i \int dP_i p_i^\mu (f_{i,\mathbf{p}}^0 + \delta f_{i,\mathbf{p}}) = \sum_i q_i (\langle p^\mu \rangle_{i,0} + \langle p^\mu \rangle_{i,\delta}), \quad (18)$$

where the summation is taken over all particle species in the mixture, and $q \in \{B, Q, S\}$ denotes the three types of charges. Using these two expressions, we effectively treat the mixture, consisting of multiple particle species carrying various charges, as a single fluid with multiple charge components.

It's important to note that the decomposition (13) of $f_{i,\mathbf{p}}$ into its equilibrium and off-equilibrium parts lacks uniqueness until the local equilibrium parameters $u^\mu(x)$, $T(x)$ and $\mu(x)$ in $f_{i,\mathbf{p}}^0$ as given in Eq. (14) are accurately defined. Additionally, the link between the decompositions in Eqs. (17,18) and those in Eqs. (5,6) has not yet been established. In fact, the flow velocity $u^\mu(x)$ has been established in Eq. (7) by selecting the Landau frame, consequently fixing the local energy density $\epsilon(x)$. To further determine $T(x)$ and $\mu(x)$, we require that $\delta f_{i,\mathbf{p}}$ contributes nothing to the local energy density and baryon density. This condition is commonly referred to as

^dHere, no degeneracy factor is explicitly introduced, but the spin degrees of freedom should be summed over; similarly in Eq. (36) and Eqs. (39)-(40).

the Landau matching condition. By combining Eqs. (8) with Eqs. (17,18), we can derive the following expressions for the local energy and baryon densities:

$$\epsilon = u_\mu T^{\mu\nu} u_\nu \equiv \sum_i \langle (u_\mu p^\mu)^2 \rangle_{i,0}, \quad n_q = u_\mu N_q^\mu \equiv \sum_i q_i \langle u_\mu p^\mu \rangle_{i,0}. \quad (19)$$

Meanwhile, the pressure can also be obtained, as given by

$$p = -\frac{1}{3} \sum_i \langle \Delta_{\mu\nu} p^\mu p^\nu \rangle_{i,0}. \quad (20)$$

In Eqs. (19), the conditions $\sum_i \langle (u_\mu p^\mu)^2 \rangle_{i,\delta=0} = 0$ and $\sum_i \langle u_\mu p^\mu \rangle_{i,\delta=0} = 0$ are imposed in accordance with the matching condition. Equations (19) define $T(x)$ and $\mu(x)$ and, in combination with the defined $u^\mu(x)$, determine $f_{i,\mathbf{p}}^0$.

Projecting out the additional components, as introduced in Eqs. (5,6), from Eqs. (17,18), we can deduce the dissipative components:

$$\pi^{\mu\nu} \equiv \Delta_{\alpha\beta}^{\mu\nu} T^{\alpha\beta} = \sum_i \langle p^{(\mu} p^{\nu)} \rangle_{i,\delta}, \quad (21)$$

$$\Pi \equiv -\frac{1}{3} T^{\mu\nu} \Delta_{\mu\nu} - p = -\frac{1}{3} \sum_i \langle \Delta_{\mu\nu} p^\mu p^\nu \rangle_{i,\delta}, \quad (22)$$

$$n_q^\mu \equiv \Delta_\nu^\mu N_q^\nu = \sum_i q_i \langle p^{(\mu} \rangle_{i,\delta}. \quad (23)$$

Equations (21-23) indicate that, under the matching condition, the dissipative components only receive contributions from the off-equilibrium $\delta f_{i,\mathbf{p}}$. If we introduce the irreducible moments of tensor-rank ℓ and energy-rank r of $\delta f_{i,\mathbf{p}}$ for a given particle species i ,

$$\rho_{i,r}^{\mu_1 \dots \mu_\ell} \equiv \Delta_{\nu_1 \dots \nu_\ell}^{\mu_1 \dots \mu_\ell} \int dP_i E_{i,\mathbf{p}}^r p_i^{\nu_1} \dots p_i^{\nu_\ell} \delta f_{i,\mathbf{p}} = \langle E_{\mathbf{p}}^r p^{(\mu_1} \dots p^{\mu_\ell)} \rangle_{i,\delta}, \quad (24)$$

in terms of irreducible tensors $p^{(\mu_1} \dots p^{\mu_\ell)}$ that are orthogonal to the flow velocity, it's straightforward to verify that Eqs. (21-23) yield

$$\pi^{\mu\nu} = \sum_i \rho_{i,0}^{\mu\nu}, \quad \Pi = -\frac{1}{3} \sum_i (m_i^2 \rho_{i,0} - \rho_{i,2}), \quad n_q^\mu = \sum_i q_i \rho_{i,0}^\mu, \quad (25)$$

where $E_{i,\mathbf{p}} = p_i^\mu u_\mu$ and $m_i^2 = p_i^\mu k_{i,\mu}$ denotes the energy and mass of the given particle species i , respectively.

2.2.3. Dissipative equations of motion

In principle, one can choose to solve the Boltzmann equation (12) to obtain $f_{i,\mathbf{p}}$. Once $f_{i,\mathbf{p}}$ is obtained, it can be used to calculate the evolving dissipative variables given by Eqs. (21)-(23). However, this is generally a very complicated task. Alternatively, one can re-formulate the Boltzmann equation into an infinite system of coupled evolution equations for the moments $\rho_{i,r}^{\mu_1 \dots \mu_\ell}$. The solution of these equations governs the evolution of the dissipative variables through Eq. (25). Employing this approach, the DNMR theory¹¹⁹ derived these dissipative evolution equations for a single-component fluid. In Refs.,^{112,115,127} these equations were studied for multicomponent fluids.

More specifically, to derive the equations of motion for the irreducible moments, the equation for the comoving derivative $\dot{\rho}_{i,r}^{\langle \mu_1 \dots \mu_\ell \rangle} \equiv \Delta_{\nu_1 \dots \nu_\ell}^{\mu_1 \dots \mu_\ell} D \rho_{i,r}^{\nu_1 \dots \nu_\ell}$, one can proceed by multiplying the Boltzmann equation (12) in the following form:

$$\delta \dot{f}_{i,\mathbf{p}} = -\dot{f}_{i,\mathbf{p}}^0 - E_{i,\mathbf{p}}^{-1} p_{i,\nu} \nabla^\nu f_{i,\mathbf{p}}^0 - E_{i,\mathbf{p}}^{-1} p_{i,\nu} \nabla^\nu \delta f_{i,\mathbf{p}} + E_{i,\mathbf{p}}^{-1} C[f_{i,\mathbf{p}}] \quad (26)$$

by $E_{i,\mathbf{p}}^r p_i^{\langle \mu_1} \dots p_i^{\mu_\ell \rangle}$ and subsequently integrating over momentum space. After linearizing the collision integral with respect to the quantities $\phi_{i,\mathbf{p}} \equiv \delta f_{i,\mathbf{p}} / [f_{i,\mathbf{p}}^0 (1 - a_i f_{i,\mathbf{p}}^0)]$, which implies that

$$\delta f_{i,\mathbf{p}} \equiv [f_{i,\mathbf{p}}^0 (1 - a_i f_{i,\mathbf{p}}^0)] \phi_{i,\mathbf{p}}, \quad (27)$$

the irreducible moments of the collision integral $C[f_{i,\mathbf{p}}]$ can be expressed as a linear combination of the irreducible moments $\rho_{i,r}^{\mu_1 \dots \mu_\ell}$. A closed set of equations of motion for the dissipative quantities Π , n_q^μ , and $\pi^{\mu\nu}$ is consequently obtained by truncating the infinite set of moment equations in the $(10 + 4N_q)$ -moment approximation.¹¹²

The dissipative equations of motion are of relaxation type. For the evolution equations of the bulk viscous pressure and shear stress tensor, they are given by

$$\tau_\Pi \dot{\Pi} + \Pi = -\zeta \theta + (\text{higher-order terms}), \quad (28)$$

$$\tau_\pi \dot{\pi}^{\langle \mu\nu \rangle} + \pi^{\mu\nu} = 2\eta \sigma^{\mu\nu} + (\text{higher-order terms}), \quad (29)$$

where $\dot{\Pi} \equiv D\Pi$ and $\dot{\pi}^{\langle \mu\nu \rangle} \equiv \Delta_{\alpha\beta}^{\mu\nu} D\pi^{\alpha\beta}$, ensuring that all terms are purely spatial in the LRF and, if applicable, traceless. τ_Π and τ_π represent the relaxation times for Π and $\pi^{\mu\nu}$, respectively. They determine the rate at which the dissipative flows relax to their Navier-Stokes limits, characterized by $\Pi_{\text{NS}} \equiv -\zeta\theta$, and $\pi_{\text{NS}}^{\mu\nu} \equiv 2\eta\sigma^{\mu\nu}$. Here, ζ and η denote the bulk viscosity and shear viscosity, respectively. These parameters describe the first-order

response of the dissipative flows to their driving forces — the negative of the scalar expansion rate θ and the shear flow tensor $\sigma^{\mu\nu}$ — leading the system away from local equilibrium. The determination of these parameters will be further discussed in Sec. 2.2.4.

Similarly, the equation for the diffusion current of charge q is given by:

$$\sum_{q'} \tau_{qq'} \dot{n}_q^{\langle\mu\rangle} + n_q^\mu = \sum_{q'} \kappa_{qq'} \nabla^\mu \left(\frac{\mu_{q'}}{T} \right) + (\text{higher-order terms}), \quad (30)$$

where the sum is taken over *BQS* charges. Importantly, due to the presence of off-diagonal elements in the diffusion coefficient matrix $\kappa_{qq'}$, the diffusion current of a particular charge q can receive contributions from gradients of the chemical potentials of all charge types. This is a natural consequence of the fact that each constituent of the fluid may carry multiple types of charges, leading to intricate couplings between different charges. For instance, in the context of a (1+1)-dimensional system, where the dissipative effects from shear and bulk viscous pressures are ignored, it was observed in Ref. ¹²⁸ that a gradient in baryon number can not only give rise to a baryon current but also induce currents in strangeness and electric charge. The study demonstrated that strangeness separation can manifest in a system initially in a strangeness-neutral state, primarily driven by its coupling to the baryon diffusion current.

In scenarios where the charges are not coupled, assuming that each constituent of the fluid carries only a single type of charge, the equation simplifies to:

$$\tau_q \dot{n}_q^{\langle\mu\rangle} + n_q^\mu = \kappa_q \nabla^\mu \left(\frac{\mu_q}{T} \right) + (\text{higher-order terms}), \quad (31)$$

where the relaxation time $\tau_q \equiv \tau_{qq}$ and diffusion coefficient $\kappa_q \equiv \kappa_{qq}$ represent the diagonal elements of the respective matrices. This corresponds to the conventional scenario that investigations have predominantly focused on. Similar to the case of bulk viscous pressure and shear stress tensor, Eq. (31) of relaxation type suggests that when the expansion rates are sufficiently small, such that $\nabla^\mu (\mu_q/T)$ evolves slowly, the charge diffusion current n_q^μ will asymptotically approach the values predicted by the Navier-Stokes theory at times much greater than the relaxation time τ_q , i.e.,

$$n_{q,\text{NS}}^\mu \equiv \kappa_q \nabla^\mu \left(\frac{\mu_q}{T} \right). \quad (32)$$

This is the equation of motion derived from relativistic Navier-Stokes theory. It also resembles relativistic Fick's law, illustrating how diffusion currents arise due to gradients in the thermal potential associated with the

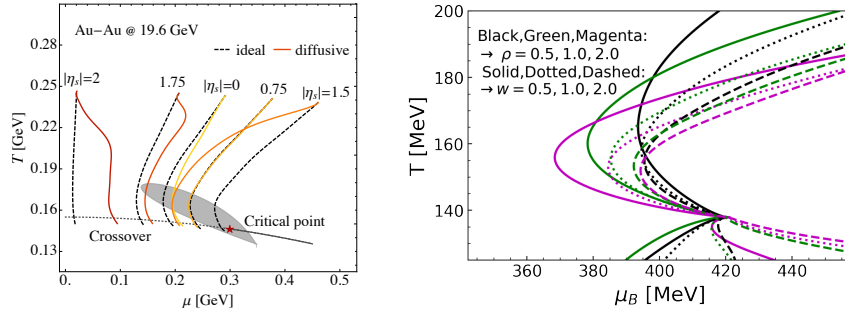


Fig. 6.: *Left*: Phase diagram trajectories of the fireball within different rapidity windows, comparing ideal evolution (black dashed lines) with evolution including baryon diffusion (colored solid lines).⁷² *Right*: Illustration of the critical lensing effect through isentropic trajectories crossing the critical point with different parameters controlling the critical region of the EOS.¹³⁰

charge. Notably, in a flat Minkowski space, where $\nabla^\mu = (0, -\partial_x, -\partial_y, -\partial_z)$ in the local rest frame, the minus sign in the spatial components indicates that diffusion currents work to smooth out the existing inhomogeneities that initially generated the current. Additionally, the diffusion coefficient κ_q decreases as the temperature of the expanding fireball decreases. Due to these two factors, the baryon diffusion current is found to be significant only during the early stages of the evolution.^{72,129}

So far, among the three types of charges, the baryon charge is the only one that has received significant attention in phenomenological studies, albeit to a much lesser extent compared to the investigations of viscous effects associated with shear stress tensor and bulk pressure. One of the primary reasons for the focus on the baryon charge is that both baryon density and temperature are among the most important controllable features that can be adjusted in heavy-ion collisions by varying the collision energy. Moreover, the QCD phase diagram is commonly depicted with a horizontal axis representing either baryon density or baryon chemical potential, and a vertical axis representing temperature. Consequently, the dynamics of the baryon current plays a pivotal role in determining the evolution of baryon-rich QCD matter within this diagram and in the search for the signatures of the QCD critical point (see the left panel of Fig. 6). Eqs. (31)-(32) encapsulate the fundamental information required to comprehend baryon diffusion current, which is essential for understanding the associated phenomenology.

We should also briefly mention a few studies as examples that have focused on developing hydrodynamic formalisms considering only baryon

number (or a single-component charge). These approaches have utilized various methods, including the moment method,^{119,131} Chapman-Enskog method,¹²⁷ 14-moment method,¹³² and anisotropic hydrodynamics.^{133,134} Additionally, a newly developed Maximum Entropy method^{135,136} and a novel Relaxation Time Approximation¹³⁷ show promise but has yet to be extended to systems with finite charges. Moreover, multiple hydrodynamic codes, such as MUSIC,^{71,82} BEShydro,^{86,138} vHLLE,^{88,139} and CLvisc,^{140,141} have been developed and implemented to simulate the (3+1)-dimensional evolution of a baryon-charged fluid.

2.2.4. *Transport coefficients*

Transport coefficients are parameters characterizing the transport of various quantities—like energy-momentum and charges—within the QGP fluid. Some key first-order transport coefficients encompass shear (η) and bulk (ζ) viscosity, alongside diffusion coefficients for conserved charges (κ_q) and the relaxation times governing these dissipative quantities (e.g., τ_q). Second-order and even higher-order transport coefficients describe the interplay among these dissipative components in the higher-order terms of their equations of motion.^e These coefficients play a vital role in describing the macroscopic behavior of QCD matter by bridging microscopic properties, such as interactions between its constituents, with the system's overall transport behavior. Their dependence on temperature and chemical potentials encapsulates the distinctive properties of the QCD matter and the underlying microscopic interactions.

Obtaining transport coefficients poses a great challenge¹⁴⁶ and often demands sophisticated calculations and models. Within the field of heavy-ion physics, acquiring these coefficients for nuclear matter involves various methods (see Fig. 7), with one of the most common being the application of kinetic theory to many-particle systems. This method involves comparing the macroscopic and microscopic definitions of thermodynamic quantities, integrating particle interactions as dynamic inputs into the expressions of transport coefficients. Usually, when deriving the hydrodynamic equations of motion, these expressions for transport coefficients in terms of particle interactions are naturally derived. For studies employing kinetic theory to derive transport coefficients, refer to, for example, Refs. ^{127,147–153} Although

^eCurrently, second-order transport coefficients receive little attention, and in practice, they are often connected to thermodynamic quantities through relationships with first-order coefficients evaluated in kinetic theory or holography.^{142–145}

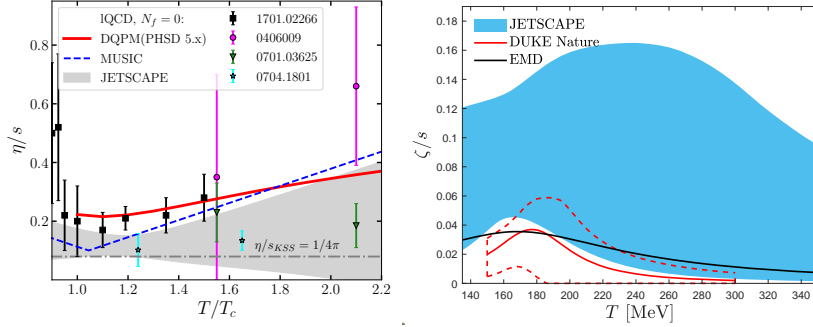


Fig. 7.: *Left*: Different specific shear viscosities plotted as a function of the scaled temperature T/T_c at zero chemical potential (figure from Ref. ¹⁶³). *Right*: The holographic EMD prediction for the specific bulk viscosity compared to the results favored by phenomenological multistage models at zero chemical potential (figure from Ref. ¹⁶⁴).

the coefficients estimated within kinetic theories can provide insights, they do not represent real QCD matter due to the oversimplified interactions often assumed.

Moreover, linear response theory serves as a framework to describe a system's behavior when subjected to small perturbations or external fields. Within this framework, the Kubo formula characterizes the system's response to perturbations and provides specific expressions for transport coefficients by relating the transport coefficients of a slightly non-equilibrium system to real-time correlation functions computed within an equilibrium thermal ensemble.¹⁵⁴ This formula serves as a foundational tool for calculating transport coefficients from first principles using finite-temperature quantum field theory and has played a crucial role in determining the transport coefficients of nuclear matter.^{114,155–159} Additionally, transport coefficients can be extracted using lattice QCD calculations^{1,160–162} through conserved current correlators. These Euclidean correlators are connected, via an integral transform, to spectral functions. The small-frequency form of these spectral functions determines the transport properties using the Kubo formula.

The development of the AdS/CFT correspondence, also known as the gauge/gravity duality more broadly, has introduced a new paradigm for exploring strongly coupled gauge theories through weakly coupled gravitational systems. This duality has proven invaluable for investigating both thermal and hydrodynamic properties of field theories at strong cou-

pling. Utilizing holographic methods, the specific shear viscosity η/s has been bounded by a minimum value of $1/4\pi$.¹⁶⁵ The remarkable order-of-magnitude agreement with RHIC data has spurred extensive efforts to employ holographic techniques in computing various transport coefficients of the QCD medium^{166–173} (for comprehensive reviews, see^{164,174,175}).

Despite the advancements in various methods for calculating transport coefficients, the arguably most reliable approach to determining their values remains model-to-data comparison phenomenologically.¹⁴⁶ Early recognition highlighted the sensitivity of hadronic observables, like the distributions and correlations of hadrons in heavy-ion collisions, to the shear and bulk viscosities of QCD matter.^{176–179} Qualitatively, a significant bulk viscosity tends to isotropically reduce the momenta of hadrons, whereas shear viscosity diminishes their azimuthal momentum asymmetry. Initial works aimed at constraining these coefficients via hydrodynamic simulations of heavy-ion collisions primarily focused on the specific shear viscosity η/s , often approximated as a constant (as reviewed in Refs.^{28,180}). Contemporary endeavors seek to characterize their dependencies on the equilibrium properties of the system, typically focusing on constraining the temperature dependence of the specific shear and bulk viscosities,^{181–184} denoted as $(\eta/s)(T)$ and $(\zeta/s)(T)$, respectively. The functional forms of the dependence are often guided by insights obtained from the theoretical calculations.^{185–189}

As we move into an era of demanding precision, the challenge lies in quantitatively constraining viscosities with quantified uncertainties derived from measurements. The hydrodynamic expansion of the deconfined QGP stands as one among several phases within heavy-ion collisions, accompanied by various stages of many-body dynamics before and after this fluid phase. The evolution itself involves intricate variations in flow velocity and temperature profiles, varying from collision to collision. These factors pose significant challenges in disentangling the contributions of shear and bulk viscosities via hadronic measurements. Consequently, theoretical uncertainties at each stage of the collision can significantly influence estimations of the viscosities. Achieving a meaningful constraint on QGP viscosities from collider measurements demands extensive model-to-data comparisons encompassing multiple collision stages, meticulously modeling each phase, and contrasting resulting predictions against extensive and diverse experimental data.

Utilizing Bayesian statistical analysis to systematically constrain QGP transport properties, with precisely quantified uncertainties, has emerged

as a successful approach within various theoretical frameworks over the last decade^{142–145,190–200} (for comprehensive overviews, see Refs.^{201,202}). These studies have significantly advanced model-data inference in heavy-ion physics, offering diverse perspectives and insights. For instance, pioneering works in Refs.^{193,195} conducted the first Bayesian inference on temperature-dependent shear and bulk viscosities. Additionally, deeper insights into the temperature dependence of transport coefficients and the event-by-event nucleon substructure were gained using measurements from p -Pb and Pb-Pb collisions in Ref.¹⁹⁴ The JETSCAPE Collaboration presented Bayesian analyses utilizing p_T -integrated measurements at top RHIC and LHC energies, offering robust constraints on the temperature dependence of QGP shear and bulk viscosities around the crossover temperature.^{142,143} Notably, this study also examined theoretical uncertainties stemming from various off-equilibrium corrections (see Sec. 2.3.2) during the particlization stage for the first time. Further constraints using p_T -differential observables were explored in Refs.^{144,145} Moreover, Bayesian quantifications with color glass condensate initial conditions^{198,199} and anisotropic hydrodynamics²⁰⁰ were separately undertaken, contributing to a comprehensive understanding of QGP dynamics.

At the BES energies, the consideration of BQS charges becomes essential, and thus understanding the transport coefficients' dependence on equilibrium properties necessitates considering the finite chemical potentials associated with these charges. Current efforts have primarily focused on the dependence on the baryon chemical potential (μ_B), although progress is significantly less compared to investigations at zero μ_B . The presence of baryon chemical potential can significantly modify the system's transport properties.^f For example, at finite μ_B , the system's fluidity is assessed based on the ratio of shear viscosity to the enthalpy multiplied by temperature, $\eta T/(\epsilon + p)$, rather than relying on the specific shear viscosity η/s .²⁰³ Calculations using Chapman-Enskog theory within a simple hadronic model revealed a substantial reduction in $\eta T/(\epsilon + p)$ compared to η/s at nonzero μ_B for a hadron resonance gas.²⁰⁴ This suggests that systems generated at lower collision energies could exhibit fluid-like behavior, displaying an effective fluidity similar to that observed near the phase transition at the top RHIC energy. Studies like Refs.^{53,181} demonstrated that measurements of

^fIn the critical region, fluctuations significantly modify the physical transport coefficients, leading to their correlation length dependence. As a result, the transport coefficients could exhibit singularities at the critical point. A concise discussion on this topic can be found in Ref.⁸⁶

rapidity-differential anisotropic flows could constrain the shear viscosity's temperature dependence in regions where μ_B plays a significant role. Additionally, several investigations have explored constraints on η/s at various beam energy using measurements at the BES.^{87,205–207}

In addition to phenomenological constraints on η/s at finite μ_B , various approaches have been employed to evaluate it. For example, calculations have been conducted using the gauge/gravity duality,^{173,208,209} the dynamical quasiparticle model (DQPM) by explicitly computing parton interaction rates,²¹⁰ the extended $N_f = 3$ Polyakov Nambu-Jona-Lasinio (PNJL) model,²¹¹ and through the HRG model.^{159,212,213} Regarding the specific bulk viscosity ζ/s , although there are some phenomenological constraints at finite μ_B ,^{206,207} it has received less attention in many phenomenological studies at the BES. However, several of the aforementioned approaches that evaluate η/s at finite μ_B also examine ζ/s under the same conditions.^{173,208–210} The Bayesian inference conducted in Ref.²⁰⁶ suggests a non-monotonic relationship between the QGP's specific bulk viscosity $\zeta T/(\epsilon + p)$ and the collision energy, although further systematic analysis is required to confirm this observation.

At the BES, the diffusion coefficients κ_q associated with BQS charges, along with the cross diffusion coefficients $\kappa_{qq'}$, hold significant importance. Among these, the baryon diffusion coefficient κ_B assumes a crucial role in the evolution of charged QGP fireball. Its significance lies in determining the trajectory of systems across the QCD phase diagram and is particularly relevant for interpreting potential signatures of the QCD critical point, especially concerning proton cumulant measurements. The baryon diffusion coefficient has been derived through various methodologies. Expressions for κ_B for the net baryon diffusion current were obtained using Grad's 14-moment and Chapman-Enskog methods.^{71,119,125,127,150,214} Additionally, evaluations of κ_B have been performed within holographic models^{172,173,208,209} and the dynamical quasiparticle model.²¹⁰ Cross diffusion coefficients $\kappa_{qq'}$ were also derived employing kinetic approaches^{112,128,152} and various transport models.^{153,158,159}

Currently, we face significant challenges in precisely constraining the baryon diffusion coefficient, particularly relying on net proton yields in rapidity.^{71–73,215} This observable is intricately entangled with both the initial baryon distribution and the hydrodynamic transport. The former is particularly sensitive to baryon stopping during the prehydrodynamic stage, while the latter is particularly sensitive to the longitudinal gradient of baryon density and κ_B . Consequently, understanding and accurately con-

straining κ_B necessitate a thorough disentanglement of these intertwined effects, particularly improving our comprehension of the initial baryon distribution, as discussed in Sec. 2.1. Additional observables at the BES, such as baryonic directed flow $v_1(y)$ ⁵⁶ and the polarization of Λ hyperons,²¹⁶ might also offer insights into constraining κ_B . Additionally, when explored as functions of relative azimuthal angle, balance functions exhibit sensitivity to the diffusivity of light quarks, serving as independent observables for constraining the charge diffusion constants.^{217–220} However, achieving a robust phenomenological constraint on κ_B and its temperature and baryon chemical potential dependence necessitates a comprehensive model-data inference approach incorporating diverse measurements, especially those in rapidity.

2.2.5. Equations of state at finite chemical potentials

The EOS of QCD characterizes the thermodynamic properties of strongly interacting matter, providing a relationship among key thermodynamic variables such as pressure, temperature, and chemical potentials. In hydrodynamic simulations, the EOS plays a crucial role in reducing the number of unknown variables to close the system of equations and is sometimes essential when determining the values of transport coefficients. Much like transport coefficients, the EOS encapsulates the fundamental properties of QCD. The mapping of the QCD phase diagram, essentially dictated by probing the EOS, stands as one of the primary objectives of Beam Energy Scan programs.⁷ Presently, the high-energy nuclear physics and astrophysics communities are in a unique position to establish highly stringent constraints on the EOS of strongly interacting matter, drawing from both heavy-ion collisions and neutron star observations through a comprehensive, multi-disciplinary strategy.^{9,221,222}

For a comprehensive quantitative description of nuclear collisions, it is imperative to have an EOS as input for hydrodynamic simulations. Particularly, simulating the dynamic evolution of the collision fireball created at various beam energies, which transitions from a deconfined partonic fluid to a confined hadronic gas, necessitates an EOS that captures the thermodynamic properties across a wide range of temperatures and chemical potentials. Just like the transport coefficients, an EOS can be derived within the same kinetic approach used for deriving hydrodynamic equations of motion, but it is not truly representative of QCD. A modern approach to constructing such an EOS involves a smooth interpolation around the phase

transition between a lattice QCD EOS (effective at high temperatures) and an HRG EOS (effective at low temperatures)^{223,224} (for a comprehensive overview, see Refs.^{9,225}). Utilizing such an EOS is essential for maintaining the conservation of energy-momentum and charges during the particlization process at the freeze-out surface, marking the transition from a continuous macroscopic hydrodynamics framework to a discrete microscopic particle transport approach (see Sec. 2.3).

Deriving the EOS of QCD at finite baryon chemical potential through conventional Monte Carlo simulations in lattice QCD faces significant challenges. This is primarily due to the fermion sign problem, a fundamental technical obstacle characterized by complex exponential.²²⁶ However, recent years have seen the proposal of alternative methods to extract the properties of QCD matter at low baryon chemical potential.^{227–230} These methods include Taylor expansion around $\mu_B = 0$ and analytic continuation from imaginary μ_B (for a comprehensive overview, see Ref.^{1,226,231}). Furthermore, holographic approaches have been developed to match QCD thermodynamics at $\mu_B = 0$, successfully reproducing all the Taylor expansion coefficients available from lattice QCD. These holographic methods are then extended to high baryon density, a regime currently beyond the reach of lattice simulations.²³² For a comprehensive overview of holographic descriptions, particularly those based on the class of gauge-gravity Einstein–Maxwell–Dilaton (EMD) effective models, refer to Ref.¹⁶⁴ Note that, in these methods, the investigation of the EOS of QCD has mostly focused on finite μ_B , while keeping $\mu_Q = \mu_S = 0$.

In heavy-ion collisions at the BES, it is reasonable to assume that light quarks (u , d , and s) can achieve thermalization in the QGP, making the EOS dependent on non-zero chemical potentials of baryon number, electric charge, and strangeness.^{233,234} The chemical potentials of BQS are interconnected with those of the relevant quarks through the following relationships:

$$\mu_u = \frac{1}{3}\mu_B + \frac{2}{3}\mu_Q, \quad \mu_d = \frac{1}{3}\mu_B - \frac{1}{3}\mu_Q, \quad \mu_s = \frac{1}{3}\mu_B - \frac{1}{3}\mu_Q - \mu_S. \quad (33)$$

The lattice QCD EOS at non-zero chemical potentials can be constructed using a Taylor expansion around vanishing chemical potentials:

$$\frac{p_{\text{lat}}}{T^4} = \frac{p(T)}{T^4} + \sum_{l,m,n} \frac{\chi_{l,m,n}^{BQS}(T)}{l!m!n!} \left(\frac{\mu_B}{T}\right)^l \left(\frac{\mu_Q}{T}\right)^m \left(\frac{\mu_S}{T}\right)^n, \quad (34)$$

where $p(T)$ represents the pressure and the expansion coefficients $\chi_{l,m,n}^{BQS}(T)$ are the susceptibilities at vanishing chemical potentials, calculated from

lattice QCD simulations. The susceptibilities at finite chemical potentials are defined as

$$\chi_{l,m,n}^{BQS} = \frac{\partial^l \partial^m \partial^n (p/T^4)}{\partial(\mu_B/T)^l \partial(\mu_Q/T)^m \partial(\mu_S/T)^n}. \quad (35)$$

Here matter-antimatter symmetry requires $l + m + n$ to be even.

In low-temperature regions, HRG models have been developed to incorporate hadronic interactions, aiming to enhance agreement with lattice QCD observables at temperatures below the chiral pseudocritical temperature T_{pc} . In the commonly used ideal HRG model, the system is represented as a non-interacting, multi-component gas of known hadrons and resonances. While this model describes the thermodynamic functions of lattice QCD at $\mu_B = 0$ up to temperatures around T_{pc} , deviations arise in susceptibilities of conserved charges, introduced in Eq. (35), which involve derivatives of the pressure function with respect to the chemical potentials and provide insights into the finer details of the EOS.^{228,235} In lattice QCD at the physical point, susceptibilities show rapid deviations from the ideal HRG in the vicinity, and even below, T_{pc} . These deviations may stem from hadronic interactions that are not dominated by resonance formation. Some attractive interactions, for instance, cannot be accurately described by simply adding resonances as free particles. Additionally, it has been suggested that deviations in lattice data on higher-order susceptibilities from the uncorrelated hadron gas baseline can be attributed to repulsive interactions.²³⁶ Consequently, HRG models incorporating repulsive interactions have gained interest in the context of lattice QCD calculations of fluctuations and correlations of conserved charges. For a comprehensive overview of HRG with van der Waals interactions, see Ref.²³⁷

Taking the ideal HRG as an example, its hydrostatic pressure can be expressed as:²³⁴

$$\begin{aligned} p_{\text{hrg}} &= \pm T \sum_i \int \frac{d^3p}{(2\pi)^3} \ln[1 \pm e^{-(E_i - \mu_i)/T}] \\ &= \sum_i \sum_k (\mp 1)^{k+1} \frac{1}{k^2} \frac{1}{2\pi^2} m_i^2 T^2 e^{k\mu_i/T} K_2\left(\frac{km_i}{T}\right), \end{aligned} \quad (36)$$

Here, i is the index for particle species, m_i is the particle's mass, and $K_2(x)$ is the modified Bessel function of the second kind. The index k describes the expansion of quantum distributions around the classical ones. The upper signs are for fermions, and the lower signs are for bosons. The hadronic chemical potential of species i is given by Eq. (15). Note that

to ensure energy and momentum conservation during the transition from hydrodynamics to a hadronic transport approach at particlization, it is essential that the particle species in the HRG EOS align with those included in the transport model.^{142,238}

Different approaches exist for interpolating the EOS between lattice QCD and the HRG. In Ref.,²³⁴ the EOS at non-zero (μ_B, μ_Q, μ_S) for the high-temperature region is constructed using lattice QCD calculations of $\chi_{l,m,n}^{BQS}(T)$. Subsequently, it is interpolated with the HRG EOS at low temperatures using a suitable interpolating function. In contrast, Ref.²³³ first introduces interpolations for $\chi_{l,m,n}^{BQS}(T)$ between the HRG and lattice QCD calculations across the entire relevant temperature range. The full EOS at non-zero chemical potentials is then constructed using Eq. (34) with the interpolated $\chi_{l,m,n}^{BQS}(T)$. Commonly, the interpolation between the two equations of state is centered around the crossover/phase transition line.

To simulate nuclear collisions at the BES energies, it is essential to employ relativistic hydrodynamics that accounts for multiple conserved charges and incorporates such an EOS constructed at nonzero BQS chemical potentials. Simultaneously, the evolution of charge transport must be taken into account, considering their interplay as outlined in Eq. (30). However, doing so is computationally demanding, particularly when conducting spacetime evolution in (3+1) dimensions which is necessary for collisions at the BES. Up to now, most simulations for the BES have focused on nonzero baryon charge alone, assuming $\mu_Q = \mu_S = 0$, and at times, even neglecting its diffusion current. Nevertheless, the consideration of nonzero electric charge and strangeness effects can be simplified in simulations that only account for nonzero baryon charge by deducing QS charges from B charge. This can be achieved by imposing constraints on the 4-dimensional EOS in (T, μ_B, μ_Q, μ_S) and subsequently projecting it onto 2-dimensional planes in (T, μ_B) . The values of (μ_Q, μ_S) can then be obtained from (T, μ_B) utilizing their relationships associated with the imposed constraints.^{225,234}

In nuclear collisions, the absence of valence quarks of strangeness in the colliding nuclei implies that the average strangeness density in the produced systems should be zero, denoted as $\langle n_S \rangle = 0$, a condition known as strangeness neutrality. Moreover, the electric density n_Q is linked to the net baryon density n_B taking into account the proton-to-nucleon ratio Z/A of the colliding nuclei. For instance, in the case of Au and Pb nuclei with Z/A around 0.4, one can assume $\langle n_Q \rangle = 0.4 \langle n_B \rangle$ for the systems produced in the collisions of these nuclei.^{233,234} Based on these considerations, Ref.²³⁴ imposes various constraining conditions on the EOS and constructs three

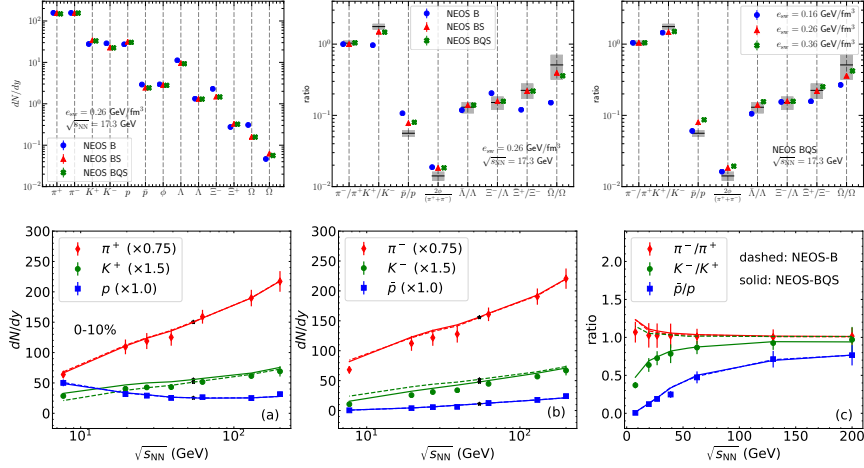


Fig. 8.: *Top*: Particle yields and ratios for central Pb+Pb collisions at $\sqrt{s_{\text{NN}}} = 17.3$ GeV with various freeze-out energy densities.²³⁴ *Bottom*: Particle yields and ratios for central Au+Au collisions at various beam energies $\sqrt{s_{\text{NN}}}$ with a fixed freeze-out energy density.²³⁹ The calculations incorporate equations of state with different constraints.

types: NEOS-B (assuming vanishing strangeness and electric charge chemical potentials, $\mu_Q = \mu_S = 0$), NEOS-BS (assuming strangeness neutrality $\langle n_S \rangle = 0$ and vanishing electric charge chemical potential $\mu_Q = 0$), and NEOS-BQS (assuming strangeness neutrality $\langle n_S \rangle = 0$ and a fixed electric charge-to-baryon ratio $\langle n_Q \rangle = 0.4 \langle n_B \rangle$). Comparing results obtained with different equations of state can elucidate the effects arising from imposing these distinct constraints.

These constraining conditions interrelate the *BQS* chemical potentials in various ways and thereby can impact the ratios between final yields of various hadron species carrying different hadronic chemical potentials. For instance, studies such as Refs.^{234,239} have indeed observed a significant improvement in the agreement between theoretical calculations and experimental measurements (see Fig. 8), particularly in the particle yield ratio such as K^-/K^+ as a function of beam energy when utilizing NEOS-BQS. However, it is crucial to acknowledge that the conditions $\langle n_S \rangle = 0$ and $\langle n_Q \rangle = 0.4 \langle n_B \rangle$ should be applied to averaged quantities across the colliding nuclei. Using these EOS enforces these constraints on each fluid cell, potentially leading to overly stringent limitations. For instance, studies like Refs.^{56,239} demonstrate that the implementation of NEOS-BQS

could disrupt the agreement between theoretical predictions and experimental measurements for some rapidity-dependent observables obtained using NEOS-B, particularly in the directed flows, $v_1(y)$, for identified hadrons with strangeness (e.g., Λ and K^+ carrying opposite μ_S). This illustrates that the choice of an appropriate EOS, whether a 2-dimensional EOS with specific constraints to save computational time or a 4-dimensional EOS with multicharge evolution for interpreting particular observables, may highly depend on the specific experimental measurements and relevant physics of interest. Regardless, it is crucial to bear in mind that heavy-ion collisions at the BES explore the T - μ_B - μ_Q - μ_S space instead of the T - μ_B plane with $\mu_Q = \mu_S = 0$. Caution should be exercised when drawing conclusions solely in terms of T - μ_B .

In phenomenological studies employing multistage hydrodynamic simulations, the EOS is often fixed as an input, without accounting for potential theoretical uncertainties. However, uncertainties associated with the EOS can arise from various factors, including uncertainties in lattice QCD results and different methods of interpolating the EOS between lattice QCD and the HRG. These uncertainties can propagate into the results of model calculations, impacting extracted QCD properties such as transport coefficients.^{223,238,240,241} To address these uncertainties, Bayesian constraints^{191,242–244} and machine learning techniques^{245,246} have been employed in the determination of EOS with consideration for various measurements (for a comprehensive review, see Ref.²⁴⁷). For example, in Ref.,¹⁹¹ Bayesian techniques were applied to a combined analysis of a large number of observables, allowing for variations in model parameters, which encompassed those related to the EOS. The resulting posterior distribution over possible equations of state was found to be consistent with results from lattice QCD EOS, providing valuable insights into constraining the QCD EOS.

Near the critical point, the thermodynamic properties of QCD matter are expected to exhibit singularities. To accurately describe dynamics in the vicinity of the critical point, the EOS should incorporate correct singular behaviors. The QCD critical point belongs to the same universality class as the 3D Ising model,^{3,4,248} from which the universal static critical behavior of the QCD critical point can be inferred. Starting with the pressure of the 3D Ising model, denoted as $p^{\text{Ising}}(r, h)$, where r is the reduced temperature and h is the magnetic field, one must map it to the pressure of QCD as a function of (T, μ_B) . However, the mapping is not universal, and different mappings can result in different shapes for the critical region, where the

critical pressure has a significant contribution.^{249–253} Moreover, the global scale of the critical pressure is also unknown, with larger values corresponding to larger critical regions. To account for these non-universalities, one can parametrize the critical contribution to the pressure in the critical region, once a mapping between (r, h) and (T, μ_B) is chosen:

$$p_{\text{critical}}^{\text{QCD}}(T, \mu_B) \sim p^{\text{Ising}}(r(T, \mu_B), h(T, \mu_B)), \quad (37)$$

where a function of (T, μ_B) can be added to set the overall scale. The full pressure is then expressed as the sum of the Ising contribution (i.e., $p_{\text{critical}}^{\text{QCD}}$) and the non-Ising one, the latter of which is not known *a priori*. Refs.^{250,251} construct the non-Ising pressure using the same Taylor expansion method described in Eq. (34), and the expansion coefficients at $\mu_B = 0$ are calculated by subtracting the Taylor coefficients of the Ising model (with a factor relevant to the overall function mentioned above) from the ones calculated by lattice QCD.

The construction of the EOS with a critical point involves large uncertainties and many parameters. Constraining these parameters from a model-to-data comparison, especially within a complex multistage hydrodynamic framework, is certainly not straightforward. Adding the critical point in an EOS can deform hydrodynamics trajectories, leading them to converge toward the critical point, a phenomenon known as the critical lensing (see the right panel of Fig. 6). This occurrence has been observed in both equilibrium and out-of-equilibrium evolutions, resulting in a higher number of trajectories passing through the vicinity of the critical point.¹³⁰ This potentially enhances the likelihood of detecting the critical point in experimental settings. Finally, we also note that initial off-equilibrium effects associated with the shear stress tensor and bulk viscous pressure can significantly influence the trajectories on the phase diagram in a non-trivial manner.^{115,254}

2.3. Freeze-out and particlization

As the QGP expands and cools below the pseudocritical temperature, *hadronization* takes place, transforming the deconfined partons into confined hadrons. During this transition, color neutralization takes place, leading to an increase in the mean-free path and rendering the hydrodynamic description ineffective. In multistage descriptions, we transition from a continuous macroscopic hydrodynamics framework to a discrete microscopic particle transport approach known as *particlization*. This transition occurs on a freeze-out hypersurface denoted as $\Sigma^\mu(x)$, which is defined based on

various criteria. One approach is to use a constant switching temperature T_{sw} when the matter is baryon-neutral,¹⁴² another involves a constant energy density e_{sw} when the matter is baryon-charged,⁷¹ and yet another method selects a surface of constant Knudsen number.²⁵⁵ These choices are motivated by our understanding of the phase transition line or the applicability of hydrodynamics. Determining the freeze-out hypersurface for particlization from a discretized hydrodynamic evolution can be a complex task, often accomplished using routines like the well-known Cornelius routine.²⁵⁶ Particles sampled on the hypersurface further propagate through the hadronic cascade stage, where the chemical and kinetic freeze-out processes are subsequently automatically performed.⁸ Modeling the emission of hadrons on this hypersurface is a crucial component of the multistage descriptions of heavy-ion collisions.

2.3.1. Cooper-Frye prescription

The Cooper-Frye prescription^{257,258} establishes a connection between the hydrodynamic fields and momentum distributions of identified particles, yielding the Lorentz-invariant momentum distribution for species i on a freeze-out surface denoted as $\Sigma_\mu(x)$, expressed as:

$$p^0 \frac{d^3 N_i}{d^3 p} = \frac{1}{(2\pi)^3} \int_\Sigma d^3 \sigma_\mu(x) p^\mu f_i(x, p). \quad (38)$$

Here, p^μ represents the four-momentum of the particle, $d^3 \sigma_\mu(x)$ corresponds to the normal vector for a freeze-out surface element at the point x , and $f_i(x, p)$ is the one-particle distribution function for species i . If we refrain from integrating over the hypersurface in Eq. (38) and perform momentum integration over the formula, it becomes evident that the Cooper-Frye prescription conserves various types of charges across the surface element, as indicated by:

$$N_q^\mu(x) = \sum_i q_i \int \frac{d^3 p}{(2\pi)^3 p^0} p^\mu f_i(x, p), \quad q \in \{B, Q, S\} \quad (39)$$

where q_i represent BQS charges carried by species i . This equation describes the local conservation of net charge q at surface element $d^3 \sigma_\mu(x)$ with spacetime coordinates x . Moreover, the distribution function $f_i(x, p)$

⁸Hadronization, chemical freeze-out, and kinetic freeze-out processes are physical phenomena, while particlization and the freeze-out hypersurface are not inherently physical but rather practical or computational concepts.

should be such that it conserves the energy-momentum tensor for an element at x on the hypersurface as well:

$$T^{\mu\nu}(x) = \sum_i \int \frac{d^3p}{(2\pi)^3 p^0} p^\mu p^\nu f_i(x, p). \quad (40)$$

The distributions given by Eq. (38) are Monte Carlo sampled to generate an ensemble of particles with well-defined positions and momenta. These ensembles serve as the initial state for the hadronic afterburner, as described by transport models that allow for the decay of unstable resonances and their regeneration via hadronic rescattering (see Sec. 2.4).

2.3.2. Off-equilibrium corrections

In a scenario where the QGP fluid is in a state of perfect local kinetic and chemical equilibrium, the distribution function $f_i(x, p)$ in Eq. (38) adopts the form outlined in Eq. (14). Within the context of particlization, the local temperature $T(x)$ and chemical potential $\mu_i(x)$ (15) should be considered as values on the freeze-out hypersurface. However, given the dissipative nature of the QGP fluid, which is indicated by the presence of terms such as $\pi^{\mu\nu}$, Π , and n_q^μ within the hydrodynamic description, the distribution function $f_i(x, p)$ includes off-equilibrium corrections. Without any hydrodynamic information guiding the decomposition of the fluid energy-momentum tensor $T^{\mu\nu}$ into contributions from different hadron species i , as written in Eq. (40), and lacking hydrodynamic information for all the infinitely many other momentum moments of the distribution functions (e.g., $\int_p p^\mu p^\nu p^\lambda f_i$), there exist infinitely many possibilities for the choice of distribution functions $f_i(x, p)$.¹⁴²

Given that the dissipative terms, such as $\pi^{\mu\nu}$, Π , and n_q^μ , are intended to capture deviations in the hadrons' momentum distributions and yields from local thermodynamic equilibrium, $f_{\text{eq},i} \equiv f_{i,\mathbf{p}}^0$, due to dissipative corrections, the distribution functions $f_i(x, p)$ can be expressed as:

$$f_i(x, p) \equiv f_{\text{eq},i} + \delta f_i = f_{\text{eq},i} + \delta f_{\pi,i} + \delta f_{\Pi,i} + \delta f_{n_q,i}. \quad (41)$$

Here the terms $\delta f_{\pi,i}$, $\delta f_{\Pi,i}$, and $\delta f_{n_q,i}$ correspond to the phase space distributions that encapsulate off-equilibrium effects originating from the dissipative terms $\pi^{\mu\nu}$, Π , and n_q^μ , respectively. In a formal context, to deduce the off-equilibrium corrections from the dissipative terms, we require the inverse mapping provided by Eqs. (21)-(23). The constraints from these dissipative terms are insufficient to fully determine all the off-equilibrium corrections associated with every hadron species, given the count of known

and unknown variables. In principle, the same methods used to derive the hydrodynamic equations of motion (see Eq. (27)), such as the Grad's method or Chapman-Enskog method, can also be employed to obtain these off-equilibrium terms in the Cooper-Frye prescription. However, similar to the transport coefficients and EOS derived directly from underlying kinetic theory, which fundamentally differ from those of QCD as previously discussed, there is often a lack of clear theoretical guidance regarding which formalism of δf_i to utilize for implementing particlization.

Assuming the simultaneous applicability of dissipative fluid dynamics and relativistic kinetic theory on the freeze-out hypersurface, various models of viscous corrections to the local equilibrium distribution function have been developed. These include Grad's method (also known as the 14-moments method in the relativistic context),^{259,260} the first-order Chapman-Enskog (CE) expansion in the relaxation time approximation,^{261,262} the Pratt-Torrieri-Bernhard (PTB) modified equilibrium distribution,²⁶³ the Pratt-Torrieri-McNelis (PTM) modified equilibrium distribution,²⁶⁴ the Pratt-Torrieri-McNelis modified anisotropic distribution (PTMA),²⁶⁵ and the newly proposed Maximum Entropy distribution.^{135,136} Brief summaries of the features of these various δf_i models can be found in Refs.^{142,264,265} Once δf_i and, consequently, f_i are determined, generating an ensemble of particles with positions and momenta at particlization involves interpreting the Cooper-Frye integrand in Eq. (38) as a probability density in phase-space and sampling it stochastically, recognizing that the integrand may not always be positive-definite. Two potential sources of negative contributions arise from instances where either $f_i(x, p)$ becomes negative or $p^\mu d^3\sigma_\mu(x)$ turns negative.

For instance, the distribution functions $f_i(x, p)$ can go negative when a linearized form of δf_i is used, such as in the Grad and Chapman-Enskog methods, which assume $|\delta f| \ll f_{\text{eq}}$. These two models provide corrections that are linear in the dissipative currents $\pi^{\mu\nu}$ and Π , and the corrections scale either linearly or quadratically with the hadron momentum p . Consequently, there are values of $\pi^{\mu\nu}$ and Π for which $|\delta f| > f_{\text{eq}}$, even for moderate momenta. Moreover, even for small values of $\pi^{\mu\nu}$ and Π , $|\delta f| > f_{\text{eq}}$ at sufficiently large momenta. In hydrodynamic simulations of heavy-ion collisions, it is not uncommon to encounter situations where $|\delta f| > f_{\text{eq}}$ or $f_i(x, p)$ becomes negative in certain phase-space regions. This is particularly noticeable when particlization is performed near the phase transition, where the bulk viscosity peaks, leading to significant δf_i corrections. These regions, where the assumption $|\delta f| \ll f_{\text{eq}}$ of these models is often pushed

to the limit or even beyond, are generally small enough to not significantly contribute to experimental observables. Commonly, this issue is addressed by regulating the Grad or Chapman-Enskog viscous corrections to prevent $|\delta f| > f_{\text{eq}}$ and by ignoring the fluid cells where $f_i(x, p)$ becomes negative. Although this approach may violate conservation laws (39,40) at hadronization, the deviations of the regulated $f_i(x, p)$ from the original spectra are usually small, except for very soft or high-momentum particles.

The necessity for regulating linearized viscous corrections has motivated the development of models aiming to resum the viscous corrections to all orders and provide positive-definite “modified equilibrium distributions.” The PTB, PTM, and PTMA distributions^{263–265} serve this purpose by incorporating the effects of viscous pressures into the arguments of the exponential function characterizing the equilibrium distribution outlined in Eq. (14). This is achieved by introducing effective temperature and chemical potential, effectively transforming Eq. (14) into a quasiequilibrium distribution. In practice, the PTMA distribution is more suitable for use on freeze-out hypersurfaces constructed from anisotropic hydrodynamic simulations. It is worth noting that, in contrast to the unregulated linearized Grad and Chapman-Enskog distributions, the PTB, PTM, and PTMA distributions do not exactly satisfy the matching constraint Eq. (40) when the viscous stresses are large. A comparison of particle spectra and p_T -differential elliptic flow coefficients from the Cooper-Frye formula, computed with the modified equilibrium distribution and with linearized viscous corrections, is presented in Ref.²⁶⁵ The Maximum Entropy distribution, whose features are yet to be fully explored, constitutes a novel type of positive-definite particle distribution. It introduces dissipative corrections to the local thermal equilibrium distribution by maximizing entropy and does not rely on any uncontrolled assumptions about the microscopic dynamics of the distribution function.

Another source of negative contributions to Eq. (38) arises from regions on the hypersurface with a spacelike normal vector (i.e., $d^3\sigma \cdot d^3\sigma < 0$), where certain momenta satisfy $p \cdot d^3\sigma < 0$. This indicates that the momenta are directed toward the surface elements, representing particles flowing into the hydrodynamic region and subsequently being reabsorbed by the fireball, i.e., the backflow. Various methods exist to handle these types of negative contributions.²⁶⁶ The first approach is simply to neglect the negative contribution.²⁶⁶ However, since contributions from all momenta are required to construct the conserved currents at a position x , discarding contributions from momenta with $p \cdot d^3\sigma < 0$ would violate current con-

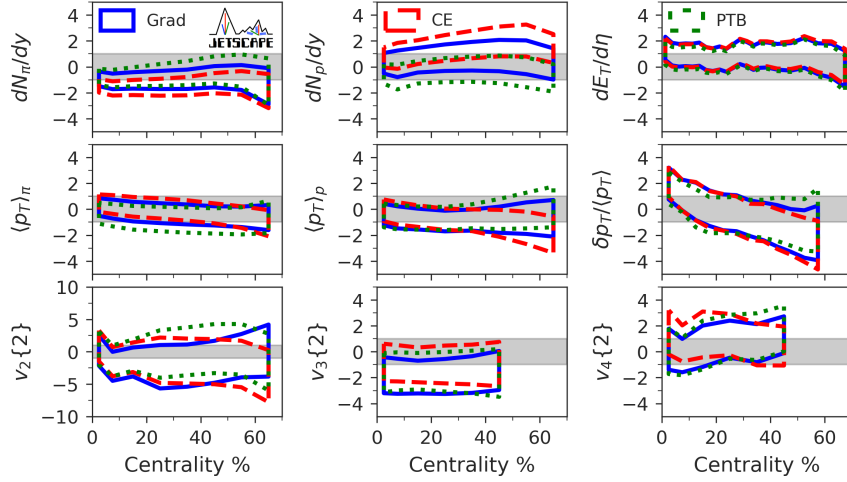


Fig. 9.: The 90% credible intervals of the posterior distribution of observables for Pb+Pb collisions at the LHC as functions of centrality, considering various particlization models. The vertical axis represents the model discrepancy in units of the experimental standard deviation. Figure from Ref. ¹⁴³

servation. A second method for handling the backflow has been to remove particles from the hadronic cascade that cross back into the hydrodynamic region.²⁶⁷ However, the numerical cost associated with tracking the backflow would be high, as it is challenging to find a robust algorithm that avoids constant checks for backflows. A third method is, instead of tracking particles relative to the interface, to simulate the evolution of particles emitted with negative weights.²⁶⁶ Studies on negative contributions stemming from backflow can be found in Refs. ^{256,268,269}

It is worth noting that, given an off-equilibrium correction model, one can calculate $f_i(x, p)$ in Eq. (41), and thus determine the current $N^\mu(x)$ and energy-momentum tensor $T^{\mu\nu}(x)$ using the *smooth* Cooper-Frye distribution. In this scenario, there is no need to sample particles, eliminating the requirement to interpret Eq. (38) as a probability distribution. Consequently, there is no concern about it going negative, and thus, no need to regulate δf_i or discard any fluid cells. One can assess the performance of models for $\delta f_i(x, p)$ by comparing the constructed $N^\mu(x)$ and $T^{\mu\nu}(x)$ from $f_i(x, p)$ with those obtained from the hydrodynamic evolution on the hypersurface, as discussed in. ^{263,265} A well-designed model of $\delta f_i(x, p)$ should yield a good match between them. Finally, it is crucial to acknowledge

that the selection of a dissipative correction model involves irreducible theoretical ambiguity. Therefore, it is logical to inquire about the constraints that experimental data may provide on models of dissipative corrections to the local equilibrium distribution function. For example, a recent model-to-data analysis quantifying the theoretical uncertainties associated with the particlization process in heavy-ion collisions was reported in Ref.^{142,143} (see Fig. 9).

2.3.3. *Statistical ensembles and sampling algorithms*

To calculate the off-equilibrium corrections δf_i and subsequently apply the Cooper-Frye prescription (38) for obtaining the momentum distribution of particle species, several key elements are required. These include the hydrodynamic fields, such as $(T, \mu_B, \mu_Q, \mu_S, u^\mu)$, as well as dissipative variables like $\pi^{\mu\nu}$, Π , n_q^μ , at each spacetime point x , on the freeze-out hypersurface. Furthermore, the spacetime-dependent normal vector of the hypersurface itself, $d^3\sigma_\mu(x)$, is also essential for this process. The aforementioned Cornelius routine can construct such a 4-dimensional hypersurface $\Sigma^\mu(x)$ with the above required elements in the context of (3+1)-dimensional hydrodynamic simulations. In practice, on each fluid cell on the hypersurface, the distributions given by Eq. (38) are Monte Carlo sampled to generate particles with well-defined positions and momenta. The primary task of a hadronic sampler is to faithfully sample particles whose probabilities follow these distributions. Several samplers exist in the field, including *Therminator*,²⁷⁰ *iSS*,²⁷¹ *iS3D*,²⁶⁴ *Microcanonical Sampler*,²⁷² and *FIST-Sampler*.²⁷³

In the most common sampling procedure, the yields of hadrons and resonances are usually sampled independently in each fluid cell from a Poisson distribution, with the particle number obtained from the Cooper-Frye formula interpreted as its mean.²⁷⁴ Since the Poisson distribution is additive, this implies that the yields of all hadron species in the entire space on the hypersurface follow a Poisson distribution as well. Consequently, the samples obtained belong to a grand canonical ensemble (GCE), wherein, when comparing the hydrodynamic quantities and the sampled particles, only the temperature, chemical potentials, and volume are fixed, while the energy, momentum, and charges are conserved only on average. To enhance statistics and reduce statistical uncertainties, particles are often sampled multiple times for each hydrodynamic hypersurface, a method known as the over-sampling method. With over-sampling, grand canonical sampling

is computationally efficient and can provide good approximations for bulk observables, such as transverse momentum spectra and rapidity distributions. Various sampling routines, considering the yields, momenta, viscous corrections, and quantum statistics of different hadron species with various masses, have been developed.^{15,71,264,266,271,272,274} A robust sampling method should yield particle distributions obtained from a large number of oversamples that agree with those from smooth Cooper-Frye distributions. This serves as a common validation method to assess the performance of a hadronic sampler.^{71,239,264,269,271,273}

While grand canonical sampling is arguably consistent with the hydrodynamic description, as seen in the usage of lattice QCD EOS assuming the GCE, recent studies emphasize caution and highlight its potential effects on observables sensitive to event-by-event fluctuations.^{269,272,274–276h} For example, on an event-by-event level, grand canonical sampling has the potential to violate conservation laws at particlization, leading to fluctuations in final particle multiplicity. These fluctuations may subsequently impact the selection of centrality classes.²⁵⁶ A comparison with cases that account for global conservation in each event, as demonstrated in Ref.,²⁷⁴ reveals that the differences in bulk observables, such as transverse momentum spectra and rapidity distributions, between the two approaches are expected to be more pronounced for lower collision energies, smaller collision systems, and rare hadron species. The potential effects on observables involving fluctuations and correlations are of particular interest, especially in the context of searching for the critical point. Therefore, we require a particlization routine that can avoid introducing unphysical fluctuations due to the sampling method, while preserving the physical fluctuations, whether critical or thermal, from the hydrodynamic evolution properly.

The effects of assuming different statistical ensembles have been studied by comparing grand canonical sampling to other cases, such as microcanonical sampling, where conservation laws are fulfilled for the entire freeze-out hypersurface globally in every event.^{15,256,274} If this holds not only for the entire hypersurface but also for smaller spacetime regions, it is referred to as local microcanonical sampling. Refs.^{269,272} implemented local microcanonical sampling, where conservation laws are satisfied on “patches” which are space-time regions smaller than the entire surface but still containing many particles. Due to the conservation laws, the sampled particles of different

^hThe fluctuations due to sampling on a hydrodynamic hypersurface differ from the fluctuations arising from an ensemble of hydrodynamic events, which result from factors such as initial condition fluctuations and thermal fluctuations.

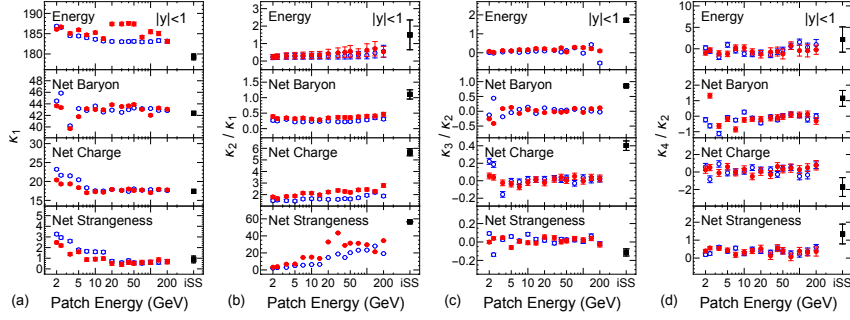


Fig. 10.: Cumulants or cumulant ratios of conserved quantities for particles within a rapidity range $|y| < 1$ as a function of patch energies. The results obtained by the iSS sampler assume the GCE sampling method. From top to bottom: energy, net baryon number, net electric charge, and net strangeness, respectively. Figure from Ref.²⁶⁹

species are found to be correlated, deviating from the conventional grand canonical sampling method with no such constraints (see Fig. 10). Various effects, including suppression in p_T spectra and enhancement in $v_2(p_T)$ for protons at high p_T , stronger suppression of fluctuations, and enhancement of correlations, were observed. They found that many effects, particularly fluctuations and correlations, do not vanish even in the thermodynamic limit. The effects of over-sampling on the net baryon number cumulants were also studied.²⁷⁶ It was found that the commonly used finite particle number sampling procedure introduces an additional Poissonian contribution when global baryon number conservation is absent or multinomial if global baryon number conservation is enforced. This introduces an increase in the extracted moments of the baryon number distribution.

The above sampling methods of the Cooper-Frye formula, even when considering off-equilibrium corrections, generate an ensemble of particles corresponding to an ideal hadron resonance gas with no interactions. Certainly, the particles could exhibit correlations due to the collective motion inherited from the hydrodynamic expansion. Therefore, these existing methods are not suitable for analyzing fluctuation signals beyond the physics of an ideal hadron gas. Extensions of the Cooper-Frye procedure are necessary to incorporate additional physics, such as extending the ideal HRG to include short-range repulsive interactions.²³⁷ A particleization routine appropriate for describing event-by-event fluctuations encoded in the EOS of such interacting HRG models is implemented in

FIST-Sampler.^{273,277} The short-range repulsion between particles is implemented through a rejection sampling step, which prohibits any pair of particles from overlapping in coordinate space. This step effectively models the effect of hard-core repulsion.

Moreover, it is crucial to maintain the critical correlations in coordinate space, which are propagated during the hydrodynamic evolution, and translate them into correlations in momentum space among the particles. This preservation is essential for the search for the critical point through model-data comparison. Attempts have been made to calculate (without sampling) correlations of multiplicity fluctuations at different rapidities from off-equilibrium critical fluctuations propagated in the hydrodynamic stage (see Sec. 4).

2.4. Hadronic afterburner

The last component of a multistage approach to describing heavy-ion collision dynamics, known as the hadronic afterburner, evolves hadrons from particlization to the last scattering (kinetic freeze-out). Physically, this stage describes a gas, consisting of hundreds of hadronic species, which is expanding and cooling. Throughout this process, inelastic collisions become infrequent and, consequently, chemical equilibration times become much longer than the lifetime of the hadronic stage, which means that chemical equilibrium ceases to be preserved.^{123,278} Similarly, local kinetic equilibrium is also difficult to maintain because with the expanding volume V , heavy particles cool faster ($T \propto 1/V^{2/3}$) than nearly massless particles ($T \propto 1/V^{1/3}$). Because of these factors, the role of the hadronic afterburner is best fulfilled by dynamic microscopic transport models, which handle the non-equilibrium evolution taking place after the system is particlized.

The crucial influence of including a hadronic afterburner in simulations was discovered when dynamic models attempted to simultaneously describe multiple observables measured at the top RHIC energy of $\sqrt{s_{\text{NN}}} = 200$ GeV. A compilation²⁸⁴ of such attempts within a selection of models^{48,280–283} is shown in Fig. 11 against measurements from the STAR²⁸⁵ and PHENIX²⁷⁹ experiments. The only model describing all shown data simultaneously (labeled as “ π QGP EOS+RQMD, Teaney et al.”) used a hybrid approach, novel at the time, consisting of a hydrodynamic simulation followed by a hadronic afterburner.^{12,280} This allowed the model to use a soft EOS in the hydrodynamic stage, producing results for the differential elliptic flow $v_2(p_T)$, where p_T is the transverse momentum, agreeing with the ex-

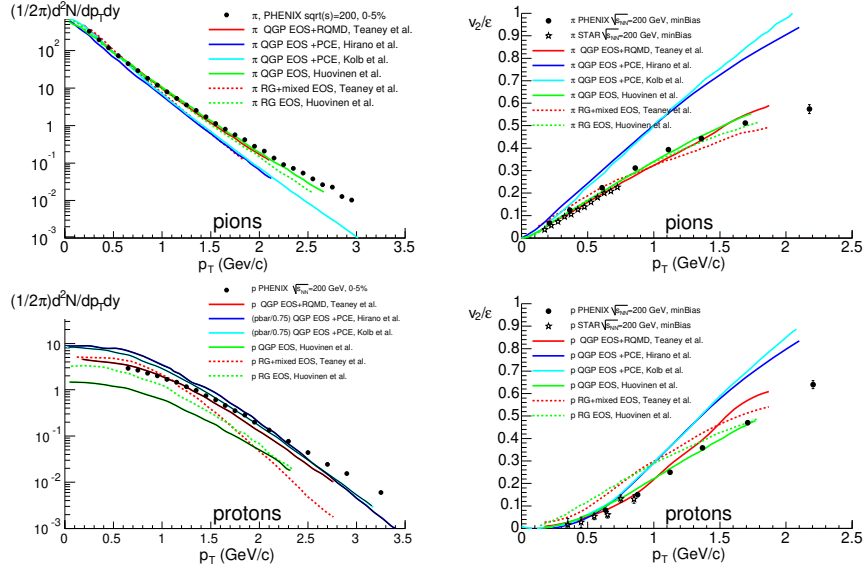


Fig. 11.: The p_T -spectra (*left*) and p_T -differential elliptic flow v_2 scaled by the initial eccentricity ϵ (*right*) for pions (*top*) and protons (*bottom*). The PHENIX data²⁷⁹ is compared with results from simulations within several hydrodynamic models.^{48,280–283} Figure from.²⁸⁴

perimental data, while also obtaining relatively hard p_T -spectra, likewise consistent with experimental measurements, thanks to effects due to rescattering in the afterburner stage.

Elements of hadronic transport approaches as well as recent advancements in modeling are discussed in Sec. 3. Below, we highlight the role of the afterburner stage in arriving at the final results of multistage dynamical simulations. Notably, this role becomes ever more prominent as collision energies decrease and the hadronic stage describes an ever larger fraction of the total evolution time.

2.4.1. Particle yields

Hadronic afterburners change the final particle yields, with the extent of this effect depending on the particle species. At top collider energies, pion and kaon yields are only changed by a few percent, while proton yields can be changed, mainly due to annihilation processes (whose importance is expected to be proportional to the collision energy), by 10% to 30%,¹⁸⁴ see

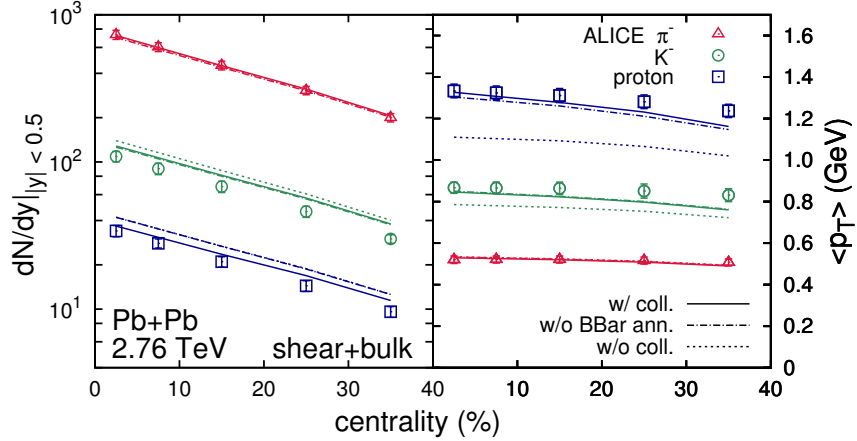


Fig. 12.: The centrality dependence of midrapidity yields (*left*) and mean p_T (*right*) of pions, kaons, and protons in Pb+Pb collisions at $\sqrt{s_{NN}} = 2.76$ TeV. Results from simulations including full UrQMD (labeled “w/ coll.”), UrQMD without $B\bar{B}$ annihilations (labeled “w/o BBar ann.”), and UrQMD without both collisions and annihilations (labeled “w/o coll.”) are shown by the solid, dash-dotted, and dotted curves, respectively, with the ALICE data²⁸⁶ also shown for comparison. Figure from.¹⁸⁴

the left panel in Fig. 12.

2.4.2. Particle spectra

The hadronic stage also shifts spectra, where in particular proton spectra are significantly depleted in the low- p_T region owing to baryon-antibaryon ($B\bar{B}$) annihilations and, at the same time, they are shifted toward higher transverse momenta due to the large cross sections between nucleons and highly energetic pions²⁸⁸ (this effect is sometimes referred to as the “pion wind”), see Fig. 13. Comparisons at the top RHIC energy show that using an afterburner leads to a better description of the experimental data. Similarly, effects due to scatterings in the hadronic stage are found to be crucial at BES energies,⁷¹ with $B\bar{B}$ annihilations also contributing at a significant level.²³⁴

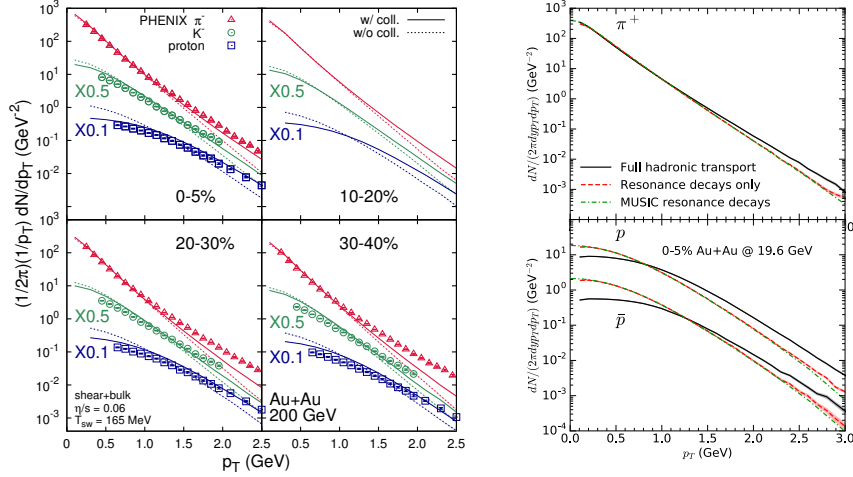


Fig. 13.: *Left*: The p_T -differential spectra of pions, kaons, and protons for centrality classes 0–5%, 10–20%, 20–30%, and 30–40% in Au+Au collisions at $\sqrt{s_{NN}} = 200$ GeV. Results from simulations including full UrQMD (labeled “w/ coll.”) and UrQMD without collisions (labeled “w/o coll.”) are shown by the solid and the dashed curves, respectively, with the PHENIX data²⁸⁷ also shown for comparison. Figure from.¹⁸⁴ *Right*: The p_T -differential spectra of pions, protons, and antiprotons for centrality class 0–5% in Au+Au collisions at $\sqrt{s_{NN}} = 19.6$ GeV. Results from simulations in MUSIC followed by resonance decays, MUSIC followed by hadronic transport with resonance decays only, and MUSIC followed by full hadronic transport with both decays and scatterings are shown as dash-dotted green, dashed red, and solid black lines, respectively. Figure from.⁷¹

2.4.3. Collective flow

At the top RHIC energy, the afterburner stage slightly increases the p_T -differential elliptic flow $v_2(p_T)$ of light mesons while it significantly decreases $v_2(p_T)$ of protons,¹⁸⁴ which leads to an overall better description of experimental data, see the left panel in Fig. 14 (note that at ultrarelativistic energies, proton and antiproton flow are nearly equal). In contrast, at $\sqrt{s_{NN}} = 19.6$ GeV, the afterburner stage increases the p_T -differential elliptic flow $v_2(p_T)$ of pions significantly; moreover, in the case of $v_2(p_T)$ of protons and antiprotons, the afterburner significantly enhances the medium-to-high- p_T region, while it reduces the flow in the low- p_T region,⁷¹ see the right panel in Fig. 14. These significant increases in flow may be explained by the additional time that the afterburner stage gives the system to convert the remaining spatial eccentricity (which at the BES energies,

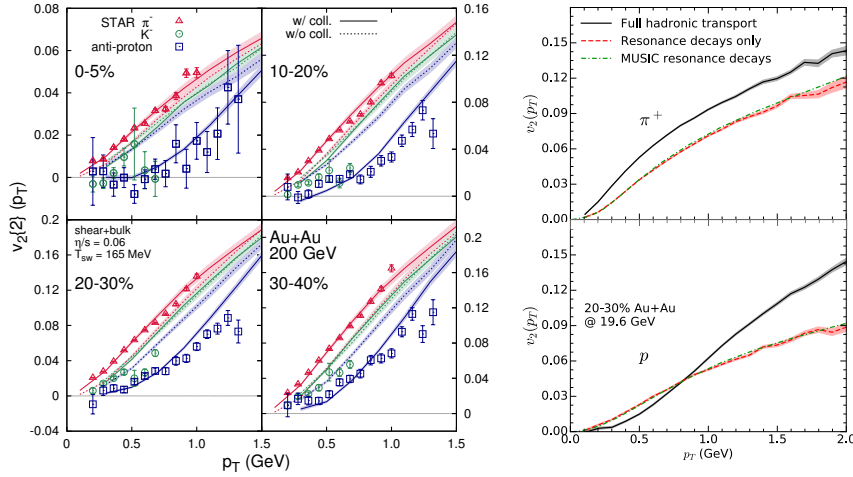


Fig. 14.: *Left:* The p_T -differential elliptic flow $v_2\{2\}$ of identified hadrons for centrality classes 0–5%, 10–20%, 20–30%, and 30–40% in Au+Au collisions at $\sqrt{s_{NN}} = 200$ GeV. Results from simulations including full UrQMD (labeled “w/ coll.”) and UrQMD without collisions (labeled “w/o coll.”) are shown by solid and dashed curves, respectively, with the STAR data²⁸⁹ also shown for comparison. Figure from.¹⁸⁴ *Right:* The p_T -differential elliptic flow v_2 of pions (*top*) and protons (*bottom*) for centrality class 20–30% in Au+Au collisions at $\sqrt{s_{NN}} = 19.6$ GeV. Results from simulations in MUSIC followed by resonance decays, MUSIC followed by hadronic transport with resonance decays only, and MUSIC followed by full hadronic transport with both decays and scatterings are shown as dash-dotted green, dashed red, and solid black lines, respectively. Figure from.⁷¹

in contrast to the top RHIC energy, remains substantial at particlization) into the particle momentum anisotropy. The depletion of the proton and antiproton $v_2(p_T)$ at low values of p_T can be ascribed to the corresponding modification of the proton spectra⁷¹ (see the right panel in Fig. 13).

2.4.4. Future directions

It is important to note that in its use as an afterburner, microscopic transport is usually employed without any mean-field effects on particles’ trajectories (in this mode, it is often referred to as the “hadronic cascade”). This is typically motivated by the corresponding significant reduction in the computational cost as well as by the fact that mean-field effects tend to be negligible at high collision energies (note, however, that this may be a feature of the design: since mean fields used in microscopic trans-

port are most often parametrized in terms of baryon density n_B , it is not surprising that they do not exert any appreciable effects in systems characterized by $n_B \approx 0$). As the collision energy is reduced and both the length of the afterburner stage as well as densities probed during that stage increase, however, mean-field effects are bound to become more important. Consequently, studies of the influence of the hadronic stage on final state observables which include effects due to mean-field particle interactions are vital for BES physics. Such studies should also include investigations of the mean-field influence on correlation and fluctuation observables, which carry a considerable significance in the BES program (see Sec. 4) and which have been previously shown to be strongly affected by processes typical to the afterburner stage such as resonance decays and baryon annihilation.^{16,290–292} Initial studies along this direction have been recently presented.²⁹³

3. Microscopic transport description of dense nuclear matter dynamics

Using heavy-ion collisions to constrain the Quantum Chromodynamics (QCD) equation of state (EOS) at baryon densities n_B larger than the saturation density of nuclear matter n_0 is a long-standing objective in nuclear physics. Initially motivated by the goal of describing nuclear matter at densities reached in neutron stars,^{294,295} studies were further fueled by the discovery of asymptotic freedom^{296,297} which led to the postulation of a hypothesized state of matter in which hadrons are packed so tightly that quarks and gluons are practically free.^{298,299} Following works suggesting³⁰⁰ that highly energetic heavy-ion collisions may probe regions allowing for the study of the Hagedorn “limiting temperature”³⁰¹ (which was also interpreted as a sign of a second-order phase transition³⁰²) and calculations considering the production of “quark matter”,^{303,304} “hadronic plasma”,³⁰⁵ or “quark-gluon plasma”³⁰⁶ in such collisions, experiments colliding heavy-ions at relativistic velocities became a means to probe the phase diagram of QCD.

At this time, studies of the dense nuclear matter EOS are pursued within several approaches. Microscopic many-body calculations within the chiral effective field theory^{307,308} allow one to obtain state-of-the-art predictions on the nuclear matter EOS with quantified uncertainties.^{222,309,310} However, these calculations are only applicable at relatively low temperatures and moderate densities, and in particular are characterized by large uncertainties for densities $n_B \gtrsim 1.5n_0$. Astrophysical observations of neutron

stars can provide constraints on the EOS of neutron-rich matter at zero temperature up to densities several times that of normal nuclear matter,³¹¹ with a particular sensitivity for densities above $2n_0$,^{312,313} while additionally neutron star mergers are expected to probe temperatures on the order of tens of MeV.⁸

In comparison, heavy-ion collisions at the nucleon-nucleon center-of-mass beam energies from about $\sqrt{s_{\text{NN}}} \approx 1.9$ GeV (equivalent to incident kinetic energies, excluding the rest mass, of $E_{\text{kin}} \approx 50$ MeV/nucleon) up to $\sqrt{s_{\text{NN}}} \approx 7.7$ GeV (equivalent to $E_{\text{kin}} \approx 30$ GeV/nucleon) probe nearly isospin-symmetric nuclear matter at densities from a few tenths to about 5 times n_0 .²²² While, at these energies, a large fraction of the collision evolution is out-of-equilibrium, preventing one from using thermodynamic quantities in a well-defined way, one can connect the explored energy densities to temperatures ranging from a few to a few hundreds of MeV.²²² As a result, collisions of heavy nuclei at these energies probe nuclear matter over an impressive range of densities and temperatures, both overlapping with and complementary to other approaches, and, moreover, present the only means of probing the dense nuclear matter EOS in controlled laboratory experiments. The average density and temperature (the latter to the extent that it can be well-defined) of the collision systems are varied by changing the beam energy and collision geometryⁱ. Moreover, certain control of the isospin asymmetry is also possible by varying the isotopic composition of the target and projectile.^{222,315}

A list of selected recent, current, and upcoming efforts using heavy-ion collisions to probe high-density nuclear matter is given in Table 1. Among currently run or analyzed experiments, the Solenoidal Tracker at RHIC (STAR) experiment's Fixed-Target (FXT) campaign of the Beam Energy Scan (BES) II program at the Relativistic Heavy Ion Collider (RHIC) performs gold-gold (Au+Au) collisions in the energy range $\sqrt{s_{\text{NN}}} \in [3.0\text{--}13.1]$ GeV ($E_{\text{kin}} \in [2.92\text{--}89.6]$ GeV/nucleon). The High Acceptance Di-Electron Spectrometer (HADES) experiment at GSI, Germany, collides gold nuclei at $\sqrt{s_{\text{NN}}} = 2.42$ GeV ($E_{\text{kin}} = 1.24$ GeV/nucleon) and silver nuclei at $\sqrt{s_{\text{NN}}} = 2.55$ GeV ($E_{\text{kin}} = 1.58$ GeV/nucleon), while an upcoming campaign at HADES will collide gold nuclei at $\sqrt{s_{\text{NN}}} \in \{1.97, 2.07, 2.16, 2.24\}$ GeV ($E_{\text{kin}} \in \{0.2, 0.4, 0.6, 0.8\}$ GeV/nucleon) and carbon nuclei at $\sqrt{s_{\text{NN}}} \in \{2.16, 2.24\}$ GeV ($E_{\text{kin}} \in \{0.6, 0.8\}$ GeV/nucleon).

ⁱNote, however, that they cannot be varied independently, as compression is always accompanied by heating.^{243,314}

experiment	E_{kin} [GeV/u]	$\sqrt{s_{\text{NN}}}$ [GeV]	ion species
STAR FXT	2.92 – 98.1	3.0 – 13.7	Au
HADES	1.23, 1.58	2.42, 2.55	Au, Ag
HADES	0.2 – 0.8	1.97 – 2.24	Au
(2024)	0.6, 0.8	2.16, 2.24	C
CBM	2.0 – 10.9	2.7 – 4.9	Au
(2028)			other stable
S π RIT	0.27	2.01	$^{108,132}\text{Sn} + ^{112,124}\text{Sn}$
EOS@FRIB	0.175	1.96	$^{56,70}\text{Ni} + ^{58,64}\text{Ni}$
(2025)	0.2	1.97	$^{108,132}\text{Sn} + ^{112,124}\text{Sn}$
EOS@FRIB400	0.4	2.07	$^{104,134}\text{Sn} + ^{112,124}\text{Sn}$
(2030?)			$^{36,52}\text{Ca} + ^{40,48}\text{Ca}$ other unstable+stable

Table 1.: Comparison of different experimental conditions in selected recent, current, and upcoming heavy-ion collision experiments; dates in the brackets indicate the expected timeframe for the upcoming efforts.

The future Compressed Baryonic Mater (CBM) experiment at the Facility for Ion and Antiproton Research (FAIR), Germany, will explore collisions of a variety of stable nuclei at $\sqrt{s_{\text{NN}}} \in [2.7\text{--}4.9]$ GeV ($E_{\text{kin}} \in [2.0, 10.9]$ GeV/nucleon).

Colliding nuclei of varied isotopic composition is a particular strength of facilities where neutron- or proton-rich radioactive beams can be collided on different stable targets, leading to a range of probed isospin densities. Within the recent efforts, the SAMURAI Pion Reconstruction and Ion-Tracker (S π RIT) experiment at the Radioactive Isotope Beam Factory (RIBF) at RIKEN, Japan, performed collisions of tin isotopes at $\sqrt{s_{\text{NN}}} = 2.01$ GeV ($E_{\text{kin}} = 0.27$ GeV/nucleon). In the near future, the recently commissioned Facility for Rare Isotope Beams (FRIB) will provide unique capabilities, colliding the widest range of isotopes available worldwide at up to $\sqrt{s_{\text{NN}}} = 2.01$ GeV ($E_{\text{kin}} = 0.27$ GeV/nucleon), which is expected to yield tight constraints on the isospin-dependence of the EOS up to $n_B \approx 1.5n_0$. The proposed FRIB400 upgrade to $\sqrt{s_{\text{NN}}} = 2.07$ GeV ($E_{\text{kin}} = 0.4$ GeV/nucleon) will further expand this range up to $n_B \approx 2n_0$.³¹⁵

The EOS can be studied in heavy-ion collisions by measuring the final state products of the experiments and constructing observables sensitive to bulk properties of nuclear matter. Any quantitative, and often also qualitative, interpretation of these observables can only be obtained by com-

paring experimental measurements with results of dynamic simulations. Conversely, simulations are also used to identify promising observables. Since collisions in the above-listed energy ranges not only proceed out-of-equilibrium for considerable fractions of the collision time, but are also characterized by prolonged initial compression and final rescattering stages, the appropriate framework for describing the evolution can be provided by microscopic transport simulations. These approaches, which in contrast to hydrodynamics do not require an assumption of local equilibrium, can be used to describe the entire span of a heavy-ion collision: from the initial state of the colliding nuclei, through initial compression and growth of the compression zone, to the development of collective behaviors, decompression of the fireball, and particle scatterings and decays in the final dilute stage of the process.

At the same time, the inherent complexity of heavy-ion collisions in this energy range makes one-to-one comparisons between theory and experiment challenging, especially when attempting to extract an equilibrium property of dense nuclear matter such as the EOS at different densities, temperatures, and isospin asymmetries. To reliably constrain the dense nuclear matter EOS, multiple complex aspects of the simulations have to be well controlled and understood. The effort required in addressing this challenge is well motivated by the fact that heavy-ion collisions have the potential to provide information on the EOS in a region of the QCD phase diagram which cannot be accessed by any other means.

The structure of this section is as follows: In Sec. 3.1, we give an overview of selected observables identified as promising for constraining the EOS of symmetric nuclear matter. In Sec. 3.2, we briefly review the theoretical foundations of microscopic transport approaches. In Sec. 3.3, we highlight some of the recent developments in modeling low- and intermediate-energy heavy-ion collisions with microscopic transport. Finally, in Sec. 3.4 we discuss selected recent efforts to constrain the dense nuclear matter EOS using comparisons between transport models and experimental data.

3.1. Selected prominent observables for extracting the equation of state

Relativistic heavy-ion collisions proceed through several stages which include the initial impact, development of the compressed region and heating, decompression and cooling, and late-stage rescattering. The influence of the EOS is prominent in nearly all elements of the evolution. The initial

state of the collisions is affected by the EOS through its influence on the structure of the colliding nuclei^{316,317}. Furthermore, whether the EOS is stiff or soft (describing matter that is relatively more or less incompressible, respectively) impacts not only the degree of the compression and the corresponding heating,^{243,314} but also the duration of the compression and decompression stages. Likewise, the EOS affects the yields of particles produced throughout the evolution, in particular influencing scatterings and decays in the late dilute stages of the collision.

Through theoretical considerations and simulations, a number of observables have been identified as sensitive to the EOS, including collective flow, subthreshold meson production, dilepton production, femtoscopic correlations, and light cluster production. Among these, certain observables are more promising for collisions at specific beam energies; for example, subthreshold kaon production is an effective probe of the EOS in collisions at energies where subthreshold production dominates. Below, we review some of these prominent observables used to constrain the EOS.

3.1.1. *Remarks about sensitivity*

While the sensitivity of a given measurement to the EOS can often be demonstrated relatively easily, the fact that heavy-ion observables are constructed out of the final-state particle distributions means that they are often *also* sensitive to multiple additional elements influencing the dynamics of the collisions. Notable examples of such elements include elastic and inelastic scattering cross sections or the initial structure of the colliding nuclei. As a result, quantitative constraints on the EOS depend not only on the particular way in which the EOS is modeled, but also, often substantially, on other features of the collision dynamics.

This has profound consequences for efforts to extract the EOS from comparisons of experimental data to simulation results. Simulations of heavy-ion collisions, especially at lower energies where the system is out of equilibrium for the majority (if not the entirety) of the evolution, must include many complex aspects of the collisions which interplay with each throughout the evolution. For many of these aspects, there is either no clear theoretical guidance as to how they should be modeled, or the theoretical guidance cannot be straightforwardly implemented in simulations, creating the need to rely substantially on phenomenology. Since there are many choices available when choosing how to model a given aspect of the evolution, consequently there are differences in both phenomenological ap-

proaches and numerical solutions employed, which can lead to substantial differences in obtained results.

Because of the above, extracting the EOS from heavy-ion collisions ultimately requires assigning systematic errors connected with both the way in which the EOS is modeled and modeling of other aspects of the collision. In this endeavor, Bayesian analyses of simulation results and experimental data (allowing one to understand the relative importance of different aspects of modeling for final results) as well as controlled comparisons between different transport codes will play a pivotal role. Both of these research directions have been gaining prominence in recent years. Bayesian analyses have already led to a deeper understanding of the interplay between different aspects of the collision dynamics and constraints (with meaningful uncertainties) on, among others, the EOS.^{191,243,244,318} Controlled comparisons between different simulation frameworks are being done within the Transport Model Evaluation Project (TMEP) collaboration, which has extensively studied the influence of both phenomenological assumptions and numerical realizations on numerous components of the simulated collision dynamics and, consequently, observables.³¹⁹ Notably, the TMEP effort has been primarily addressing aspects of simulations which are of importance for studies of the isospin dependence of the EOS, performed at relatively low collisions energies ($\sqrt{s_{NN}} \lesssim 3$ GeV, or $E_{kin} \lesssim 2.9$ GeV/nucleon). A similar effort exploring the Beam Energy Scan regime would be invaluable to explorations of the QCD EOS and phase diagram by providing key insights into the interpretation of currently available and upcoming measurements.

3.1.2. Collective flow

Through its importance for the development and evolution of the compression zone, the EOS influences the transverse expansion of the system. The latter, in turn, is reflected in the final state particle distributions, where in particular angular particle distributions in the transverse plane $dN_i/d\phi$, where the subscript i denotes particle species, are often considered. Given the invariant particle distribution $d^3N_i/(p_T dp_T dy d\phi)$, where p_T is the transverse momentum, y is the rapidity, and ϕ is the azimuthal angle, it is particularly convenient to decompose $dN_i/d\phi$ in terms of its Fourier coefficients v_n ,

$$\frac{d^3N_i}{p_T dp_T dy d\phi} = \frac{d^2N_i}{p_T dp_T dy} \frac{1}{2\pi} \left[1 + \sum_{n=1}^{\infty} 2v_n^{(i)}(p_T, y) \cos(n\phi) \right], \quad (42)$$

from which it follows that

$$v_n^{(i)}(p_T, y) \equiv \frac{\int_0^{2\pi} d\phi \cos(n\phi) \frac{d^3 N_i}{p_T dp_T dy d\phi}}{\int_0^{2\pi} d\phi \frac{d^3 N_i}{p_T dp_T dy d\phi}} \quad (43)$$

$$= \langle \cos(n\phi) \rangle = \frac{1}{N_i} \sum_{k=1}^{N_i} \cos(n\phi_k) \Big|_{p_T, y}, \quad (44)$$

where the sum in the last expression is performed over all particles of species i which have transverse momentum p_T and rapidity y . Since the Fourier coefficients $v_n^{(i)}(p_T, y)$ reflect the direction of particles' momenta averaged over the entire system, they are referred to as "collective flow". To tease out broad characteristics of this collective motion, flow observables $v_n^{(i)}(p_T, y)$ are often further integrated over p_T , y , or both.

The influence of the EOS on the collective flow is especially prominent at collision energies for which two time scales associated with the collisions are comparable. The first of those is the time necessary for the compression and decompression of matter originating from participant nucleons (that is nucleons trapped in the collision region), while the second is the time of propagation of spectator nucleons (that is nucleons whose trajectories do not directly cross the initial transverse overlap of the colliding nuclei) past the collision region. The two time scales are similar for collision energies ranging from around $\sqrt{s_{\text{NN}}} \approx 2$ GeV ($E_{\text{kin}} \approx 0.2$ GeV/nucleon) to $\sqrt{s_{\text{NN}}} \approx 10$ GeV ($E_{\text{kin}} \approx 50$ GeV/nucleon), and consequently in this regime the development of flows $v_n^{(i)}$ is heavily affected by the interplay between the initial geometry of the colliding system, the gradual creation of the compression zone from incoming participants and its subsequent expansion, and the movement of spectator nucleons. It has been shown in numerous hydrodynamic ^{320–326} and microscopic transport^{241,243,327–332} models that the resulting collective motion of the system, which can be measured to a very high precision, is very sensitive to the EOS, placing flow among the central observables used for constraining the EOS.

An asymmetry in the compression and expansion of the collision zone is necessary for the development of finite v_n . A substantial asymmetry is obtained in off-central collisions where the initial overlap of the colliding nuclei has an approximately elliptical shape (see Fig. 15), which leads to pressure gradients within the collision zone (that are larger along the short axis of the ellipsoid) and supports the development of a non-zero $v_1(p_T, y)$, referred to as the directed flow, and $v_2(p_T, y)$, known as the elliptic flow. The particular values of such generated flow coefficients depend

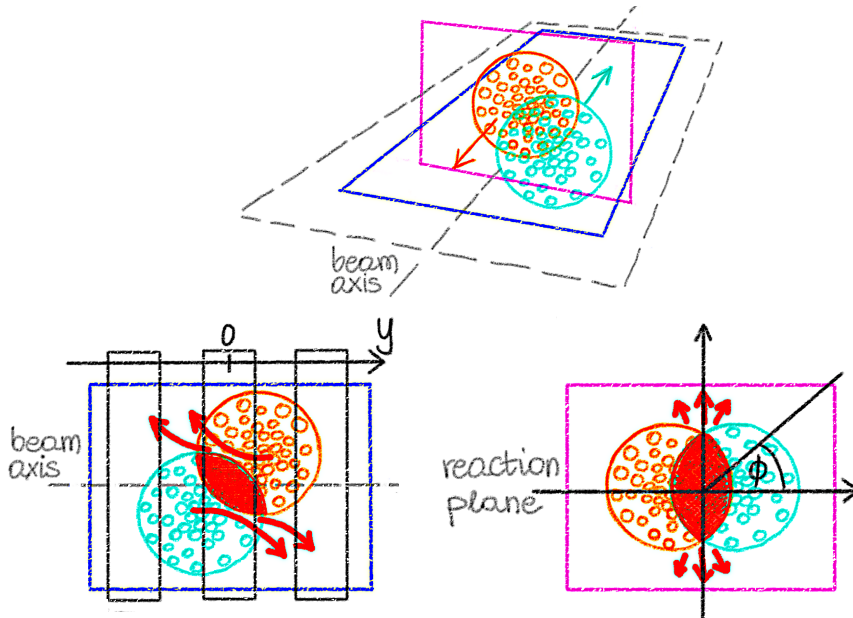


Fig. 15.: A sketch picturing the geometry of a heavy-ion collision system at the moment of impact (*top*) as well as the development of the directed (*bottom left*) and elliptic (*bottom right*) flow. The solid red regions indicate the compressed matter created in the aftermath of the impact, while the red arrows indicate the motion of matter in response to interaction with the dense collision zone (*middle*) and during its subsequent decompression (*right*). The presented picture is valid in collisions at energies for which the time scale associated with the compression and decompression of the collision zone and the time scale of propagation of spectator nucleons past the collision region are comparable. Note that two nuclei moving at relativistic speeds should be Lorentz contracted, however, the sketch omits the contraction for clarity.

on the aforementioned intrinsic time scales of the collision and the EOS. In the case in which the spectator nucleons leave the collision region before the collision zone starts to expand, nothing obstructs the expansion of the created fireball to follow the directions of the largest pressure gradients, which results in a preferential emission in directions parallel to the reaction plane (“in-plane” emission), directly corresponding to the shape of the collision region which can be quantified, e.g., by its eccentricity.²⁸⁴ This, in turn, leads to positive values of $v_2(p_T, y)$, while the values of $v_1(p_T, y)$ in this case are zero (up to event-by-event contributions from random fluctuations) due to the symmetry. On the other hand, if the spectators remain

in the close vicinity of the collision region, they may block the in-plane motion of the expanding fireball and thus lead to negative values of $v_2(p_T, y)$ (“out-of-plane” emission). The degree of this blocking depends strongly on the EOS, with more blocking (and a more negative v_2) occurring for a stiffer (more repulsive) EOS. Moreover, while the directed flow at midrapidity, $v_1(p_T, y = 0)$, remains equal to zero (up to random event-by-event fluctuations) also in this case due to symmetry, it acquires non-zero values at finite values of rapidity due to the interaction between the spectators and the collision zone.³³³ Here, if the spectators whose trajectories coincide with the positive beam direction are deflected in such a way that the values of $v_1(p_T, y > 0)$ are positive, then conversely the spectators going in the negative beam direction will be deflected in the opposite direction, thus leading to negative values of $v_1(p_T, y < 0)$. (Note that because of the symmetry, one should have $v_1(p_T, y = y') = -v_1(p_T, y = -y')$, again up to random fluctuations, as well as $\int dy v_1(p_T, y) = 0$.) The value of the directed flow at a given value of y as well as its slope at midrapidity, $dv_1/dy|_{y=0}$, depend on the EOS, with stiffer (softer) EOSs leading to larger (smaller) values of $dv_1/dy|_{y=0}$. Notably, several studies^{323,334} even suggest $dv_1/dy|_{y=0} < 0$ for EOSs exhibiting a first-order phase transition, for which the interactions between the collision zone and the spectators may become attractive instead of repulsive.

While the sensitivity of the directed and elliptic flow to the EOS has been extensively explored and confirmed in multiple studies considering various possible behaviors of the EOS with baryon density,^{241,243} it is also well-known that the extraction of the EOS from flow observables is heavily affected by the momentum dependence of interactions.^{329,332,335–337} Therefore, studies using flow observables to extract the EOS should also address the influence of the momentum dependence, which can be independently constrained using data from peripheral collisions^{329,336} where the effects due to the unknown density-dependence of the EOS diminish due to lower probed densities. Similarly, flow results are also affected by the modification of elementary cross-sections in the medium, which can be calculated in models^{338–343} and the necessity of which can be inferred from measured stopping observables that tend to be overpredicted in models using free-space cross sections.^{338,344–346} Still, the in-medium dependence of cross-sections is not well constrained, especially at energies relevant to the BES program. Flow results have also been shown in the past to be influenced by the degrees of freedom considered in simulations, in particular by inclu-

sion of high-mass resonant states. These states are produced in significant amounts at collision energies $\sqrt{s_{\text{NN}}} \gtrsim 2.3$ GeV ($E_{\text{kin}} \gtrsim 1$ GeV/nucleon) and, by providing additional production channels which can use some part of the collision energy, affect the degree of initial compression and the spectrum of emitted and absorbed mesons, with non-negligible implications for the collective flow.³⁴⁷ Consequently, simulations aimed at inferring the EOS from flow observables should include all relevant resonant species as well as provide a reliable description of meson production. Finally, flow results can be also affected by production algorithms for deuteron, triton, and other light clusters included in simulations.³⁴⁸ While several modeling choices are available,^{349–354} they still display certain shortcomings: models based on coalescence typically do not take into account the influence of light clusters on the evolution, while approaches based on dynamical production of clusters through the collision term in transport equations are impeded by increasing complexity when attempting to include heavier clusters which are characterized by more and more production channels. Moreover, cluster production is ultimately related to intermediate-range correlations and quantum effects, and as such touches on fundamental properties of nuclear matter reaching beyond the classical one-body description typical for microscopic transport. Nevertheless, identifying successful phenomenological approaches to cluster production can help shed light on the underlying fundamental mechanisms.

3.1.3. Light cluster production

Recently, light nuclei production itself has been suggested as a probe of the EOS and, in particular, the existence and location of the QCD first-order phase transition region with the corresponding critical point.^{355,356} The key observation made was that fluctuations in the phase-space density, which are expected to be significantly enhanced both inside the spinodal region of a first-order phase transition and in the vicinity of a critical point and (see Sec. 4), may lead to an enhanced production of light nuclear clusters. Specifically, based on the coalescence model, it was observed³⁵⁵ that the yield ratio $N_t N_p / N_d^2$, where N_t , N_p , and N_d are triton, proton, and deuteron yields, respectively, is sensitive to relative fluctuations in neutron density $\Delta n_n \equiv \langle (\delta n_n)^2 \rangle / \langle n_n \rangle^2$,

$$\frac{N_t N_p}{N_d^2} = \frac{1}{2\sqrt{3}} \frac{1 + 2C_{np} + \Delta n_n}{(1 + C_{np})^2}, \quad (45)$$

where $C_{np} \equiv \langle \delta n_n \delta n_p \rangle / (\langle n_n \rangle \langle n_p \rangle)$ denotes proton-neutron density correlation. Moreover, combined heavy-ion collision data spanning the energy range $\sqrt{s_{NN}} \approx 3\text{--}200$ GeV ($E_{\text{kin}} \approx 3\text{--}21,300$ GeV/nucleon)^{357–361} shows a nonmonotonic behavior in the dependence of the $N_t N_p / N_d^2$ ratio on collision energy, which suggests enhanced spatial density fluctuations in the region of the phase diagram probed by the corresponding beam energies. However, firm conclusions are prevented by the fact that the available models (both dynamical and thermal) disagree on the $N_t N_p / N_d^2$ ratio even when using the same EOS *without* a critical point, thus disagreeing about the trivial baseline for the measurement. Thus, using this observable to constrain the EOS requires further studies on cluster production, with a particular emphasis on dynamical studies at intermediate and low collision energies where the intriguing behavior of the light nuclei yield ratio occurs. Some work in this direction has already been done.^{362–364}

3.1.4. Femtoscopic correlations

Two-particle correlations at small relative momentum, also known as femtoscopic or Hanbury-Brown–Twiss (HBT) correlations, have been proposed as a sensitive probe of the EOS. Given that correlations due to final-state interactions are stronger between particles that are emitted close to each other in space or time, HBT correlations provide a tool to investigate the spatial and temporal properties of particle emission as well as the dynamics of the emitting source. In particular, information about not only the spatial, but also temporal extent of the source can be extracted from measurements of femtoscopic radii R_{long} , R_{out} , R_{side} .³⁶⁵ Here, R_{long} is a measure of the source size along the longitudinal (beam) axis, R_{out} measures the source size in the direction of the average transverse momentum of the correlated pair, while R_{side} measures the source size in the direction perpendicular to both R_{long} and R_{out} . Since the femtoscopic radii provide information about the space-time extent of the studied source, they are often also referred to as interferometry.

It was pointed out^{366–368} that if a heavy-ion collision evolves through a first-order phase transition, which both allows the system to compress more and prolongs the expansion of the fireball due to the softening of the EOS in the transition region, then this will increase the size of the emission region in the radial direction. In that case, R_{out} is comparatively larger, and in particular the femtoscopic radii will satisfy $R_{\text{out}} \gg R_{\text{side}}$. As a consequence, both the difference $R_{\text{out}}^2 - R_{\text{side}}^2$ and the ratio $R_{\text{out}}/R_{\text{side}}$ can

be used to constrain the EOS. (We note here that while the difference of the femtoscopic radii can be directly linked to the emission duration $\Delta\tau$ through $R_{\text{out}}^2 - R_{\text{side}}^2 = \beta_T^2 \Delta\tau$,^{369–371} where β_T is the transverse velocity of the emitted particles, this relationship is only reliable for systems without transverse collective flow; if flow is present, extracting $\Delta\tau$ is impeded by significant model dependence.^{372–374})

The sensitivity of femtoscopic correlations to the EOS has been demonstrated in a Bayesian analysis of high-energy heavy-ion collisions, constraining the EOS at near-zero baryon density.^{191,318} Recent work³⁷⁵ has addressed the possibility of using HBT correlations to constrain the EOS of dense nuclear matter in collision energy range $\sqrt{s_{\text{NN}}} = 2.4\text{--}7.7$ GeV, explored in the HADES experiment, the FXT campaign of the RHIC BES II program, and the future CBM experiment.

On the experimental side, femtoscopic measurements have been dominated by pion interferometry.^{373,376–379} However, recently more attention has been given to femtoscopic correlations between nucleons³⁸⁰ as well as light nuclei.³⁸¹ Preliminary results from the HADES experiment³⁸¹ show significant differences between proton–proton, proton–deuteron, and proton–Helium-3 as well as proton–Helium-3 and proton–triton correlations, suggesting changes in strong interaction effects between these systems. Moreover, the results are shown to be affected by decays of exotic Lithium-4 and excited Helium-4 states, stressing the need for modeling light nuclei production in this energy region.

3.2. *Microscopic transport models*

Microscopic transport models can be divided into models of the Boltzmann-Uehling-Uhlenbeck (BUU) type (also referred to as the Boltzmann-Vlasov type) and models of the Quantum Molecular Dynamics (QMD) type. In both cases, with the exception of very limited simple considerations, the complexity of the underlying non-linear equations means that the models cannot be solved analytically. Instead, insights into the evolution of described systems is gained through dynamical simulations. Reviews discussing many of the currently used models, including particular choices of phenomenological approaches and details of implementation as well as their consequences for obtained results, are available.^{36,319,382,383} Below, we give a brief description of each type of models, largely based on similar summaries,^{319,384} to facilitate the discussion that follows.

3.2.1. Boltzmann-Uehling-Uhlenbeck models

In BUU approaches, the evolution of a system of particles, involving N particle species indexed by n , is described by a set of coupled differential equations for the evolution of the phase space distribution function of each species $f_n(t, \mathbf{x}, \mathbf{p})$,

$$\left[\frac{\partial}{\partial t} + \frac{d\mathbf{x}}{dt} \frac{\partial}{\partial \mathbf{x}} + \frac{d\mathbf{p}}{dt} \frac{\partial}{\partial \mathbf{p}} \right] f_n(t, \mathbf{x}, \mathbf{p}) = I_{\text{coll}}[\{f_n\}], \quad (46)$$

where the terms on the left-hand side are equivalent to a total time derivative of $f_n(t, \mathbf{x}, \mathbf{p})$ and describe the drift of particles in the phase space, while $I_{\text{coll}}[\{f_n\}]$ is known as the collision term or the collision integral. In the absence of particle-particle collisions as well as particle production (i.e., resonance excitation) and decays, the right-hand side of the above equation is identically equal to zero. This, in fact, follows from the Liouville theorem and can be intuitively understood by realizing that the total time derivative on the left-hand side, $df_n(t, \mathbf{x}, \mathbf{p})/dt$, describes changes that $f_n(t, \mathbf{x}, \mathbf{p})$ undergoes in time from the perspective of an observer traveling along the system's trajectory, $(\mathbf{x}(t), \mathbf{p}(t))$. When collisions, particle production, and decays, which either add or remove particles from a given infinitesimal volume of the phase space, are absent, the distribution function remains constant in the subvolume moving along the trajectories of particles. (We additionally note here that these trajectories are realized both by changes in particles' positions due to propagation as well as by changes in particles' momenta due to forces acting on the particles, and as such may be far from trivial.) On the other hand, if collisions, particle production, or decays are allowed to occur, the corresponding changes in the distribution function are reflected in $I_{\text{coll}}[\{f_n\}]$ which sums over all possible cross sections and production or decay channels between considered particle species. Typically, within the derivation of Eq. (46) from the Bogoliubov-Born-Green-Kirkwood-Yvon (BBGKY) hierarchy,³⁸⁵ the contribution to the collision integral due to two-body scattering with a particle of species k , $p_n + p_k \rightarrow p'_n + p'_k$, formally takes the form

$$I_{\text{coll}}[\{f_n\}] = \sum_k g_k \int \frac{d^3 p_k}{(2\pi)^3} d\Omega' \times v_{nk} \frac{d\sigma_{nk}}{d\Omega'} \left[f'_n f'_k (1 - af_n)(1 - af_k) - f_n f_k (1 - af'_n)(1 - af'_k) \right], \quad (47)$$

where the sum runs over all considered particle species, g_k is the degeneracy (which takes into account spin and may also include isospin degeneracy),

the distribution functions are all taken at the same spacetime point (t, \mathbf{x}) , the outgoing momenta p'_n and p'_k are determined by the scattering angle Ω' and energy-momentum conservation, $d\sigma_{nk}/d\Omega'$ is the differential cross section for scattering, and v_{nk} is the relative velocity,

$$v_{nk} = \frac{\sqrt{(p_n \cdot p_k)^2 - m_n^2 m_k^2}}{p_n^0 p_k^0}, \quad (48)$$

where m_n and m_k are bare masses of particle species n and k , respectively. Furthermore, the first term in the square bracket is known as the gain term, given that it provides the phase space factor related to particles scattering *into* the state with momentum p_n , while the second term is known as the loss term since it describes particles scattering *out of* the p_n state; here, effects due to Pauli blocking or Bose enhancement are taken into account by factors of the form $(1 - af)$, where $a = 1$ for fermions and $a = -1$ for bosons.

Numerically, Eq. (46) is solved based on the method of test particles, which can be formally derived³⁸⁶ as well as introduced in a more pedestrian way.²⁴³ Within this approach, the continuous distribution function $f_n(t, \mathbf{x}, \mathbf{p})$ describing A particles of species n is approximated by a discrete distribution of a large number $N_T A$ of test particles occupying phase space coordinates $(t, \mathbf{x}_i, \mathbf{p}_i)$,

$$f_n(t, \mathbf{x}, \mathbf{p}) \approx \frac{1}{N_T} \sum_{i=1}^{N_T A} \delta^3(\mathbf{x} - \mathbf{x}_i(t)) \delta^3(\mathbf{p} - \mathbf{p}_i(t)), \quad (49)$$

where $N_T \gg 1$ is the number of test particles per particle. Note that the introduction of the normalization factor of $1/N_T$ preserves the interpretation of f_n as the number of “real” particles in a given infinitesimal volume of the phase space. The phase space evolution of test particles proceeds according to single-particle equations of motion, which are obtained by inserting Eq. (49) into Eq. (46),

$$\frac{d\mathbf{x}_i}{dt} = \frac{\mathbf{p}_i}{p_i^0} \equiv \frac{d\mathbf{x}_i}{d\mathbf{p}_i}, \quad (50)$$

$$\frac{d\mathbf{p}_i}{dt} = -\nabla U_i \equiv -\frac{d\varepsilon_i}{d\mathbf{x}_i}, \quad (51)$$

where ε_i is the single-particle energy (including a possible mean-field potential term), and by enabling the test particles to undergo allowed scatterings, resonance excitations, and decays using a chosen algorithm for simulating the collision term of Eq. (46). Such algorithms can be based on, e.g., the geometric criterion for scattering^{36,387} or stochastic scattering rates^{349,388,389}

informed either by experimental cross section measurements or calculated from, e.g., the principle of detailed balance. To preserve the physical average number of scatterings per particle in a heavily “oversampled” system of $N_T A$ test particles, one further scales the cross sections as $\sigma \rightarrow \sigma/N_T$, where σ is a given physical cross section.

Altogether, this yields the time evolution of a system of test particles which follow the trajectories of “real” particles in the phase space. In other words, using Eq. (49) to approximate the phase space distribution at the initial time t_0 , $f_n(t_0, \mathbf{x}, \mathbf{p})$, and evolving thus obtained system of test particles effectively solves Eq. (46) (i.e., yields the time evolution of the continuous phase space distribution $f_n(t, \mathbf{x}, \mathbf{p})$), since at any time $t > t_0$ the evolved test particles can be always used to again approximate $f_n(t, \mathbf{x}, \mathbf{p})$ provided that the evolution of each test particle appropriately mimics the evolution of a “real” particle under the same conditions.

Unless a very large number of test particles per particle, on the order of $N_T = \mathcal{O}(1000)$, is used, the approximation of the phase space distribution function given in Eq. (49) fluctuates strongly due to effects related to the finite number of samples (often also referred to as the numerical noise). This is of great importance to the success of the method, as the accuracy of calculating local values of f_n is crucial for several key elements of the simulation, including the evaluation of single-particle mean-field potentials U_i entering the equations of motion, Eq. (51), and the corresponding mean-field dynamics³⁹⁰ or calculation of Pauli blocking factors³⁹¹ which inform the probability of a particle to scatter or decay into a given final state. On the other hand, using very large numbers of test particles per particle N_T comes at a significant numerical cost which is especially prominent for algorithms performing scatterings, which scale with the square of the total number of particles in an event, $\propto N_T^2$. For this reason, generalizations of Eq. (49) are often used where the Dirac delta functions are substituted by profile functions (also known as smearing functions) in coordinate and momentum space,

$$f_n(t, \mathbf{x}, \mathbf{p}) \approx \frac{1}{N_T} \sum_{i=1}^N G_{\mathbf{x}}(\mathbf{x} - \mathbf{x}_i(t)) G_{\mathbf{p}}(\mathbf{p} - \mathbf{p}_i(t)), \quad (52)$$

which “distribute” the contribution of a test particle to the phase space density over a finite volume and as a result reduce local fluctuations due to a finite number of samples, thus allowing for successfully employing smaller values of N_T . Most often, non-Dirac-delta profile functions are used only for distributing the particles over the coordinate space, usually over volumes

on the order of $\Delta V = \mathcal{O}(1 \text{ fm}^3)$. Popular choices for the shapes of the smearing profiles include triangular functions and Gaussians, where the latter have been also used to achieve a fully covariant description.³⁹² Note that because Eq. (49) was used to derive the single-particle equations of motion, Eq. (49), from the BUU equation, Eq. (46), using a more general form as shown in Eq. (52) will, in general, lead to different equations of motion for the test particles. A systematic way of accounting for the form of the smearing function both in calculating the phase space density and in single-particle equations of motion has been developed and is known as the lattice-Hamiltonian method.³⁹³ Besides formal consistency, this approach yields equations of motion that strictly preserve conservation of the total energy,³⁹⁴ which otherwise can be more or less broken.^{395,396} Nevertheless, while multiple codes adopt the lattice-Hamiltonian method, its use is far from widespread.³¹⁹

We note here that while the BUU equation presented in Eq. (46) is not written in a manifestly covariant way, it can be shown that it is relativistically covariant. In the collision term, p_k^0 in the denominator of v_{nk} can be combined with the momentum integration to obtain an invariant integration measure, while the spin-averaged phase space distribution is a Lorentz scalar. Furthermore, both sides of Eq. (46) can be multiplied by p^0 , yielding a covariant derivative on the left-hand side. Consequently, any equations following from the BUU equation, including the single-particle equations of motion, are also relativistically covariant.^{243,396,397} Nevertheless, in practice, covariance is always broken by other elements of the simulation. A trivial example here is using non-relativistic single-particle potentials, however, covariance is also disturbed simply by solving the Boltzmann equation with a *finite* number of test particles, which leads to, e.g., collisions between particles occurring at a finite distance³⁹⁸ or calculations of the mean field at a given point based on particles present within a finite volume around that point, both of which imply instantaneous interaction over a finite distance and explicitly break causality. Formally, these effects disappear in the limit of an infinite number of test particles, and a full Lorentz covariance is restored in that limit.

3.2.2. *Quantum Molecular Dynamics models*

In QMD models, the many-body state of the system is described by a product wave function of single-particle states (which may³⁹⁹ or may not⁴⁰⁰ be antisymmetrized), the latter of which are usually taken to assume a

Gaussian form. Through their use of localized wave packets, QMD models include the description of classical many-body correlations. The time evolution is obtained by evolving the centroids of the wave packets, representing the particles in the system, according to classical molecular dynamics, as well as by introducing collisions and decays in a way similar to that employed in BUU approaches. While QMD models can, in principle, employ two-, three-, and many-body interactions, instead particles are usually evolved with a mean-field potential (similarly to BUU). As such, QMD may be interpreted as derived from the time-dependent Hartree method, where the product trial wave function

$$\Psi(\mathbf{x}_1, \dots, \mathbf{x}_A; t) = \prod_{i=1}^A \phi_i(\mathbf{x}_i; t) \quad (53)$$

employs Gaussian single-particle states,

$$\begin{aligned} \phi_i(\mathbf{x}_i; t) = & \frac{1}{[2\pi(\Delta x)^2]^{3/4}} \\ & \times \exp \left[- \left(\frac{\mathbf{x}_i - \mathbf{X}_i(t)}{2\Delta x} \right)^2 \right] \exp \left[i\mathbf{P}_i(t) \cdot (\mathbf{x}_i - \mathbf{X}_i(t)) \right], \end{aligned} \quad (54)$$

and the centroid positions $\mathbf{X}_i(t)$ and momenta $\mathbf{P}_i(t)$ are identified as variational parameters. With Eq. (53), one can then calculate the 1-body Wigner function,

$$f(\mathbf{x}, \mathbf{p}) = \sum_{i=1}^A \frac{1}{(\Delta x \Delta p)^3} \exp \left[- \frac{(\mathbf{x} - \mathbf{X}_i(t))^2}{2(\Delta x)^2} - \frac{(\mathbf{p} - \mathbf{P}_i(t))^2}{2(\Delta p)^2} \right], \quad (55)$$

where the sum is performed over all single-particle contributions. The QMD ansatz, Eq. (53), and the time-dependent variational principle then lead to the following single-particle equations of motion,

$$\frac{d\mathbf{X}_i}{dt} = \frac{\partial \langle H \rangle}{\partial \mathbf{P}_i}, \quad (56)$$

$$\frac{d\mathbf{P}_i}{dt} = - \frac{\partial \langle H \rangle}{\partial \mathbf{X}_i}, \quad (57)$$

where $\langle H \rangle$ is the expectation value of the many-body Hamiltonian H containing both kinetic and potential energy contributions. In the classical limit, the expectation value of the many-body Hamiltonian can be taken as the sum of single-particle Hamiltonians, $H = \sum_i H_i = \sum_i (K_i + V_i)$, where K_i and V_i denote the kinetic and potential energy of the i th particle. Given V_i dependent on local baryon density $V_i(n_B(\mathbf{X}_j))$ (which can be also

thought of as the *average* potential of a particle at position \mathbf{X}_i), the change in particle's momentum can be then written out explicitly as

$$\frac{d\mathbf{P}_i}{dt} = -\frac{\partial V_i(n_B)}{\partial n_B(\mathbf{X}_i)} \frac{\partial n_B(\mathbf{X}_i)}{\partial \mathbf{X}_i} - \sum_{j \neq i} \frac{\partial V_j(n_B)}{\partial n_B(\mathbf{X}_j)} \frac{\partial n_B(\mathbf{X}_j)}{\partial \mathbf{X}_i}, \quad (58)$$

where the first term accounts for the change in the potential at the location of the i th particle due to a local gradient of density $\partial n_B / \partial \mathbf{X}_i$, while the second term accounts for the change in the potential at the locations of all *other* particles due to changes in \mathbf{X}_i . This underscores the fact that QMD is an n -body theory describing interactions between n nucleons. The local computational frame density at the position of the i th particle \mathbf{X}_i , also sometimes referred to as local interaction density, is calculated by summing contributions from all particles except the i th particle, which given the Gaussian form of the wave packet, Eq. (54), yields

$$n_B(\mathbf{X}_i) = \left(\frac{2(\Delta x)^2}{\pi} \right)^{3/2} \sum_{j \neq i} B_j \exp \left[-\frac{(\mathbf{X}_i - \mathbf{X}_j)^2}{2(\Delta x)^2} \right], \quad (59)$$

where B_j is the baryon number of the j th particle. Note that as a result, $2(\Delta x)^2$ is the effective range parameter of the interaction. Finally, while the propagation of particles in QMD, Eq. (56), can and often is described respecting the laws of special relativity, the change in the momenta of the particles due to a density-dependent potential, Eq. (57), is calculated in a non-relativistic way.

3.2.3. Degrees of freedom

Microscopic transport models are mostly used to describe systems composed of baryons and mesons, in which case the corresponding frameworks are usually referred to as “hadronic transport”. Within this group, simulation codes often differ between each other with respect to the number of degrees of freedom considered. Codes used for the description of heavy-ion collisions at the lowest energies (up to the order of 50 MeV/nucleon in the fixed-target frame) may consider only nucleons and nuclear clusters, including both light clusters (up to alpha particles) and heavy clusters (nuclei with mass numbers on the order of tens of nucleons). Above around 200 MeV/nucleon, pion production starts to play a role, necessitating their inclusion as degrees of freedom. Similarly, around 1 GeV/nucleon there is a need to include kaons in the description of collisions; at the same time, heavy clusters start becoming less abundant in that region. In general, as

the energy is increased, more and more hadronic species are considered, including resonant states, while the importance of even light clusters diminishes. However, which particular degrees of freedom play a dominant role depends on the set of observables that one wants to describe. For example, deuterons may remain important for the description of some proton observables as long as their yield binds a substantial fraction of protons available in the system, which is the case up to rather high energies of $\sqrt{s_{\text{NN}}} \approx 10 \text{ GeV}$ ($E_{\text{kin}} \approx 50 \text{ GeV/nucleon}$).³⁵⁹

Microscopic transport also lends itself to descriptions of parton dynamics. Such approaches include simulations of jet-medium interactions⁴⁰¹ and of heavy-quark dynamics coupled to a dense strongly-interacting medium,^{402,403} where the underlying bulk evolution is provided by relativistic hydrodynamics, and can yield predictions for, e.g., production or elliptic flow of quarkonia. There are also microscopic transport frameworks that can be used for the description of the entire evolution of a heavy-ion collision at high energies.^{34,38,404,405} In these simulations, the dense initial state of the collisions (which, depending on the framework, can be obtained either from an initial state model or from hadronic transport evolution) transitions to a system of strongly-interacting partons which subsequently transition back to hadronic degrees of freedom as the system expands and cools. Such approaches are an alternative to using multi-stage simulations (see Sec. 2) for describing heavy-ion observables even at high and very high energies.

While both of the above-mentioned uses provide for exciting and developing research directions, we will not address them in this review.

3.3. Recent developments relevant to constraining the dense nuclear matter equation of state

As already mentioned in Sec. 3.1.1, and as we will again discuss in Sec. 3.4.3, putting reliable constraints on the EOS does not involve a single observable or an isolated process affecting the evolution. Conversely, there are numerous elements of simulations which may influence the extraction of the EOS from experimental data. Given the above, virtually *any* development of the chosen simulation framework, also beyond the explicit treatment of the EOS, can affect constraints on the EOS. Covering all such recent developments and their influence on the overall performance of the relevant models is beyond the scope of this review. Below, we concentrate on developments related to two most prominent decisions that one needs to make before us-

ing heavy-ion collision data to extract the EOS: the choice of the simulation framework and the choice of the paradigm for modeling the EOS.

3.3.1. *Transport codes for the Beam Energy Scan physics*

While there are many microscopic transport codes available,³¹⁹ relatively few of them are suited for use either as an afterburner (see Sec. 2.4) or as an independent simulation framework for the range of energies explored in the RHIC BES program.

Since the early days of RHIC, the Ultrarelativistic Quantum Molecular Dynamics (UrQMD) transport model^{36,37} has been widely used both as an independent simulation framework and, later on, as a hadronic afterburner. Suitably for attempts to describe collisions from the intermediate to ultrarelativistic energies, the model incorporates mean-field interactions, includes scattering, production, and decay processes for over 80 hadronic species, and describes string excitation and fragmentation for collisions at energies exceeding $\sqrt{s_{\text{NN}}} = 5$ GeV. The code has been developed over the years, with improvements such as using PYTHIA,⁴⁰⁶ which employs the Lund string fragmentation model^{407,408} for multiparticle production, for initial hard scatterings⁴⁰⁹ or incorporating an intermediate hydrodynamic stage, based on the ideal 3+1D relativistic hydrodynamics simulation code SHASTA (SHarp And Smooth Transport Algorithm),^{410,411} for an intermediate fluid dynamic description of the hot and dense phase,¹⁵ thus making UrQMD a self-contained hybrid approach.

Another framework suited for the RHIC era is the Parton-Hadron-String-Dynamics (PHSD) code,^{405,412–414} which is a covariant approach, based on generalized off-shell transport equations for test particles,^{415,416} that can describe both hadronic and partonic matter. Given that PHSD propagates Green's functions which, in particular, include information about the spectral functions of the described degrees of freedom, it is an extension beyond the usual semi-classical BUU-type models. The hadronic degrees of freedom include the baryon octet and decuplet, the 0^- and 1^- meson nonets, and certain higher resonances. At low energies, hadronic reactions are performed using the corresponding cross sections, while at high energies multi-particle production is achieved by using event generators FRITIOF^{417,418} and PYTHIA.⁴⁰⁶ At high energies, partonic dynamics is realized by using the Dynamical Quasiparticle Model (DQPM),⁴⁰⁵ fit to describe lattice QCD data.⁴¹⁴ As a result, PHSD can be used to describe the entire evolution of a relativistic heavy-ion collision, including

the initial hard scatterings and string formation, transition to the dynamically evolving quark-gluon plasma (QGP), hadronization, and subsequent hadronic phase. Recently, an offshoot of the code called Parton-Hadron-Quantum-Molecular-Dynamics (PHQMD)³⁸ has been developed which uses a QMD approach to propagating hadrons and thus includes n -body dynamical evolution.

The Jet AA Microscopic (JAM) transport model³⁰ has likewise been designed to be used across a large range of energies. At low energies, the degrees of freedom of the model include hadrons and their excited states, and the nuclear mean field with momentum dependence can be included.⁴¹⁹ String excitation is implemented according to the Heavy Ion Jet Interaction Generator (HIJING) model,^{420–422} which also serves as a template for implementation of multiple mini-jet production, for which the jet cross sections and the number of jets are calculated using an eikonal formalism for perturbative QCD. Hard parton-parton scatterings are simulated using PYTHIA.⁴²³

Another framework including both partonic and hadronic degrees of freedom is A Multi-Phase Transport (AMPT) model.³⁴ The initial state of the evolution is obtained using HIJING and includes spatial and momentum distributions of minijet partons and soft string excitations. The evolution of partons is achieved by using Zhang's Parton Cascade (ZPC),⁴²⁴ while conversion of partons into hadrons is modeled either by the Lund string fragmentation model^{407,408,423} or string melting with quark coalescence.^{425–427} Further evolution of hadrons is described by A Relativistic Transport (ART) model^{428,429} extended to include additional reaction channels of relevance for modeling high energy collisions, such as formation of antibaryon resonances, baryon-antibaryon production from mesons, and baryon-antibaryon annihilation. In subsequent developments, the model has been extended by both partonic⁴³⁰ and hadronic⁴³¹ mean fields.

A relatively recent addition is the SMASH (Simulating Many Accelerated Strongly-Interacting Hadrons) hadronic transport code.³⁵ Building on the experience of other transport approaches to date, including UrQMD, GiBUU,⁴³² and pBUU,^{337,349} SMASH is a modern (utilizing C++ and ROOT, among others), modular, open source and version-controlled code developed both to be used as an afterburner and as a stand-alone simulation framework for collisions at low energies. The framework includes all hadrons and confirmed hadronic resonances with masses up to ≈ 2 GeV (over 120 hadronic species, where isospin states such as π^\pm and π^0 or baryons and antibaryons are counted as one species). It also takes advantage of new exper-

imental data for cross sections and resonance properties (with all hadronic reactions fulfilling the principle of detailed balance), includes a perturbative treatment of photon and dilepton emission,^{433,434} and deuteron production via explicit reactions.^{349,352} Notably, SMASH often implements multiple phenomenological and algorithmic solutions (such as different collision criteria or various forms of mean-field potentials) that can be freely chosen by the user and which allow for extensive tests of given simulation inputs within the same framework. Similarly to the hybrid UrQMD code, there also exists a modular hybrid approach SMASH-vHLE-hybrid,⁸⁸ coupling 3+1D viscous hydrodynamics vHLE (viscous Harten-Lax-van Leer-Einfeldt algorithm)¹³⁹ to SMASH. A further improvement in the form of dynamical (gradual) initialization of the hydrodynamic phase in the SMASH-vHLE-hybrid is currently under development.^{435,436}

3.3.2. Modeling the equation of state

For both BUU- and QMD-type simulations, the EOS enters the evolution of the system primarily through single-particle equations of motion, Eqs. (50–51) or Eqs. (56–57), where it contributes to changes in particles' momenta through gradients of the single-particle energy. In the case of models including relativistic scalar-type interactions, the EOS also explicitly affects the propagation of particles through its effects on the particle effective mass. Additionally, the EOS can play a role in the scattering term, leading to, e.g., subthreshold production or reduced in-medium cross sections (note, however, that most in-medium cross section parametrizations currently in use are purely phenomenological with no explicit connection to the local potential).

Historically, development of transport simulations was driven by early experiments on relativistic heavy-ion collisions at incident kinetic energies per nucleon (excluding the nucleon mass) from a couple hundred of MeV/nucleon up to about $E_{\text{kin}} \approx 1$ GeV/nucleon ($\sqrt{s_{\text{NN}}} \approx 2.3$ GeV). These experiments probed densities from around that of normal nuclear matter n_0 up to at most 3 times n_0 ,²²² and consequently it was natural that simulations utilized EOSs known to correctly describe the established properties of nuclear matter in the ground state, such as saturation at $n_0 \approx 0.17 \pm 0.03 \text{ fm}^{-3}$ and binding energy of nuclear matter $B_0 \approx -16$ MeV.⁴³⁷ The single-particle potentials reproducing these properties can be cast in a particularly simple form often referred to as the Skyrme potential, in which they are parametrized as a function of local

baryon density n_B ,

$$U(n_B) = A \left(\frac{n_B}{n_0} \right) + B \left(\frac{n_B}{n_0} \right)^\tau . \quad (60)$$

Here, A , B , and τ are free parameters which are fit so that the EOS reproduces the values of n_0 , B_0 , and the incompressibility of nuclear matter at saturation K_0 . With values of n_0 and B_0 relatively well known, the Skyrme EOSs differ between each other mostly by the value of K_0 , the constraint on which is less stringent, $K_0 = 230 \pm 30$ MeV.⁴³⁷ In turn, variation in K_0 allows for variation between the EOSs at densities away from n_0 .

Importantly, to maximize the range of possible behaviors of the EOS at high densities, K_0 is often varied well beyond the experimentally constrained region above, $K_0 \in [170, 380]$ MeV. In such cases, one should understand the used values of K_0 not as an assertion on the actual value of incompressibility at n_0 , but rather as a parameter which specifies the behavior of the EOS for the range of densities relevant to a given study. As an example, in the case of collisions at energies which primarily probe the EOS at densities above $2n_0$, any conclusions on the value of K_0 which describes the data best only concerns the behavior of the EOS above $2n_0$, and is by no means a statement on the behavior of the EOS around n_0 .

Note that the parametrization in terms of baryon density implies interactions of vector type, however, the potential shown in Eq. (60) is non-relativistic. While one can always assume that $U(n_B)$ is simply the form of the potential in the local rest frame and boost the resulting equations of motion to account for relativistic effects (such as, e.g., contributions to the equations of motion from a non-zero baryon current), this needs to be done with care so that all relevant relativistic terms are recovered.³⁹⁶ Regardless of whether the modification of the equations of motion due to the potential is treated relativistically or not, the form of the potential shown in Eq. (60) leads to a superluminal behavior at high densities for any $\tau \geq 1$,⁴³⁸ which is ubiquitous among Skyrme-type models.⁴³⁷ To prevent such superluminal behavior, some codes³²⁹ employ a more stable form

$$U(n_B) = \frac{A \left(\frac{n_B}{n_0} \right) + B \left(\frac{n_B}{n_0} \right)^\tau}{1 + \alpha \left(\frac{n_B}{n_0} \right)^{\tau-1}} , \quad (61)$$

where α is a dimensionless parameter.

In addition to a density-dependent Skyrme parametrization, many codes also employ momentum-dependent terms in the potential.^{335,439,440} This

is motivated both by fits to experimental data^{441,442} as well as model calculations,⁴⁴³ showing that while a nucleon interacting with nuclear matter around n_0 feels attraction if it moves slowly, it feels repulsion once its kinetic energy exceeds ≈ 200 MeV. Implementations of the momentum-dependence of the potential, in general, are of the following form,

$$U_p(n_B, \mathbf{p}) = C \int \frac{d^3 p'}{(2\pi)^3} \frac{f_{\mathbf{r}, \mathbf{p}'}}{1 + \left[\frac{\mathbf{p} - \mathbf{p}'}{\Lambda} \right]^2}, \quad (62)$$

with the free parameters C and Λ fit to reproduce, e.g., the expected value of the effective mass at the Fermi surface⁴³⁹ or the measured values of U_p at chosen nucleon momenta.⁴⁴⁰ Notably, to ease the significant numerical cost associated with the calculation of momentum-dependent potentials in simulations (which for each particle requires summing the contributions from all other particles), many approaches use approximated expressions for U_p , with sometimes non-trivial consequences for the behavior of the potential.⁴⁴⁰ Alternatively to the form shown in Eq. (62), momentum dependence can be also included by employing scalar interactions, which lead to equations of motion including terms dependent on gradients of the local values of the effective mass; this can be achieved, among others, by using relativistic mean-field potentials, such as those based on the Walecka model.³⁹⁷ A fully relativistic generalization of Eq. (62) has been developed in Ref.,⁴⁴⁴ however, due to formidable complexity its use in realistic simulations has not been pursued.

We note that while the Skyrme potential, Eq. (60), depends only on density, models using this potential can still exhibit non-trivial effects due to temperature. This is because the behavior of a given system depends not only on the interactions between the particles, but also on the momenta of the particles. In equilibrium, these momenta can often be described by an appropriate distribution with an explicit dependence on temperature: the Fermi or Bose distribution for temperatures where quantum statistics plays a role, or the Boltzmann distribution for higher temperatures. Consequently, even though the interaction terms governing the system do not depend on temperature, effects due to temperature are reflected in the kinetic part of the single-particle energies which in turn affect the evolution through single-particle equations of motion, Eqs. (50) and (51) or (56) and (57).

To illustrate this fact, one can consider the Skyrme potential as used to describe ordinary nuclear matter, in which case the nucleon pressure is the sum of the Fermi pressure and interaction pressure arising from the

interaction term, Eq. (60). As already mentioned, for the model to describe nuclear matter one adjusts the interaction parameters to reproduce the well-established properties at $T = 0$: saturation density n_0 , binding energy B_0 , and incompressibility K_0 . Note that satisfying these properties means that at $T = 0$ and $n_B = n_0$, $P = 0$ (because matter is in equilibrium) and $dP/dn_B > 0$ (because incompressibility is positive). We also naturally have $P(T = 0, n_B = 0) = 0$ and, since the Fermi pressure is always positive and for very small densities the interaction terms are negligibly small, $P > 0$ at small densities. Together, this means that at $T = 0$ there is a region between $n_B = 0$ and $n_B = n_0$ where $P < 0$ and, consequently, there is also a region where $dP/dn_B < 0$, that is a region where the matter is mechanically unstable. In other words, we are dealing with a system in which at $T = 0$ there is a first-order phase transition between two phases characterized by different densities. Note that the occurrence of regions with $P < 0$ and $dP/dn_B < 0$ is an effect driven by the interaction pressure, as the Fermi pressure is always positive. In this model, changing the temperature affects only the kinetic (Fermi) contribution to the pressure; nevertheless, this is enough to yield further non-trivial features. As the temperature is increased, particles occupy higher momentum states and so the kinetic contribution to the pressure becomes larger. Gradually, the kinetic contribution starts to dominate the interaction pressure so that, for high enough temperatures, there isn't any region where $dP/dn_B < 0$, i.e., there is no density at which the system is unstable and, consequently, there is only one possible phase of the system. The temperature at which this happens is the critical temperature; as the critical temperature is approached from below, the density interval for which $dP/dn_B < 0$ collapses to a point, at the critical density, where $dP/dn_B = 0$. Thus, even though the interaction terms used in the model depend only on density and are fixed to reproduce the properties of nuclear matter at $T = 0$, the system exhibits non-trivial behavior with changing temperature, including the existence of a critical point.

We stress that while the above simple example is considered using thermodynamic variables such as temperature or pressure, the arguments used can be easily generalized to systems out-of-equilibrium, and in particular to heavy-ion collision evolution as described by microscopic transport. Since the evolution involves both particle velocities and gradients of mean-field interactions (where the former, in equilibrium, can be directly connected to temperature), transport simulations can exactly reproduce the thermodynamic behavior of the underlying EOS even though there are no explicit

temperature-dependent terms in the single-particle energies. Here, the influence of the particle momenta leads to non-trivial effects and different outcomes in situations characterized by different momentum distributions, e.g., at varying collision energies or at different stages of collisions at a given energy which, if equilibrium could be achieved, would correspond to different temperatures. This effective temperature dependence is even more pronounced in case of interactions with momentum dependence such as, e.g., the interaction in Eq. (62) or scalar interactions; in particular, scalar interactions can also lead to more complex structures in the phase diagram. At the same time, even though such an effective temperature dependence leads to non-trivial features, one can always wonder whether it is sufficient to capture all relevant effects; this remains to be seen.

The primary drawback of the Skyrme and momentum dependent potentials described above is that they only allow for modest variations in the interactions. This is naturally appropriate for describing experiments probing densities not too far from n_0 , where the properties of nuclear matter are reasonably constrained. However, at higher densities and very high momenta there is no reason to expect the single-particle potentials to exhibit the same functional form which is found suitable to describe nuclear matter close to its ground state. Additionally, since higher densities are reached in collisions at higher energies, it becomes necessary to use potentials which are relativistically covariant. Consequently, describing experiments at $E_{\text{kin}} \gtrsim 1$ GeV ($\sqrt{s_{\text{NN}}} \gtrsim 2.3$ GeV) calls for employing relativistic single-particle potentials which not only describe the known properties of ordinary nuclear matter, but also allow for the possibility of substantial changes to the behavior of the potential at high densities, momenta, and/or temperatures.

Addressing this need has been the focus of a number of recent efforts. Relativistically covariant single-particle potentials based on an arbitrary number of vector-type interaction terms, referred to as the vector density functional (VDF) model, have been developed³⁹⁵ with the goal of describing both the known properties of ordinary nuclear matter and its possible non-trivial behavior at high baryon densities. Starting from the relativistic Landau Fermi-liquid theory,⁴⁴⁵ that work develops easily parametrizable, relativistically covariant, and thermodynamically consistent EOS which leads to single-particle energies of the form

$$\varepsilon_{\mathbf{p}} = \sqrt{m^2 + \mathbf{\Pi}^2} + \sum_{k=1}^K A_k^0 . \quad (63)$$

Here, m is the particle mass, $\mathbf{\Pi} \equiv \mathbf{p} - \sum_{k=1}^K \mathbf{A}_k$ is the kinetic momentum, and the vector field A_k^λ is defined as

$$A_k^\lambda(x) = C_k n_B^{b_k-2} j_B^\lambda, \quad (64)$$

where the baryon current j_B^μ is given by a self-consistent relation,

$$j_B^\mu \equiv g \int \frac{d^3p}{(2\pi)^3} \frac{p^\mu - \sum_{k=1}^K A_k^\mu}{\sqrt{m^2 + \mathbf{\Pi}^2}} f_{\mathbf{p}}, \quad (65)$$

with g denoting the degeneracy and $f_{\mathbf{p}}$ the distribution function, and $n_B \equiv \sqrt{j_{B,\mu} j_B^\mu}$ is the rest-frame baryon density. Assuming thermal equilibrium, this leads to a pressure functional of the form

$$P_K = g \int \frac{d^3p}{(2\pi)^3} T \ln \left[1 + e^{-\beta(\varepsilon_{\mathbf{p}} - \mu_B)} \right] + \sum_{k=1}^K C_k \left(\frac{b_k - 1}{b_k} \right) n_B^{b_k}, \quad (66)$$

where T is the temperature, $\beta = 1/T$, and μ_B is the baryon chemical potential, so that the first term can be easily recognized as the pressure of the ideal relativistic Fermi gas. This relativistic generalization of the Skyrme potential, through the inclusion of an arbitrary number of potential terms, allows one to consider various possible behaviors of the potential at high baryon densities while retaining the ability to describe the known properties of ordinary nuclear matter around saturation. Of note is also the fact that while the form of the potential leading to Eq. (66) is relatively simple, polynomials of vector density are the *only* possible form of the interactions if one considers a mean-field model with self-consistently defined baryon current and one demands that the coefficients of the interaction terms are constant³⁹⁶ (the same can be shown to be true for scalar-type interactions³⁹⁶).

In the original work,³⁹⁵ the developed formalism has been used to model various critical densities, critical temperatures, and coexistence widths of a possible first-order phase transition at baryon densities $n_B > 2n_0$. As shown in Fig. 16, this leads to a non-trivial dependence of the pressure as a function of baryon density which would be impossible to describe with the standard Skyrme form of the interaction. One should note that while in this example the VDF model has been employed in a minimal form (utilizing $K = 4$ interaction terms) allowing one to describe nuclear matter with a first-order phase transition at high densities, the model can be fit to describe other possible behaviors of the single-particle energy or, equivalently, pressure. In particular, additional terms can be added to prevent the superluminal behavior of the speed of sound³⁹⁵ at densities above the postulated locations of phase transitions.

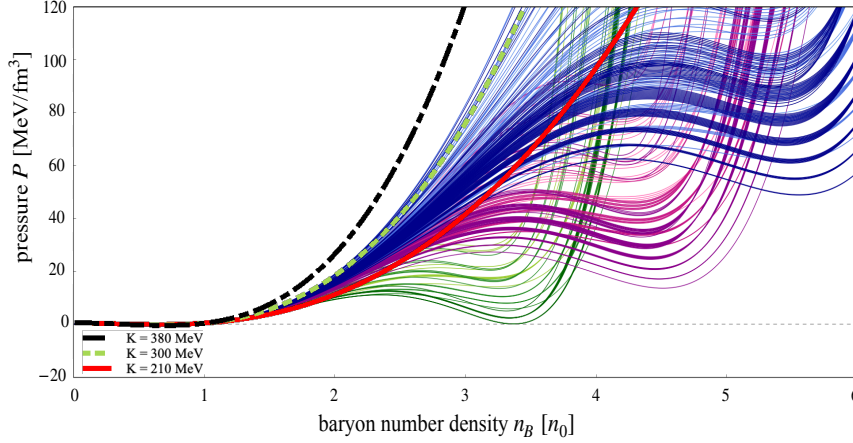


Fig. 16.: Pressure at $T = 0$ as a function of baryon density for 3 EOSs using the Skyrme parametrization and 9 families of VDF EOSs.³⁹⁵ The Skyrme EOSs are marked with thick solid red, short-dashed green, and mixed-dashed black lines, corresponding to incompressibility at saturation of $K_0 = 210$ (soft), 300 (medium), and 380 MeV (hard), respectively. Thin green, magenta, and blue curves mark VDF EOSs with a high-density phase transition characterized by a critical density of $n_c^{(Q)} = 3.0n_0, 4.0n_0,$ and $5.0n_0,$ respectively, with light, medium dark, and dark variations in the colors of the curves further differentiating between curves with the critical temperature $T_c^{(Q)} = 50, 100,$ and 150 MeV. Within each family, the VDF EOSs further vary with respect to the width of the coexistence region at $T = 0$. All of the VDF EOSs describe nuclear matter with $n_0 = 0.160 \text{ fm}^{-3}$, $B_0 = -16 \text{ MeV}$, and the critical point of the nuclear liquid-gas phase transition at $n_c^{(N)} = 0.06 \text{ fm}^{-3}$ and $T_c^{(N)} = 18 \text{ MeV}$, with incompressibilities averaging at $\langle K_0 \rangle = 273.1 \pm 5.1 \text{ MeV}$. It is easily seen that parametrizations of the VDF EOS can lead to a great variability in the behavior of the EOS at high densities. Figure modified from Ref.³⁹⁶

The above-described model has been subsequently generalized to enable parametrization of the single-particle potential based on a chosen dependence of the speed of sound squared at zero temperature c_s^2 on baryon density.²⁴³ Within this approach, the rest-frame single-particle potential, $U(n_B) \equiv A^0(n_B)|_{\text{rest frame}}$, is given by

$$U(n_B) = \mu_B(n_B^{(0)}) \exp \left[\int_{n_B^{(0)}}^{n_B} dn' \frac{c_s^2(n')}{n'} \right] - \mu^*(n_B), \quad (67)$$

where $n_B^{(0)}$ is an arbitrarily chosen density at which the corresponding value of the chemical potential $\mu_B(n_B^{(0)})$ is known and $\mu^*(n_B) \equiv [m^2 +$

$(6\pi^2 n_B/g)^{2/3}]^{1/2}$. A convenient way of parametrizing such a potential, leading to an analytic expression for $U(n_B)$ (and, consequently, $A^\mu(n_B)$), is to consider a piecewise functional form of $c_s^2(n_B, T=0)$ in which the speed of sound squared follows the Skyrme-like parametrization up to some density n_1 , after which it assumes a constant value in chosen density intervals,²⁴³

$$c_s^2(n_B) = \begin{cases} c_s^2(\text{Skyrme}) & n_B < n_1 \\ c_1^2 & n_1 < n_B < n_2 \\ c_2^2 & n_2 < n_B < n_3 \\ \dots & \\ c_m^2 & n_m < n_B \end{cases} \quad (68)$$

where n_1, \dots, n_m are chosen values of baryon density, which yields

$$U(n_B) = \begin{cases} U_{\text{Sk}}(n_B) & n_B < n_1 \\ C(n_1) \left(\frac{n_B}{n_1}\right)^{c_1^2} - \mu^*(n_B) & n_1 < n_B < n_2 \\ \dots & \\ C(n_1) \left(\frac{n_B}{n_k}\right)^{c_k^2} \prod_{i=2}^k \left(\frac{n_i}{n_{i-1}}\right)^{c_{i-1}^2} - \mu^*(n_B) & n_k < n_B < n_{k+1} \end{cases} \quad (69)$$

where $U_{\text{Sk}}(n_B)$ is a Skyrme-like potential and $C(n_1) = U_{\text{Sk}}(n_1) + \mu^*(n_1)$ (here, ‘‘Skyrme-like potential’’ refers to a relativistic VDF potential with $K = 2$ interaction terms parametrized to reproduce chosen values of n_0 , B_0 , and K_0). Note that Eq. (69) makes it evident that this generalization of the VDF potential, straying away from the polynomial form of the EOS, indeed leads to density-dependent coefficients of the interaction terms, $\tilde{C}_k \equiv C(n_1) \prod_{i=2}^k \left(\frac{n_i}{n_{i-1}}\right)^{c_{i-1}^2}$.

Examples of functional dependence of c_s^2 on baryon density and the corresponding single-particle potentials $U(n_B)$ are shown in Fig. 17. As in the case of the original VDF model, the c_s^2 -parametrization supports non-trivial behavior of the EOS or, equivalently, the single-particle potential at high baryon densities. Moreover, in contrast to the original VDF model where the EOS essentially takes the form of a polynomial, the c_s^2 -parametrization allows one to vary the behavior of the EOS within the chosen density intervals in an entirely independent way.

The c_s^2 -parametrization is not only highly intuitive due to its anchoring in the baryon-density dependence of the speed of sound (which additionally allows one to easily avoid superluminal behavior at any density), but also

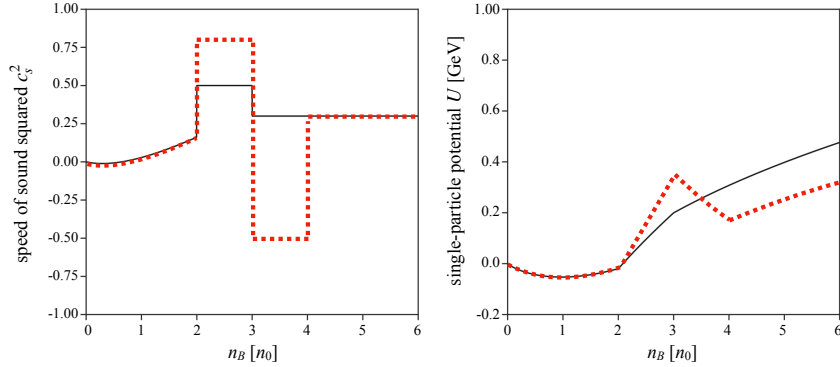


Fig. 17.: Functional dependence of c_s^2 on baryon density for two chosen c_s^2 profiles (left) and the corresponding rest-frame single-particle potential $U(n_B)$ (right) obtained within the c_s^2 -parametrization of the generalized VDF model.²⁴³

provides a convenient starting point for performing comprehensive analyses of the corresponding EOSs through simple varying of the parameter sets $\{c_i^2, n_i\}$. In particular, one can test the sensitivity of flow observables differentially in chosen density regions²⁴³ as shown in Fig. 18. It is evident that changing the EOS for densities $n_B \in (2, 3)n_0$ leads to most prominent changes in the proton and pion flow observables within a large range of energies, $\sqrt{s_{\text{NN}}} \approx 2\text{--}8$ GeV ($E_{\text{kin}} \approx 1\text{--}32$ GeV/nucleon). Changing the EOS for densities $n_B \in (3, 4)n_0$ leads to significantly smaller effects, largely constrained to $\sqrt{s_{\text{NN}}} \approx 3\text{--}8$ GeV ($E_{\text{kin}} \approx 3\text{--}32$ GeV/nucleon), and changes in the density interval $n_B \in (4, 5)n_0$ (and, consequently, likely also for higher densities) lead to only very subtle effects for $\sqrt{s_{\text{NN}}} \approx 4\text{--}8$ GeV ($E_{\text{kin}} \approx 8\text{--}32$ GeV/nucleon). This suggests that the possibilities to constrain the EOS at densities $n_B > 4n_0$ using heavy-ion collisions may be limited, although some sensitivity seems to remain in the deuteron flow (note that the values of the deuteron flow in the figure are divided by 2).

Furthermore, since one can define, without any significant numerical penalty, arbitrarily many intervals characterized by a constant c_s^2 and thus, in the limit of an infinite number of intervals, the parametrization can exactly reproduce any $c_s^2(n_B, T = 0)$ profile, the approach can be used to explore the consequences of *any* chosen EOS for microscopic transport simulations of heavy-ion collisions as long as the dependence $c_s^2(n_B, T = 0)$ is available.³⁸⁴ Here, however, some caution is warranted: since the approach is based on vector-type interactions, the resulting mean-field potentials do

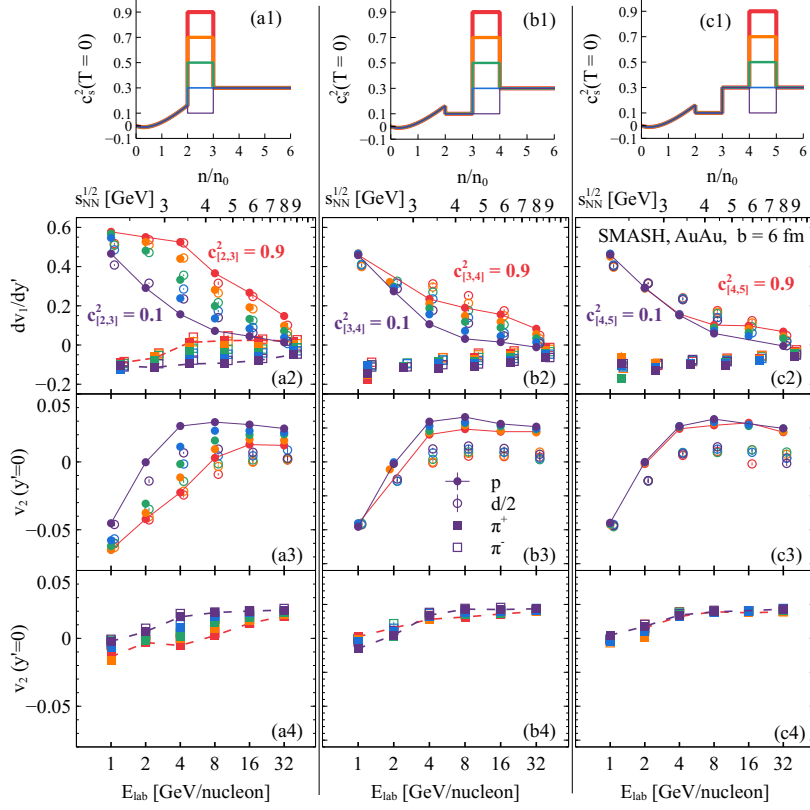


Fig. 18.: Results of simulations in SMASH using different c_s^2 -parametrizations of the EOS. For $n_B < 2n_0$, the EOS takes a Skyrme-like form. In columns (a), (b), and (c), the EOS is only varied in the density interval $n_B \in (2, 3)n_0$, $n_B \in (3, 4)n_0$, and $n_B \in (4, 5)n_0$, respectively; for densities $n_B > 2n_0$ outside of the varied intervals, c_s^2 takes on an arbitrary constant value. The first row shows variations in c_s^2 in the above intervals, where it takes representative values of $\{0.1, 0.3, 0.5, 0.7, 0.9\}$ marked with varying colors. These then correspond to results for dv_1/dy' (row 2) and v_2 (rows 3 and 4) at midrapidity for protons (full circles), deuterons (empty circles), and positive (filled squares) and negative (empty squares) pions; here, the deuteron flow is divided by 2, and the points for deuterons and pions are slightly shifted to the right for clarity. Figure from Ref. ²⁴³

not exhibit any complex temperature dependence (more precisely, the temperature dependence of the EOS comes solely from ideal gas terms). Since collisions of heavy ions probe temperatures from a few tens to well over a hundred of MeV, this may lead to substantial deviations from the EOS

which was used to provide the input $c_s^2(n_B, T = 0)$ profile if that EOS has a non-trivial (beyond ideal gas) dependence on temperature.

The two above-discussed parametrizations have been developed with relativistic BUU-type transport in mind and implemented in the transport code **SMASH** (currently, only the original VDF model is available in the public version of the **SMASH** code). Recently, an implementation of the single-particle potentials allowing one to go beyond the default Skyrme potential, Eq. (60), has been employed in **UrQMD**.²⁴¹ The approach is based on the fact that the density-dependent average potential energy per particle, $\mathcal{V}(n_B)$, can be related to the density-dependent single-particle potential $U(n_B)$ through

$$U(n_B) = \frac{\partial(n_B \mathcal{V}(n_B))}{\partial n_B}, \quad (70)$$

so that $U_i = U(n_B(\mathbf{X}_i))$. While the above prescription may appear trivial in the case of Skyrme-like models (for which the single-particle potential is equivalent to the mean-field potential required for the equations of motion), it allows one to extend the treatment of potentials in QMD to more complicated models, including models with varied interactions between multiple species, relativistic fields, and momentum-dependence (or, equivalently, effective masses), as long as the average potential per particle $\mathcal{V}(n_B)$ can be identified by some means. In particular, this can be achieved by generating a table of the average potential values at a given n_B , which is the basis of the implementation of the approach in **UrQMD**,²⁴¹ allowing for studying the influence of almost any EOS on heavy-ion collision observables. (We note here, however, that similar caution has to be exercised here as in the case of c_s^2 -parametrized potentials described above, since the approach can capture only the density dependence of a given potential, provided at $T = 0$, and any temperature-dependent effects come solely from ideal-gas-like contributions, which may lead to deviations in the behavior of the finite-temperature EOS in the underlying model and in the simulations).

In the initial exploration,²⁴¹ this approach has been used to test the effects of multiple EOSs, including in particular EOSs based on the Chiral Mean Field (CMF) model^{446–448} (see the left panel in Fig. 19), which uses an extensive list of degrees of freedom (including a complete list of all known hadrons as well as three light quark flavors and a gluon contribution) and describes the liquid-gas phase transition in ordinary nuclear matter, a transition between quarks and hadronic degrees of freedom, and chiral symmetry restoration introduced through parity doubling in the mean-field

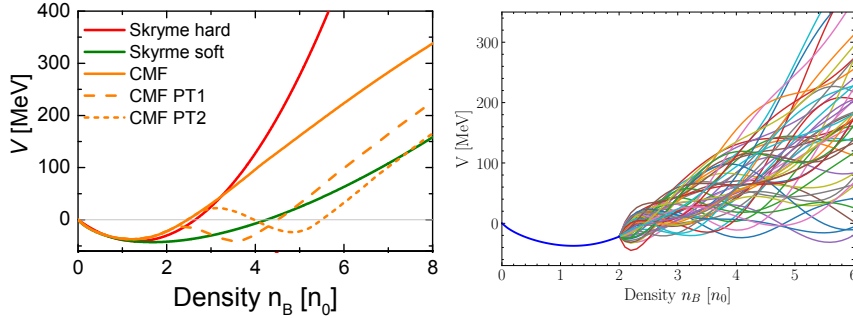


Fig. 19.: Average potential per particle as a function of baryon number density for an original CMF EOS and 2 CMF EOSs with an additional strong phase transition at high densities (*left*)²⁴¹ as well as for numerous combinations of the CMF model with a flexible polynomial parametrization of the EOS at high densities (*right*).²⁴⁴

approximation.⁴⁴⁹ In a subsequent work,²⁴⁴ the same framework has been used to explore effects of variations in the EOS above $n_B = 2n_0$ by joining a CMF EOS, describing nuclear matter for $n_B < 2n_0$, with a seventh-degree-polynomial parametrization of the potential energy per baryon \mathcal{V} at $n_B > 2n_0$,

$$\mathcal{V}(n_B) = \sum_{i=1}^7 \theta_i \left(\frac{n_B}{n_0} - 1 \right)^i + C, \quad (71)$$

where θ_i are independently varied parameters and C is a constant ensuring continuity at $n_B = 2n_0$ (see the right panel in Fig. 19).

The above recent developments in modeling the EOS address only its density dependence, while heavy-ion collisions probe dense nuclear matter not only at various densities, but also at varying temperatures and isospin fractions. Moreover, as already mentioned above, the nuclear interaction also depends on momentum (or, equivalently, effective mass). Comprehensive studies of the EOS through comparisons of simulations with experimental data require development and implementation of potentials able to capture effects due to all of these factors.

The momentum-dependence of the EOS, which is expected to have a large effect on extractions of the EOS at all BES energies, can be conveniently modeled by including scalar-type interactions, which in the mean-field approximation lead to the dependence of the EOS on scalar density. In the past, this has been mostly done by using relativistic mean-field models, such as the Walecka model,³⁹⁷ which, however, do not allow flexible

parametrizations of the EOS. A more flexible approach, based on the relativistic Landau Fermi-liquid theory, has been proposed in the past.⁴⁵⁰ More recently, following similar ideas, a generalization of the VDF model, based on a vector-scalar density functional (VSDF), has been developed³⁹⁶ to enable maximally flexible parametrizations of the scalar-density-dependence of the EOS, and its implementation in transport simulations is the subject of an ongoing work. Notably, scalar-type interactions additionally provide a non-trivial (i.e., beyond a thermal contribution of the ideal gas form) temperature dependence.

The isospin-dependence of the EOS, often quantified in terms of the symmetry energy defined as the isospin-dependent contribution to energy per particle, is expected to be less important for regions of the phase diagram explored in BES. It is, however, crucial for experiments colliding unstable isotopes, such as those planned at FRIB.^{222,315,451} Moreover, the symmetry energy is a key component of the EOS connecting nearly-symmetric nuclear matter found on Earth and the highly asymmetric nuclear matter relevant to studies of neutron stars, neutron star mergers, and supernovae^{222,452}. Finally, while the effects of the symmetry energy may be small for collision energies $\sqrt{s_{\text{NN}}} \gtrsim 3$ GeV ($E_{\text{kin}} \gtrsim 2.9$ GeV), they may still be measurable in the upcoming precision era for heavy-ion physics.⁴⁵³ Currently, the prevailing approach to modeling the dependence of the EOS on the isospin fraction is to express the isospin-dependence of the single-particle potential in terms of the expansion coefficients of the symmetry energy around n_0 ,⁴⁵⁴ which essentially gives it a Skyrme-like form. However, such simple phenomenological approaches may not correctly capture a number of important effects, including the very high-density behavior of the symmetry energy. Therefore, it is worthwhile to consider ways in which isospin dependence can be flexibly and efficiently modeled in transport simulations.

3.4. Constraints on the equation of state

Recent advances in the use of statistical methods as well as a greater availability of significant high-performance computing resources have brought about a qualitative change in using models of heavy-ion collisions to constrain the EOS. While in the past, due to limitations in computational power, comparisons of models with experimental data could only afford testing several different EOSs, nowadays it is possible to perform extensive Bayesian analyses based on simulations that explore tens or even hundreds

of different EOSs which then provide input to event emulators. In view of this, in the following we will largely concentrate on most recent results which take advantage of these new capabilities.

3.4.1. Bayesian analysis of BES FXT proton directed and elliptic flow data

Recent work²⁴³ performed a Bayesian analysis of proton collective flow data from fixed-target collisions at beam energies $\sqrt{s_{NN}} = \{3.0, 4.5\}$ GeV ($E_{\text{kin}} = \{2.9, 8.9\}$ GeV/nucleon) as measured by the STAR experiment.^{379,455} Specifically, the analysis considered the slope of the p_T -integrated proton directed flow dv_1/dy and the p_T -integrated proton elliptic flow v_2 , both taken at midrapidity. Employing a large family of significantly varying EOSs was made possible by using a flexible piecewise parametrization of the EOS,²⁴³ described in Sec. 3.3.2. The family of EOSs was generated by varying independently three EOS parameters: the incompressibility at saturation K_0 , the value of the speed of sound squared c_s^2 between 2 and 3 saturation densities $c_s^2[2, 3]n_0$, and the value of c_s^2 between 3 and 4 saturation densities $c_s^2[3, 4]n_0$; c_s^2 above $4n_0$ was taken to be equal $c_s^2[n_B > 4n_0] = 0.3$ for all EOSs (an example of the effects of varying $c_s^2[2, 3]n_0$ and $c_s^2[3, 4]n_0$ is shown in Fig. 17).

The Bayesian analysis of simulations using the generated family of EOSs and experimental data yielded the following maximum *a posteriori* probability (MAP) parameters: $K_0 = 285 \pm 67$ MeV, $c_s^2[2, 3]n_0 = 0.49 \pm 0.13$, $c_s^2[3, 4]n_0 = -0.03 \pm 0.15$. Plots of posterior parameter distributions are shown in the left panel of Fig. 20, while a scatter plot of pressure at zero temperature against baryon density, obtained from sampling the EOS parameters from the posterior distribution, is shown in the right panel. For the first time, the obtained constraint on the EOS describes both the directed and elliptic proton flow data simultaneously,²⁴³ a characteristic which was not achieved in the case of the previous state-of-the-art study and led to a comparatively broad constraint.³²⁹ It is possible, however, that this was not only a result of performing the analysis with a much more flexible EOS, but also a consequence of using new data, given that there appear to be some discrepancies²⁴³ between flow measurements^{456–459} performed by experiments at the Alternating Gradient Synchrotron (AGS) and measurements provided by the STAR experiment.

It is evident both from the values of the MAP parameters and from the resulting behavior of the pressure that the constrained EOS suggests a first-

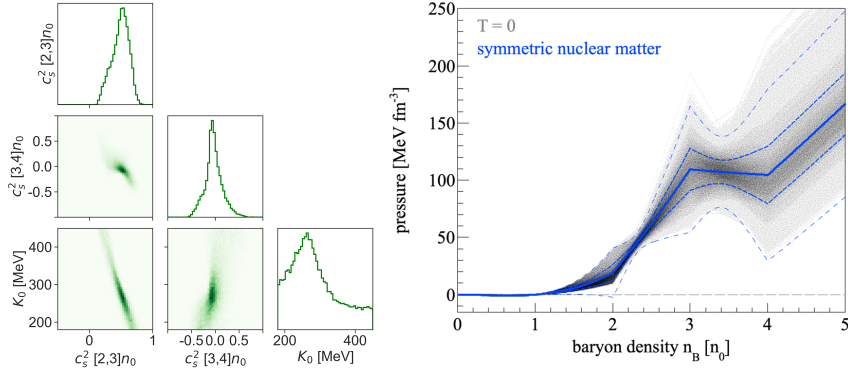


Fig. 20.: Results from a Bayesian analysis²⁴³ of STAR experiment proton flow data at $\sqrt{s_{\text{NN}}} = \{3.0, 4.5\}$ GeV.^{379,455} *Left:* Posterior parameter distribution for incompressibility at saturation K_0 , the value of the speed of sound squared between 2 and 3 saturation densities $c_s^2[2,3]n_0$, and the value of the speed of sound squared between 3 and 4 saturation densities $c_s^2[3,4]n_0$ obtained using STAR proton flow measurements. The maximum *a posteriori* probability (MAP) parameters are $K_0 = 285 \pm 67$ MeV, $c_s^2[2,3]n_0 = 0.49 \pm 0.13$, $c_s^2[3,4]n_0 = -0.03 \pm 0.15$. *Right:* Scatter plot of pressure at zero temperature as a function of baryon number density obtained by sampling the parameters of the EOS from the posterior distributions shown in the left panel. The solid line corresponds to the mean of the pressures, while the thick and thin dashed line correspond to the $\pm 1\sigma$ and $\pm 3\sigma$ contour around the mean, respectively. Figures from Ref.²⁴³

order phase transition for densities between 3 and 4 times the saturation density. However, some caution in interpreting the results is advised. As elaborated on in Sec. 3.3.2, momentum-dependence of nuclear interactions is a crucial part of modeling, which in particular for the energy range considered in the above study would result in an additional source of repulsion felt by nucleons interacting with a dense medium. In the absence of that (physically well-motivated) source of repulsion, describing the experimental data is possible by using an EOS which is relatively *stiffer*, that is characterized by higher values of the speed of sound. However, as can be seen from the correlation plot between $c_s^2[2,3]n_0$ and $c_s^2[3,4]n_0$ shown in the left panel of Fig. 20, a stiffer EOS at densities $n_B \in [2, 3]n_0$ prefers a softer EOS for densities $n_B \in [3, 4]n_0$. In other words, the significant softening of the EOS at high densities, preferred by the results of this Bayesian analysis, may not be a robust prediction given that the used model misses a crucial component of nuclear interactions which likely affects the extracted constraints

on the low- and medium-density EOS parameters. Since the momentum dependence itself likewise needs to be better constrained, especially at high densities, this discussion calls for an improved Bayesian analysis of available data where both the density- and the momentum-dependence of the nuclear EOS are varied.

3.4.2. Bayesian analysis of proton transverse kinetic energy and elliptic flow data

Another recent study²⁴⁴ performed a Bayesian analysis of proton mean transverse kinetic energy $\langle m_T \rangle - m_0$, based on data spanning collision energies $\sqrt{s_{\text{NN}}} \in [3.83, 8.86]$ GeV ($E_{\text{kin}} \in [5.9, 40.0]$ GeV/nucleon),^{460–462} and proton elliptic flow v_2 at midrapidity, based on data spanning collision energies $\sqrt{s_{\text{NN}}} \in [2.24, 4.72]$ GeV ($E_{\text{kin}} \in [0.8, 10.0]$ GeV/nucleon).^{379,455,456,463–466} This study used a flexible parametrization of the EOS, described in Sec. 3.3.2, in which a CMF EOS is used for densities below $2n_0$, while the potential energy per baryon at densities $n_B > 2n_0$ is given by a seventh-degree-polynomial with variable parameters. This led to a sizable family of EOSs with varying behavior at high densities, as shown explicitly in the right panel of Fig. 19.

Interestingly, the study explored the influence of either excluding or including constraints based on the mean transverse kinetic energy at the two lowest collision energies, $\sqrt{s_{\text{NN}}} = \{3.83, 4.29\}$ GeV ($E_{\text{kin}} = \{5.9, 7.9\}$ GeV/nucleon), resulting in two Bayesian analyses constrained by 13 or 15 experimental data points, respectively. This led to constraints on the potential energy per baryon \mathcal{V} with divergent behavior at large densities, $n_B \gtrsim 3n_0$, as can be seen in Fig. 21. This result is especially surprising given that sizable differences occur at high densities, that is in a region which should not be significantly affected by the excluded or included data points measured at energies which mostly probe densities $n_B \lesssim 3n_0$ (see Fig. 18).

The study then performs an extensive analysis of reasons behind this discrepancy, and suggests either a tension between the $\langle m_T \rangle - m_0$ and v_2 data or a shortcoming of the model used for simulations, including a possible need for an explicitly temperature-dependent EOS at higher beam energies where contributions from mesonic degrees of freedom may become dominant. (Additionally, as in the case of work described in the previous section, this study misses the momentum dependence of the nucleon potential which may lead to temperature-dependent effects.) Based on the

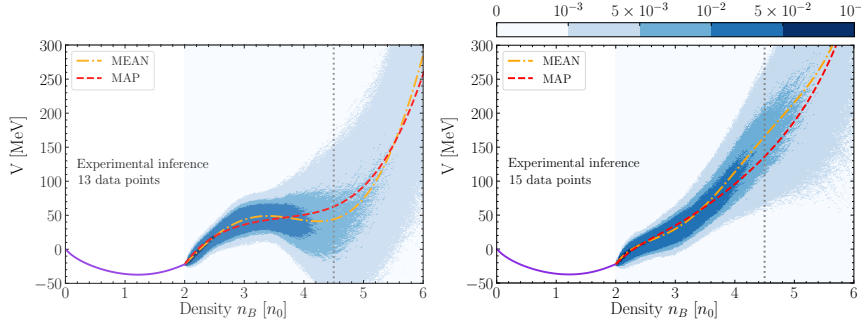


Fig. 21.: Posterior distributions for the average potential energy per baryon \mathcal{V} obtained from Bayesian analysis²⁴⁴ using experimental data for the proton elliptic flow v_2 and proton mean transverse kinetic energy $\langle m_T \rangle - m_0$. The purple line shows the CMF EOS, while the red dashed and orange dot-dashed lines show the EOS corresponding to maximum *a posteriori* parameters (MAP) and the mean EOS obtained by averaging the values of sampled potentials at different densities, respectively. The vertical gray line marks the highest average central density achieved in collisions at $\sqrt{s_{NN}} = 9$ GeV ($E_{\text{kin}} = 41$ GeV/nucleon). *Left*: Posterior obtained based on a data set of 13 experimental points excluding values of $\langle m_T \rangle - m_0$ for $\sqrt{s_{NN}} = \{3.83, 4.29\}$ GeV ($E_{\text{kin}} = \{5.9, 7.9\}$ GeV/nucleon). *Right*: Posterior obtained based on a data set of all 15 considered experimental points. Figures from Ref.²⁴⁴

study's closure tests with 13 and 15 data points, one can also surmise that the large discrepancy at high densities may be caused by a small deviation at lower densities (caused by the exclusion or inclusion of the two data points) which is then propagated to higher densities. This could be an artifact of constraining the EOS in a polynomial form, which is known for exhibiting uncontrolled behavior away from the region in which the polynomial is fit, and is further supported by the study's conclusion that the constraining power of the chosen data set at densities $n_B > 4n_0$ is weak (agreeing with the study of flow sensitivity to the EOS shown in Fig. 18). Finally, the study compares simulation results with experimental data for the slope of the directed flow dv_1/dy and finds a better agreement for the EOS obtained using 15 data points.

3.4.3. Prominent constraints from flow observables and discussion

The two recent Bayesian analysis studies described above used proton flow observables as the basis for their constraints on the dense nuclear matter EOS. Historically, flow was likewise often an observable of choice in endeav-

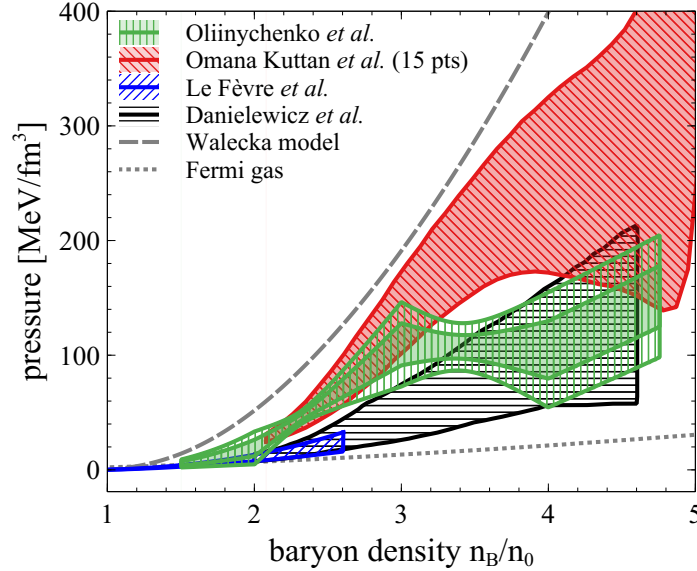


Fig. 22.: A compilation of selected constraints on the EOS based on comparisons of experimental data on flow observables with microscopic transport simulations carried out using pBUU (region with black horizontal stripes, labeled by “Danielewicz *et al.*”),³²⁹ IQMD (region with blue backward stripes, labeled by “Le Fèvre *et al.*”),³³⁰ SMASH (region with green vertical stripes, labeled by “Oliinychenko *et al.*”, where the shaded (unshaded) region corresponds to the 68% (95%) confidence interval),²⁴³ and UrQMD (region with red forward stripes, labeled with “Omana Kuttan *et al.* (15 pts)”, corresponding to the 68% confidence interval for the analysis using 15 input data points).²⁴⁴

ors aimed at constraining the EOS from heavy-ion collision data.

A compilation of well-known constraints on the EOS based on comparisons of experimental data on flow observables with microscopic transport simulations, including the recent studies, is shown in Fig. 22. A prominent constraint on the EOS for baryon densities between $(2-4.5)n_0$ was obtained³²⁹ by comparing measurements of collective flow from heavy-ion collisions^{457,467-469} at center-of-mass energies $\sqrt{s_{NN}} = 1.95-4.72$ GeV ($E_{kin} = 0.15-10$ GeV/nucleon) with results from pBUU^{337,349} hadronic transport simulations using Skyrme-type EOSs with different values of the incompressibility at saturation density K_0 (see Sec. 3.3.2). The study results indicate that the symmetric nuclear matter EOS lies between Skyrme-like EOSs characterized by $K_0 = 210$ MeV and $K_0 = 300$ MeV (see the region with black horizontal stripes, labeled by “Danielewicz *et*

al.). Subsequently, the elliptic flow data measured at $\sqrt{s_{\text{NN}}} = 2.07\text{--}2.52$ GeV ($E_{\text{kin}} = 0.4\text{--}1.5$ GeV/nucleon) by the FOPI collaboration⁴⁷⁰ were used together with simulations from Isospin Quantum Molecular Dynamics (IQMD)^{400,471} to constrain the incompressibility in a Skyrme-like EOS at $K_0 = 190 \pm 30$ MeV,³³⁰ likewise suggesting a comparatively soft EOS (see the region with blue backward stripes, labeled by “Le Fèvre *et al.*”). Also shown are results from the studies described in Sec. 3.4.1 (see the region with green vertical stripes, labeled by “Oliinychenko *et al.*”, where the shaded (unshaded) region corresponds to the 68% (95%) confidence interval)²⁴³ and in Sec. 3.4.2 (region with red forward stripes, labeled with “Omana Kuttan *et al.* (15 pts)”, corresponding to the 68% confidence interval for the analysis using 15 input data points).²⁴⁴

The comparison of EOSs constraints presented in Fig. 22 once again underscores the need to include momentum dependence of the potentials in simulations. The two older results suggest a softer EOS at small and moderate densities, compared to the results of the two Bayesian analyses, which can be attributed to the fact that the frameworks used in the former both included momentum dependence. On the other hand, it is apparent that the newer studies have the capability to describe a much more varied behavior of the EOS with density. The task for future studies is to merge these two features within one framework, allowing for a simultaneous comprehensive constraint on density- and momentum-dependence of the EOS, followed by similar extensions to include isospin-dependence, in-medium cross-sections, or cluster production mechanisms. The need for tighter and more reliable constraints is evident especially at high densities.

Moreover, given the complex evolution of heavy-ion collisions in this energy regime, a reliable constraint should describe not only proton observables. To underscore the wildly varying degrees to which simulations can describe different observables, Fig. 23 shows a comparison of flow observables for different species as measured by the STAR experiment⁴⁵⁵ and as obtained in three simulation frameworks: UrQMD, JAM, and SMASH. For results shown in the figure, both UrQMD and JAM simulations use an EOS characterized by $K_0 = 380$ MeV, while SMASH simulations use a c_s^2 -parametrized EOS characterized by $K_0 = 300$ MeV, $c_s^2[2, 3]n_0 = 0.47$, and $c_s^2[3, 4]n_0 = -0.08$, sampled from the posterior distribution obtained²⁴³ by fitting STAR proton flow data (see Sec. 3.4.1), including the data shown in the figure. Note that while all simulations describe the proton flow reasonably well, with SMASH showing the best agreement (unsurprisingly, since the used EOS has been constrained to describe this data), flow observables for other particle

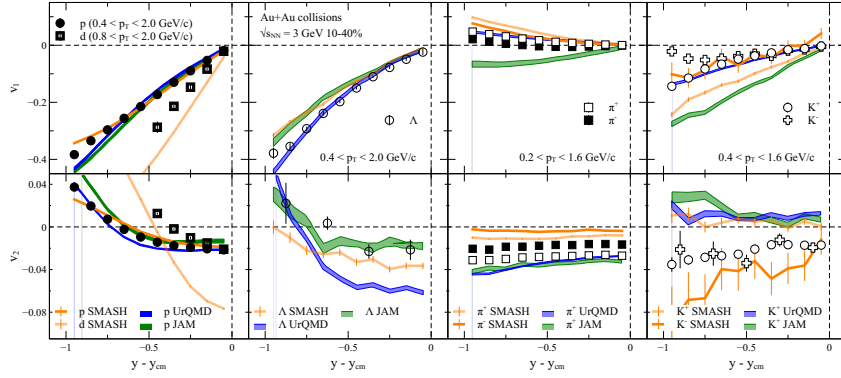


Fig. 23.: Directed (v_1 , *top*) and elliptic (v_2 , *bottom*) flow, integrated over p_T , of protons and deuterons (*left panels*), lambda baryons (*center-left panels*), pions (*center-right panels*), and kaons (*right panels*) as a function of rapidity. Experimental data points (symbols) are STAR measurements⁴⁵⁵ performed with Au+Au collisions at $\sqrt{s_{NN}} = 3$ GeV ($E_{kin} = 2.9$ GeV/nucleon) and 10–40% centrality. Bands represent results from microscopic transport models: **UrQMD** with an EOS characterized by $K_0 = 380$ MeV (blue bands),⁴⁵⁵ **JAM** with an EOS characterized by $K_0 = 380$ MeV (green bands),⁴⁵⁵ and **SMASH** with an EOS characterized by $K_0 = 300$ MeV at moderate densities and a significant softening at high densities.²⁴³

species are consistently rather poorly described by all of the codes. This suggests that the simulations must either miss or incorrectly treat components necessary to describe the entire system, and calls for further studies of and developing simulation algorithms for, among others, deuteron production, strange interactions, and meson interactions. Only when multiple observables of importance are well-described, or when deviations from experimental data can be reliably ascribed to elements of the simulations which do not significantly affect the EOS extraction, can constraints on the EOS be accepted at their face value.

4. Fluctuations: critical point, hydrodynamics, freeze-out

The description of the heavy-ion collisions is inherently statistical. Therefore, fluctuations are an essential part of that description. In this section we describe the status and the recent progress in understanding the physics of fluctuations, both in and out of equilibrium, with a particular focus on the role fluctuations play in mapping the QCD phase diagram and the search for the critical point.

4.1. Fluctuations in thermodynamics, critical fluctuations

4.1.1. Relation between equation of state and fluctuations

In thermodynamic equilibrium (by definition) the probability of the system to be found in a given *microscopic*, i.e., quantum, state depends only on the conserved quantum numbers of this state, such as energy, momentum, charge, etc. Therefore, the probability of a given *macroscopic* state, characterized by a given set of macroscopic variables, such the energy, is proportional to the number of microscopic states with these values of the macroscopic variables. That probability is equal to the exponential of the entropy, by definition. Therefore, the dependence of the entropy on energy, etc, i.e., the equation of state (EOS), determines the probability of the fluctuations for a system in thermodynamic equilibrium.⁴⁷²

This fundamental relationship between fluctuations and EOS has been exploited by Einstein⁴⁷³ to describe the singular behavior of the density fluctuations near critical points – the origin of the phenomenon of critical opalescence.

The entropy in question is the entropy of the open system which can exchange conserved quantities, such as energy and charge with the surroundings (thermodynamic bath) at temperature T and chemical potential μ . The corresponding probability distribution for the values of energy density ϵ and charge density n is given by

$$\mathcal{P}(\epsilon, n) \sim \exp \{V[s(\epsilon, n) - \beta\epsilon + \alpha n]\} \quad (72)$$

where $\beta = 1/T$, $\alpha = \mu/T$ and V is the volume of the thermodynamic system. In the thermodynamic limit, i.e., for large V , the probability is sharply peaked around the maximum determined by the familiar conditions:

$$\left(\frac{\partial s}{\partial \epsilon}\right)_n - \beta = 0, \quad \left(\frac{\partial s}{\partial n}\right)_\epsilon + \alpha = 0. \quad (73)$$

I.e., the entropy $s(\epsilon, n)$ determines the relationship between conserved densities ϵ , n and the corresponding thermodynamic quantities T and μ .

The quadratic form of second derivatives of the entropy must be negative to ensure thermodynamic stability. One can show that this form is diagonalized using variables $m \equiv s/n$ (specific entropy) and p (pressure). Probability of small fluctuations in terms of these variables is given by

$$\mathcal{P} \sim \exp \left\{ -\frac{V}{2} \left(\frac{n^2}{c_p} (\delta m)^2 + \frac{\beta}{wc_s^2} (\delta p)^2 \right) \right\} \quad (74)$$

The specific heat $c_p = Tn(\partial m/\partial T)_p$ diverges at the critical point. This corresponds to the probability of fluctuations developing a “flat direction” along $\delta p = 0$, where the fluctuations of the specific entropy $V\langle(\delta m)^2\rangle = c_p/n^2$ become large.^j The non-monotonic behavior of fluctuations as the critical point is being approached and passed during the QCD phase diagram scan has been proposed as a signature of the QCD critical point.^{474,475}

In this section we focus on the fluctuations intrinsic in any system which affords local thermodynamic, statistical description. These fluctuations are determined by the equation of state, as discussed above. In the context of heavy-ion collisions we must distinguish these fluctuations from the fluctuations which are determined by the initial state of the system. For example, from the fluctuations of the initial geometry of the system. In experiments, such separation is not always trivial. Typically it involves selecting collisions with similar centrality, i.e., similar collision geometry. The effects of the initial fluctuations are also qualitatively different from those of thermodynamic fluctuations in that the correlations induced by initial fluctuations are longer range (in longitudinal rapidity space) than the thermodynamic fluctuations we discuss.⁴⁷⁶ Most importantly, the $\sqrt{s_{NN}}$ dependence of the initial fluctuations does not reflect the *non-monotonicity* inherent in the thermodynamic fluctuations in the vicinity of the critical point.

4.1.2. Universality and non-gaussianity of critical fluctuations

Since the equation of state is universal near critical points, the fluctuation phenomena are also universal. In this section we shall describe the universal properties of the fluctuations which are relevant for the search for the QCD critical point in heavy-ion collisions.

Since the coefficient of the $(\delta m)^2$ term in Eq. (74) vanishes at the critical point, non-gaussian terms in Eq. (74) (δm^3 , etc) become important. This makes non-gaussianity of fluctuations a telltale signature of the critical point.

An important, and related, consequence of the vanishing of the coefficient of δm^2 is the divergence of the correlation length ξ of the fluctuations

^jOther thermodynamic quantities also develop large fluctuations at the critical point. For example, $V\langle(\delta n)^2\rangle = \chi_T T$, where $\chi_T = (\partial n/\partial \mu)_T$ is also divergent. The specific entropy $m = s/n$ is special from the hydrodynamic point of view. Unlike, e.g., baryon density, $m = s/n$ is a normal hydrodynamic mode in ideal hydrodynamics, i.e., being a ratio of conserved densities specific entropy is a diffusive mode which does not mix with propagating sound modes.

of m . In mean-field approximation $\langle(\delta m)^2\rangle \sim \xi^2$. The divergence of ξ leads to the breakdown of the mean-field approximation.^k The probability can no longer be considered as a function of the homogeneous (mean) value of δm . It is a functional of the field $\delta m(x)$. The corresponding scalar field theory, in the limit of the divergent correlation length, is universal. Any liquid-gas critical point is described by that theory, as well as other transitions characterized by a single-component order parameter, such as uniaxial (Ising) ferromagnets. The full details of the universal theory of critical phenomena are beyond the scope of this review, and are covered in many textbooks and reviews on critical phenomena.⁴⁷⁷ Here we shall emphasize only the basic properties which are most relevant for the critical point search in the beam energy scan experiments.

The theory of the QCD critical point fluctuations is in the universality class of the Ising model, i.e., ϕ^4 single-component scalar field theory in three dimensions. The mapping of variables between critical region of QCD and the critical region of the Ising model has been standardized²⁵⁰ using 6 parameters: T_c , μ_{Bc} , w , ρ , α_1 and α_2 . The parameters T_c and μ_{Bc} set the location of the QCD critical point, while α_1 is the angle of the slope of the coexistence line (first-order phase transition line) at the critical point in the T vs μ_B plane. It is also the slope of $m = \text{const}$ line at the critical point and is obtained by mapping the zero magnetization line (i.e., zero magnetic field $h = 0$) of the Ising model onto the QCD phase diagram. The angle α_2 is the angle of the line on the QCD phase diagram onto which the constant temperature line passing through the Ising critical point maps.

The nongaussian cumulants of the order parameter such as δm are the same as in the Ising model, but mapped into the QCD phase diagram. In particular, these cumulants contain singular contributions which diverge at the critical point with universal powers of the correlation length, given approximately by⁴⁷⁸

$$\Delta\langle(\delta m)^3\rangle \sim \xi^{4.5}, \quad \Delta\langle(\delta m)^4\rangle^c \sim \xi^7 \quad (75)$$

where Δ reminds us that this is a contribution to cumulants, singular at the critical point. In practice, it does not have to be dominant. The search for the critical point is aimed at detecting the non-monotonic dependence of fluctuations measures on the collision energy $\sqrt{s_{NN}}$ as the critical point is approached and passed, i.e., as the correlation length increases and then shrinks back to non-critical background, or baseline, values.

^kThe approximation is valid in the thermodynamic limit, i.e., $V/\xi^3 \rightarrow \infty$. This limit is in conflict with $\xi \rightarrow \infty$.

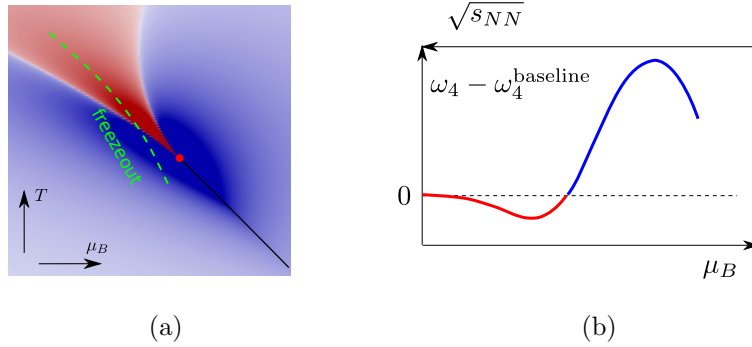


Fig. 24.: The equilibrium expectation for the quartic cumulant of fluctuations as a function of temperature and baryon chemical potential on the QCD phase diagram in the vicinity of the critical point. Red and blue colors reflect the sign of the cumulant – negative and positive respectively. The sign changes as the QCD phase diagram is scanned by varying $\sqrt{s_{NN}}$, and thus T and μ , along the freeze-out “trajectory” (dashed green line).

Unlike the quadratic cumulant $\langle(\delta m)^2\rangle$ which, being a measure of the width of the probability distribution, is positive, the cubic, and especially, the quartic cumulant could have either sign, since non-gaussian cumulants describe the *shape* of the distribution, or, more precisely, its deviation from Gaussian.

For example, the quartic cumulant around the QCD critical point is illustrated in Fig. 24(a).⁴⁷⁹ The resulting dependence on the collision energy, as it is varied in the region where the freeze-out occurs near the critical point, is illustrated in Fig. 24(b). The characteristic non-monotonicity of this cumulant is one of the signatures of the critical point searched for in the Beam Energy scan experiments.⁷

The most recently published experimental measurements of quartic cumulants by STAR collaboration indicate a non-monotonic dependence of the type similar to the one shown in Fig. 24(b) (see, e.g., Fig.4(2) in Ref. ⁴⁸⁰). While the magnitude of the cumulant sensitively depends on the EOS, and thus hard to predict (hence the lack of the vertical scale on Fig. 24(b)) the experimental results indicate that monotonic dependence is excluded at 3.1σ level.^{480–482} While not yet a definitive indication of the presence of the QCD critical point, this intriguing result motivates the second phase of the beam energy scan (BES-II) program which has collected higher statistics data being processed and analyzed currently.

In this review we shall focus on the recent progress achieved in connecting these equilibrium fluctuations to the experimental measurements. There are at least two intermediate steps between the equilibrium thermodynamic fluctuations and the experimental observables:

First, like thermodynamic variables themselves, their fluctuations evolve. This evolution is subject to conservation laws which may lead to significant memory effects, i.e., the lag of the fluctuations behind the equilibrium values.

Second, the thermodynamic/hydrodynamic quantities are not measured by experiments directly. An important step is connecting the fluctuations of these quantities to the observables, such as measures of particle multiplicity fluctuations and correlations.

The following two sections will review the recent developments in these two steps connecting theory and experiment.

4.2. Fluctuations in hydrodynamics

4.2.1. Stochastic hydrodynamics

There has been considerable recent progress in understanding and describing the *dynamics* of local thermodynamic fluctuations in an evolving medium making up a heavy-ion collision fireball.

There are two complementary approaches, which we shall refer to as stochastic and deterministic. Both begin with the Landau-Lifshits theory of hydrodynamic fluctuations.⁴⁸³ In this theory, generalized to relativistic context in Ref.⁴⁷⁶, the equations of hydrodynamics are *stochastic*. The evolution of the energy and momentum densities are described by the conservation law, as usual,

$$\partial_\mu \check{T}^{\mu\nu} = 0, \quad (76)$$

where the components of the stress-energy tensor $\check{T}^{\mu\nu}$ are stochastic variables (as indicated by the 'breve' accent). Since there are only four independent hydrodynamic variables, corresponding to conserved energy and momentum densities, the other six components of $\check{T}^{\mu\nu}$ are local functions of these four.¹ As usual, the independent variables are chosen to be the rest energy $\check{\epsilon}$ and four velocity \check{u} of the local fluid element and are related to $\check{T}^{\mu\nu}$ by the condition similar to Eq. (7):

$$\check{T}^{\mu\nu} \check{u}_\nu = \check{\epsilon} \check{u}^\mu. \quad (77)$$

¹For simplicity, in this discussion, we do not consider other hydrodynamic variables, such as baryon density. With an additional equation for baryon current conservation the extension to five (or more, if necessary) hydrodynamic variables is straightforward.⁴⁸⁴

The stress tensor in the local rest frame is then related to these independent variables by a local relationship, containing only spatial gradients in the local rest frame. This relation is stochastic, and contains a contribution of the local (point-like correlated on the hydrodynamic scale) noise $\check{S}^{\mu\nu}$:

$$\check{T}^{\mu\nu} = T^{\mu\nu}(\check{\epsilon}, \check{u}) + \check{S}^{\mu\nu} \quad (78)$$

where $T^{\mu\nu}(\epsilon, u)$ is the usual constituent relationship between the components of $T^{\mu\nu}$ and ϵ and u and their gradients, usually expanded to first order in gradients:

$$T^{\mu\nu}(\epsilon, u) = \epsilon u^\mu u^\nu - p(\epsilon)(g^{\mu\nu} - u^\mu u^\nu) + \text{viscous gradients}. \quad (79)$$

To complete this system of stochastic equations the correlation function

$$\langle \check{S}^{\mu\nu}(x_1) \check{S}^{\alpha\beta}(x_2) \rangle \sim \delta^{(4)}(x_1 - x_2) \quad (80)$$

is given by the fluctuation dissipation theorem, ensuring that the equilibrium fluctuations and correlations have the correct amplitudes in agreement with thermodynamics.

The evolution of fluctuations can be then described by, for example, directly simulating this system of stochastic equations. This, however, produces a problem (also known as infinite noise problem) due to the fact that the noise is singular at $x_1 = x_2$ in Eq. (80). The resulting solutions are dependent on the hydrodynamic cutoff, i.e., the finite elementary hydrodynamic cell size, b , complicating the ‘‘continuum limit’’ $b \rightarrow 0$. Some solutions to this problem within a numerical simulation have been proposed and implemented in the literature.^{485,486}

4.2.2. Deterministic approach to hydrodynamic fluctuations

The approach which deals with the infinite noise problem *before* the actual numerical simulation is performed has been also developed recently for Bjorken flow,^{487–489} for arbitrary relativistic flow,^{484,490,491} and for non-gaussian fluctuations.^{492,493} In this approach one expands in fluctuations around the average, e.g.,

$$\check{\epsilon} = \epsilon + \delta\epsilon, \quad \check{u} = u + \delta u, \quad (81)$$

thus obtaining stochastic equations for the fluctuations $\delta\epsilon$, δu on the deterministically evolving averaged background $\epsilon(x)$ and $u(x)$. These equations can then be used to derive *deterministic* equations obeyed by the *correlation functions* of the fluctuations, i.e., by averages of the products of the fluctuations, such as $\langle \delta\epsilon(x_1) \delta\epsilon(x_2) \rangle$.

The short-distance singularity of the noise results in ultraviolet divergences in the deterministic equations – the infinite noise problem. These divergent contributions modify the hydrodynamic equations by *local* terms which can be “renormalized” away by redefining the equation of state and transport coefficients in the constitutive equations. The resulting system of renormalized equations for hydrodynamic evolution of the renormalized average densities as well as the correlation functions is ultraviolet finite, i.e., cutoff independent, and the continuum limit can be taken.

After the renormalization the averaged hydrodynamic equations keep the form of usual hydrodynamic equations to first order in gradients with renormalized, i.e., physical, equation of state and transport coefficients. However, the finite (i.e., cutoff independent) fluctuation contributions appear beyond that order. These terms introduce contributions non-local in space (effectively being of order 3/2 in gradients) and also non-local in time, leading to the phenomena known as “long-time tails”.

The fluctuation correlators are expressed in terms of the Wigner-transformed equal-time correlation functions. For a fluid at rest globally, this definition is straightforward:

$$W_{ab}(t, \mathbf{x}; \mathbf{q}) = \int d^3 \mathbf{y} \langle \delta \Psi_a(t, \mathbf{x} + \mathbf{y}/2) \delta \Psi_b(t, \mathbf{x} - \mathbf{y}/2) \rangle e^{-i \mathbf{q} \cdot \mathbf{y}} \quad (82)$$

where $\delta \Psi_a$ is one of the fluctuation fields, e.g., $\delta \epsilon$ or δu , labeled by index a .

Nongaussianity of fluctuations, important for the critical point search, is described by *connected* correlation functions of $k > 2$ fluctuation fields:

$$H_{ab\dots}(t, \mathbf{x}_a, \mathbf{x}_b, \dots) \equiv \left\langle \underbrace{\delta \Psi_a(t, \mathbf{x}_a) \delta \Psi_b(t, \mathbf{x}_b) \dots}_{k \text{ fields}} \right\rangle^{\text{connected}} \quad (83)$$

The corresponding generalization of Wigner transform was introduced in Ref.⁴⁹² in terms of the Fourier integral with fixed midpoint $\mathbf{x} \equiv (\mathbf{x}_a + \mathbf{x}_b + \dots)/k$:

$$W_{ab\dots}(t, \mathbf{x}; \mathbf{q}_a, \mathbf{q}_b, \dots) \equiv \underbrace{\int d^3 \mathbf{y}_a e^{-i \mathbf{q}_a \cdot \mathbf{y}_a} \int d^3 \mathbf{y}_b e^{-i \mathbf{q}_b \cdot \mathbf{y}_b} \dots}_{k \text{ integrals}} \times \delta^{(3)} \left(\frac{\mathbf{y}_a + \mathbf{y}_b + \dots}{k} \right) H_{ab\dots}(t, \mathbf{x} + \mathbf{y}_a, \mathbf{x} + \mathbf{y}_b, \dots) \quad (84)$$

Due to the delta-function factor in Eq. (84), the function W does not change if all \mathbf{q} 's are shifted by the same vector. This means that one of the \mathbf{q} arguments is redundant. In practice, it is sufficient to know the function W

at all values of \mathbf{q} which add up to zero. In particular, the correlator $H_{ab\dots}$ can be obtained via inverse transformation:

$$H_{ab\dots}(t, \mathbf{x}_a, \mathbf{x}_b, \dots) = \underbrace{\int \frac{d^3 \mathbf{q}_a}{(2\pi)^3} e^{i\mathbf{q}_a \cdot \mathbf{y}_a} \int \frac{d^3 \mathbf{q}_b}{(2\pi)^3} e^{i\mathbf{q}_b \cdot \mathbf{y}_b} \dots}_{k \text{ integrals}} \times (2\pi)^3 \delta^{(3)}(\mathbf{q}_a + \mathbf{q}_b + \dots) W_{ab\dots}(t, \mathbf{x}; \mathbf{q}_a, \mathbf{q}_b, \dots). \quad (85)$$

For $k = 2$ the generalized Wigner function $W_{ab}(t, -\mathbf{q}, \mathbf{q})$ coincides with the usual 2-point Wigner function defined in Eq. (82).

The hierarchy of evolution equations was derived in Ref.⁴⁹² for fluctuations of density in a diffusion problem, where the only hydrodynamic variable is the diffusion charge density n which obeys conservation equation and the Fick's law with local noise

$$\partial_t n = -\nabla \cdot \mathbf{N}, \quad \mathbf{N} = -\lambda(n) \nabla \alpha(n) + \text{noise} \quad (86)$$

The evolution equations describe the relaxation of the k -point functions W_k of fluctuations of n to equilibrium values given by thermodynamics in terms of the equation of state $\alpha(n)$:

$$\partial_t W_2(\mathbf{q}) = -2 [\gamma \mathbf{q}^2 W_2(\mathbf{q}) - \lambda \mathbf{q}^2], \quad (87a)$$

$$\begin{aligned} \partial_t W_3(\mathbf{q}_1, \mathbf{q}_2, \mathbf{q}_3) = & -3 [\gamma \mathbf{q}_1^2 W_3(\mathbf{q}_2, \mathbf{q}_3) + \gamma' \mathbf{q}_1^2 W_2(\mathbf{q}_2) W_2(\mathbf{q}_3) \\ & + 2\lambda' \mathbf{q}_1 \cdot \mathbf{q}_2 W_2(\mathbf{q}_3)]_{\overline{123}}, \end{aligned} \quad (87b)$$

$$\begin{aligned} \partial_t W_4(\mathbf{q}_1, \mathbf{q}_2, \mathbf{q}_3, \mathbf{q}_4) = & -4 [\gamma \mathbf{q}_1^2 W_4(\mathbf{q}_2, \mathbf{q}_3, \mathbf{q}_4) \\ & + 3\gamma' \mathbf{q}_1^2 W_2(\mathbf{q}_2) W_3(\mathbf{q}_3, \mathbf{q}_4) + \gamma'' \mathbf{q}_1^2 W_2(\mathbf{q}_2) W_2(\mathbf{q}_3) W_2(\mathbf{q}_4) \\ & + 3\lambda' \mathbf{q}_1 \cdot \mathbf{q}_2 W_3(\mathbf{q}_3, \mathbf{q}_4) + 3\lambda'' \mathbf{q}_1 \cdot \mathbf{q}_2 W_2(\mathbf{q}_3) W_2(\mathbf{q}_4)]_{\overline{1234}}, \end{aligned} \quad (87c)$$

where $\gamma = \lambda\alpha'$. In Eqs. (87) we suppressed arguments t and \mathbf{x} , as they are the same for all functions W_n . Furthermore, note that all arguments of each function W_n add up to zero – reminiscent of the momentum conservation in Feynman diagrams. Therefore, to save space, we omitted the first argument in W_k where this argument can be inferred from the condition $\mathbf{q}_1 + \dots + \mathbf{q}_k = 0$. For example, $W_2(\mathbf{q}) \equiv W_2(\mathbf{q}) \equiv W_2(-\mathbf{q}, \mathbf{q})$ or $W_3(\mathbf{q}_3, \mathbf{q}_4) \equiv W_3(-\mathbf{q}_3 - \mathbf{q}_4, \mathbf{q}_3, \mathbf{q}_4)$. The symbol $[\dots]_{\overline{1\dots k}}$ denotes the sum over all permutations of $\mathbf{q}_1, \dots, \mathbf{q}_k$ divided by $1/k!$, i.e., the average over all permutations. Diagrammatic representation of Eqs. (87) is given in Ref.⁴⁹²

4.2.3. Confluent formalism for arbitrary relativistic flow

For a *relativistic* fluid with nontrivial velocity gradients the definition of the equal-time correlator in Eq. (83) and its Wigner transform are insufficient since the rest frame of the fluid is different at different space-time points, and the concept of “equal time” is thus ambiguous. Ref.,⁴⁸⁴ and for non-gaussian fluctuations, Ref.,⁴⁹³ define a generalization of the Wigner transform to this case by using local rest frame of the fluid at the midpoint $x \equiv (t, \mathbf{x})$ of the correlator. This removes an arbitrary lab frame from the definition of the correlator and allows fully Lorentz covariant formulation of hydrodynamics with fluctuations.

The idea is to equip every space-time point x with an orthonormal triad of basis 4-vectors $e_{\hat{a}}(x)$, $\hat{a} = 1, 2, 3$, or $\mathbf{e}(x)$, spatial in the local rest frame of the fluid at that point, i.e.,

$$\mathbf{e}(x) \cdot u(x) = \mathbf{0}. \quad (88)$$

One can then define equal-time k -point correlators as functions of k space-time points expressed as

$$x_1 = x + \mathbf{e}(x) \cdot \mathbf{y}_1, \quad \dots, \quad x_k = x + \mathbf{e}(x) \cdot \mathbf{y}_k, \quad (89)$$

in terms of the midpoint x and the separation 3-vectors $\mathbf{y}_1, \dots, \mathbf{y}_k$, which sum to zero: $\mathbf{y}_1 + \dots + \mathbf{y}_k = \mathbf{0}$.

Some of the fields in the correlator may not be Lorentz scalars, for example, fluctuations of velocity, δu . In this case, one would like to express fluctuations in a frame associated with the fluid, such as the local rest frame, rather than an arbitrary lab frame. The local rest frame of the fluid is, however, different for different points x_1, \dots, x_k . To use the same frame for all points while making sure that fluctuations represent deviations from fluid at rest locally, we boost the fluctuation variables (if they are not scalars) from the rest frame at the point they occur, say, at $x + \mathbf{y}_1$, to that at the midpoint x of the correlator. This operation leads to the *confluent correlator* defined as:

$$H_{a_1 \dots a_k}(x_1, \dots, x_k) \equiv \langle [\Lambda(x, x_1) \delta \Psi(x_1)]_{a_1} \dots [\Lambda(x, x_k) \delta \Psi(x_k)]_{a_k} \rangle^c \quad (90)$$

where $\Lambda(x, x_1)$ performs the boost on the corresponding fluctuation field $\delta \Psi(x_1)$ such that the 4-velocities in points x_1 and x are related by

$$\Lambda(x, x_1) u(x_1) = u(x). \quad (91)$$

Superscript “c” means “connected” as in Eq. (83).

We can now take the multipoint Wigner transform of the confluent correlator we just defined in Eq. (90) with respect to the 3-vectors $\mathbf{y}_1, \dots, \mathbf{y}_k$ describing separation of the points in the local basis at point x (cf. Eq. (84):

$$W_{a_1 \dots a_k}(x; \mathbf{q}_1, \dots, \mathbf{q}_k) \equiv \int d^3 \mathbf{y}_1 e^{-i \mathbf{q}_1 \cdot \mathbf{y}_1} \dots \int d^3 \mathbf{y}_k e^{-i \mathbf{q}_k \cdot \mathbf{y}_k} \\ \times \delta^{(3)} \left(\frac{\mathbf{y}_1 + \dots + \mathbf{y}_k}{k} \right) H_{a_1 \dots a_k}(x + \mathbf{e}(x) \cdot \mathbf{y}_1, \dots, x + \mathbf{e}(x) \cdot \mathbf{y}_k) \quad (92)$$

The inverse is given by (cf. Eq. (85))

$$H_{a_1 \dots a_k}(x + \mathbf{e}_1(x) \cdot \mathbf{y}_1, \dots, x + \mathbf{e}_k(x) \cdot \mathbf{y}_k) \\ = \int \frac{d^3 \mathbf{q}_1}{(2\pi)^3} e^{i \mathbf{q}_1 \cdot \mathbf{y}_1} \dots \int \frac{d^3 \mathbf{q}_k}{(2\pi)^3} e^{i \mathbf{q}_k \cdot \mathbf{y}_k} \\ \times \delta^{(3)} \left(\frac{\mathbf{q}_1 + \dots + \mathbf{q}_k}{2\pi} \right) W_{a_1 \dots a_k}(x; \mathbf{q}_1, \dots, \mathbf{q}_k). \quad (93)$$

Care must be taken also in defining a derivative with respect to the midpoint of such a correlation function in order to maintain the ‘‘equal-time in local rest frame’’ condition. The local rest frame is different in points x and $x + \Delta x$ used to define the derivative. A derivative which maintains ‘‘equal-time’’ condition is introduced in Ref. ^{484,491} and termed *confluent derivative*. It is defined via the $\Delta x \rightarrow 0$ limit of the following equation:

$$\Delta x \cdot \bar{\nabla} W_{a_1 \dots a_k}(x; \mathbf{q}_1, \dots, \mathbf{q}_k) \equiv \Lambda(x, x + \Delta x)_{a_1}^{b_1} \dots \Lambda(x, x + \Delta x)_{a_k}^{b_k} \\ \times W_{b_1 \dots b_k}(x; \mathbf{q}'_1, \dots, \mathbf{q}'_k) - W_{a_1 \dots a_k}(x; \mathbf{q}_1, \dots, \mathbf{q}_k), \quad (94)$$

where

$$\mathbf{q}' = \mathbf{e}(x + \Delta x) \cdot [\Lambda(x + \Delta x, x) \mathbf{e}(x) \cdot \mathbf{q}] \equiv R(x + \Delta x, x) \mathbf{q}. \quad (95)$$

In Eq. (94) the (non-scalar) fluctuation fields are boosted from point $x + \Delta x$ back to point x , similarly to the definition of the confluent correlator in Eq. (90). In addition, at $x + \Delta x$ we evaluate the function using the set of 3-wavevectors \mathbf{q}'_i given by Eq. (95), different from the set \mathbf{q}_i used at point x . The new set is obtained by representing each vector \mathbf{q} as a 4-vector orthogonal to $u(x)$, $\mathbf{e}(x) \cdot \mathbf{q}$, then boosting this vector to the rest frame at point $x + \Delta x$ and then expressing it again as a 3-vector, but now in the basis $\mathbf{e}(x + \Delta x)$ orthogonal to $u(x + \Delta x)$. The resulting transformation of vector \mathbf{q} is a rotation, denoted by R in Eq. (95).

Taking the limit $\Delta x \rightarrow 0$ one can express confluent derivative as follows:

$$\bar{\nabla}_\mu W_{a_1 \dots a_k} = \partial_\mu W_{a_1 \dots a_k} + k \left(\dot{\omega}_{\mu \dot{b}}^{\dot{a}} q_{1\dot{a}} \frac{\partial}{\partial q_{1\dot{b}}} W_{a_1 \dots a_k} - \bar{\omega}_{\mu a_1}^b W_{b a_2 \dots a_k} \right)_{1 \dots k}, \quad (96)$$

where the confluent connection $\bar{\omega}$ is a generator of the infinitesimal boost Λ and $\dot{\omega}$ is a generator of the infinitesimal rotation R :

$$\Lambda(x + \Delta x, x)_b^a = \delta_b^a - \Delta x^\mu \bar{\omega}_{\mu b}^a, \quad (97)$$

$$R(x + \Delta x, x)_{\dot{b}}^{\dot{a}} = \delta_{\dot{b}}^{\dot{a}} - \Delta x^\mu \dot{\omega}_{\mu \dot{b}}^{\dot{a}}. \quad (98)$$

The indices $a, b, a_1 \dots a_k$ label fluctuating fields. The confluent connection $\bar{\omega}_{\mu b}^a$ is nonzero when indices a, b refer to different components of a Lorentz vector (such as δu). In this case the connection satisfies

$$\bar{\nabla}_\mu u^\alpha \equiv \partial_\mu u^\alpha + \bar{\omega}_{\mu\beta}^\alpha u^\beta = 0, \quad (99)$$

(local velocity is “confluently” constant), which follows from Eqs. (91) and (97).^m

The rotation connection $\dot{\omega}$ is determined by Eqs. (95) and (98):

$$\dot{\omega}_{\mu \dot{a}}^{\dot{b}} = e_{\dot{a}}^{\dot{b}} \left(\partial_\mu e_{\dot{a}}^\alpha + \bar{\omega}_{\mu\beta}^\alpha e_{\dot{a}}^\beta \right). \quad (100)$$

Naturally, it satisfies:

$$\bar{\nabla}_\mu e_{\dot{a}}^\alpha \equiv \partial_\mu e_{\dot{a}}^\alpha + \bar{\omega}_{\mu\beta}^\alpha e_{\dot{a}}^\beta - \dot{\omega}_{\mu \dot{a}}^{\dot{b}} e_{\dot{b}}^\alpha = 0 \quad (101)$$

(local basis vectors are confluently constant).

The boost Λ is not defined uniquely by Eq. (91) – only up to a rotation keeping u unchanged. The simplest choice is the boost without additional rotation, which corresponds to confluent connection given explicitly by

$$\bar{\omega}_{\mu\beta}^\alpha = u_\beta \partial_\mu u^\alpha - u^\alpha \partial_\mu u_\beta. \quad (102)$$

For this choice of the confluent connection the rotation connection also simplifies to

$$\dot{\omega}_{\mu \dot{a}}^{\dot{b}} = e_{\dot{a}}^{\dot{b}} \partial_\mu e_{\dot{a}}^\alpha. \quad (103)$$

^mFor a scalar field (e.g., energy density, pressure fluctuations, etc) the confluent connection is, of course, zero.

4.2.4. Evolution equations for hydrodynamic fluctuations

There are five normal hydrodynamics modes, which can be described as two propagating modes and three diffusive.ⁿ The propagating modes correspond to fluctuations of pressure mixed with the fluctuations of the longitudinal (with respect to the wave vector \mathbf{q}) velocity. The frequency of these modes is $c_s|\mathbf{q}|$. The diffusive modes are the fluctuations of the specific entropy $m \equiv s/n_B$ at fixed pressure and transverse velocity. The relaxation rate of these modes is proportional to the square of their wavenumber \mathbf{q}^2 . The slowest diffusive mode near the critical point is specific entropy because its diffusion constant vanishes at the critical point.

In this review we shall focus on the slowest diffusive mode m for two reasons. First, because it is the slowest and therefore the furthest from equilibrium mode. Second, in equilibrium this mode shows the largest fluctuations, divergent at the critical point.

The evolution equation for the Wigner-transformed confluent two-point correlator of the specific entropy fluctuations, $\langle \delta m \delta m \rangle$, derived in Ref.⁴⁹¹ reads:

$$\mathcal{L}[W_{mm}(\mathbf{q})] = (\partial \cdot u)W_{mm}(\mathbf{q}) - 2\gamma_{mm}\mathbf{q}^2 \left[W_{mm}(\mathbf{q}) - \frac{c_p}{n^2} \right]. \quad (104)$$

where $\gamma_{mm} \equiv \kappa/c_p$ – the heat diffusion constant, and \mathcal{L} is the Liouville operator given by

$$\mathcal{L}[W_{mm}] \equiv \left[u \cdot \bar{\nabla} - \partial_\nu u^\mu e_\mu^{\dot{a}} e_b^\nu q_{\dot{a}} \frac{\partial}{\partial q_b} \right] W_{mm}. \quad (105)$$

The first term is the confluent derivative along the flow of the fluid, while the second describes stretching and/or rotation of the vectors \mathbf{q} due to the expansion and/or rotation of the fluid. In the case of expansion one can think of this term as describing the Hubble-like “red shift” of the fluctuation wavevector \mathbf{q} . For example, for Bjorken flow the Liouville operator takes the form

$$\mathcal{L}_{\text{Bj}} = \partial_\tau - \frac{q_3}{\tau} \frac{\partial}{\partial q_3}, \quad (106)$$

where the second term describes the “red shift”, or “stretching” of the wave number q_3 due to longitudinal expansion.^o

ⁿWe focus on hydrodynamics involving baryon charge. Each additional charge adds one diffusive mode to the count.

^oNaturally, we have chosen the triad of the 4 vectors e in such a way that the spatial part of the 4-vector e_3 points along the direction of the longitudinal flow, while the e_1 and e_2 are constant. In this case the rotation connection ($\hat{\omega}$) terms vanish in the confluent derivative in Eq. (96). The confluent connection ($\bar{\omega}$) terms are absent already for arbitrary flow because the fluctuating quantity, m , is a scalar.

The first term on the r.h.s. of Eq. (104), describes the scaling of the fluctuation magnitude with the volume of a hydrodynamic cell, as the cell expands at the rate $\partial \cdot u$. This trivial rescaling could be absorbed by multiplying W by a conserved density, such as the baryon density, n . The equation for a rescaled function $N_{mm} \equiv nW_{mm}$ is the same as in Eq. (104), but without the $\partial \cdot u$ term.

$$\mathcal{L}[N_{mm}(\mathbf{q})] = -2\gamma_{mm}\mathbf{q}^2 \left[N_{mm}(\mathbf{q}) - \frac{c_p}{n} \right]. \quad (107)$$

The last term in Eq. (104) describes diffusive relaxation of fluctuations towards equilibrium given by thermodynamic quantity c_p/n^2 (or c_p/n for N_{mm}).

It is instructive to compare Eq. (104) for W_{mm} (or the corresponding Eq. (107) for N_{mm}) to Eq. (87a) for the density-density correlator $\langle \delta n \delta n \rangle$ in the diffusion problem. The main difference is that the time derivative is replaced by the Liouville operator, which takes into account the flow of the fluid. The $(\partial \cdot u)$ term on the r.h.s. (absent when Eq. (104) is written in terms of N_{mm} , Eq. (107)) is also an effect of the flow – expansion. The diffusive relaxation terms are different because the correlated quantities are different, $\delta m \delta m$ in Eq. (104) and $\delta n \delta n$ in Eq. (87a). The coefficients, however, can be mapped onto each other via substitution

$$n \rightarrow m, \quad \gamma = \lambda \alpha' \rightarrow \gamma_{mm} = \frac{\kappa}{c_p}, \quad \lambda \rightarrow \frac{\kappa}{n^2}. \quad (108)$$

The evolution equations for non-gaussian correlators W_{mmm} and W_{mmmm} are qualitatively similar to those in the diffusion problem in Eq. (87b) and (87c). However, unlike the case of W_{mm} , where the whole equation (104) can be obtained from Eq. (87a) for W_2 by the substitution given by Eq. (108), only the terms containing leading singularities at the critical point can be obtained from Eq. (87b) and (87c) by the substitution (108). There are subleading singularities, which are due to the nonlinearity of the function $m(n)$ at constant pressure. These terms are written explicitly in Ref.⁴⁹³ and contain factors proportional to second and higher derivatives of m with respect to n at fixed pressure.

4.3. Freeze-out of fluctuations and observables

The previous section was devoted to recent progress in describing the evolution of fluctuations in hydrodynamics using correlators of hydrodynamic variables in coordinate space. Experiments do not measure such densities, or their correlations, directly. Instead the particle multiplicities and their

correlations in *momentum* space are measured. In this section we describe how to connect the theoretical description in terms of fluctuating hydrodynamics to experimental observables.

4.3.1. *Event-by-event fluctuations in heavy-ion collisions and their experimental measures*

Typical experimental measures are cumulants of the event-by-event fluctuations or correlations of particle multiplicities. For example, if N_p is the proton number in an event, its fluctuation in the event is $\delta N_p \equiv N_p - \langle N_p \rangle$ and $\langle (\delta N)^2 \rangle$ is its quadratic cumulant, or variance, where $\langle \dots \rangle$ is the event average. Higher-order cumulants, measuring non-gaussianity of fluctuations, are constructed similarly (see, e.g., Ref.⁷ for review).

In addition, correlations between particles can be also measured, such as $\langle \delta N_p \delta N_\pi \rangle$ – a correlation between proton and pion multiplicities. Such measures can also include higher-order correlators.⁴⁹⁴

Similar to correlation between species one can also consider correlations between particle with different momenta by counting particles within small momentum bins, or cells, labeled by the central momentum of the cell.

The number of particles dN_i in a given momentum cell dp^3 is given by Eq. (38) in terms of the phase space distribution function $f_i(x, p)$ integrated over the freeze-out hypersurface. Therefore the correlations between different momentum cells and/or between different species, can be expressed in terms of the correlation functions of fluctuations of $f_i(x, p)$. In this section we denote such fluctuations $\delta f \equiv f - \langle f \rangle$.^P

We shall also combine the species index (which includes all discrete quantum numbers, such as mass, spin, isospin, etc.) together with the coordinate and momentum into a single composite index $A = \{i, x, p\}$. Therefore, the general correlator which, upon integration over freeze-out surface, gives the observable correlation measures has the form

$$\langle \delta f_{i_A}(x_A, p_A) \delta f_{i_B}(x_B, p_B) \dots \rangle \equiv \langle \delta f_A \delta f_B \dots \rangle. \quad (109)$$

The freeze-out of hydrodynamic evolution was already discussed in Section 2.3. The Cooper-Frye prescription determines the event-by-event *averaged* distribution function $\langle f_A \rangle$ in terms of the hydrodynamic variables, or fields, $T(x)$ and $\mu(x)$, as in Eq. (14). In order to convert hydrodynamic *fluctuations* into particle event-by-event fluctuations we need an analogous freeze-out prescription for *correlators* in Eq. (109).

^PThis should not be confused with a similar notation used in Section 2.3.2 to denote deviation of $\langle f \rangle$ from equilibrium distribution f_{eq} .

4.3.2. Freeze-out of fluctuations and the maximum entropy method

The generalization of the Cooper-Frye freeze-out to fluctuations has been first considered in Ref.⁴⁷⁶ In the approach of Ref.⁴⁷⁶ the fluctuations of the phase space distribution function $f(x, p)$ are assumed to be caused by fluctuations of the hydrodynamic variables/fields $T(x)$ and $\mu(x)$ on which $f(x, p)$ depends. As a result, coordinate space correlations in $T(x)$ and $\mu(x)$ translate into the phase space correlations in $f(x, p)$.

This approach has an important flaw, which becomes obvious if one considers fluctuations in an (almost) ideal gas. In this case, there are fluctuations of hydrodynamic variables, such as charge density $n(x)$, but there are no momentum space correlations of $f(x, p)$, which would, nevertheless, be produced if the approach of Ref.⁴⁷⁶ were to be applied. Instead, the hydrodynamic fluctuations of $n(x)$ are matched on the particle side by trivial (Poisson, in the ideal gas case) *uncorrelated* fluctuations of the occupation numbers in each phase-space point.

This problem has been addressed in Ref.⁴⁹⁵ by subtracting this trivial ideal gas contribution from hydrodynamic fluctuations of $n(x)$ before applying the procedure of Ref.⁴⁷⁶ to the remainder, which is due to interactions and out-of-equilibrium dynamics.

Generalization of this approach to fluctuations of other hydrodynamic variables, and to non-gaussian fluctuations, proved elusive until the principle of maximum entropy for fluctuations was proposed and implemented in Ref.⁴⁹⁶ In this approach the matching of conserved hydrodynamic densities such as $\epsilon(x)$ and $n_q(x)$, defined in Eqs.(8), is done not simply on average, as, e.g., in Eqs. (39) or (40), but on an event-by-event basis. I.e.,⁹

$$\delta n_q(x) = \sum_i \int_p q_i \delta f_i(x, p) \equiv \int_{\tilde{A}} q_A \delta f_{\tilde{A}}(x) \equiv \int_A q_A \delta^{(3)}(x - x_A) \delta f_A, \quad (110)$$

where \int_p is a 3-integral over momenta with the Lorentz-invariant measure and \sum_i is a sum over the species of particles with id label i (corresponding to mass, spin, isospin, etc.) carrying charge q_i corresponding to density n_q (e.g., baryon charge when $n_q = n_B$ is the baryon density). We have also introduced a convenient shorthand $\int_{\tilde{A}}$ which denotes the sum and the momentum space integral together (but no space integration), i.e., the index $\tilde{A} = \{i, p\}$, while $A \equiv \{i_A, p_A, x_A\} = \{\tilde{A}, x_A\}$. Similarly $f_{\tilde{A}}(x_A) \equiv f_A$ (think of each particle species having its own phase space). Finally, we also introduced \int_A which includes integration over the whole phase space

⁹Eq. (110) can be obtained by multiplying *fluctuating* equation (39) by u_μ .

(momentum p_A and coordinate x_A) of each particle species. The delta function simply reflects the locality of freeze-out (i.e., each hydrodynamic cell is converted to particles located in the hydrodynamic cell at point x). Similarly, matching of the energy-momentum requires

$$\delta(\epsilon(x)u^\mu(x)) = \int_{\bar{A}} p^\mu \delta f_A(x) \equiv \int_A p^\mu \delta^{(3)}(x - x_A) \delta f_A. \quad (111)$$

It is convenient to organize equations such as Eqs. (110) and (111) into an indexed array, where lowercase index \tilde{a} runs through five hydrodynamic variables $\Psi_{\tilde{a}} = \{n_q, \epsilon u^\mu\}$:

$$\delta\Psi_a \equiv \delta\Psi_{\tilde{a}}(x_a) = \int_A P_a^A \delta f_A, \quad (112)$$

where

$$P_a^A = \{q_A, p_A^\mu\} \delta^{(3)}(x_a - x_A) \quad (113)$$

is the array of the contributions of a single particle A at point x_A to hydrodynamic densities $\Psi_{\tilde{a}} = \{n, \epsilon u^\mu\}$ in a cell around point x_a on the freeze-out surface. Similarly to particle index A it is convenient to view hydrodynamic field index a as a composite index labeling both the field and the point on the freeze-out surface where the value of this field is taken from, i.e., $a = \{\tilde{a}, x_a\}$.

Eq. (112) for fluctuations imply relationships between the hydrodynamic correlators in space points x_a, x_b , etc.

$$H_{ab\dots} \equiv \langle \delta\Psi_a \delta\Psi_b \dots \rangle \quad (114)$$

and particle correlators in phase-space points A, B , etc.

$$G_{AB\dots} \equiv \langle \delta f_A \delta f_B \dots \rangle \quad (115)$$

which have the form:

$$H_{ab\dots} = \int_{AB\dots} G_{AB\dots} P_a^A P_b^B \dots, \quad (116)$$

Equations (116) represent constraints on the particle correlators $G_{AB\dots}$ imposed by conservation laws. These constraints alone are not enough to completely determine $G_{AB\dots}$ simply because there are more “unknowns” $G_{AB\dots}$ than the constraints.

The situation is similar already for ensemble (i.e., event) averaged quantities, or one-point functions. In this case the averaged energy, momentum and baryon density are not sufficient alone to determine the particle distribution functions f_A . Additional input is needed. In the absence of additional information, the most natural solution is the one which maximizes

the entropy of the resonance gas into which the hydrodynamically evolved fireball freezes out. That entropy is given by the well-known functional of f_A :

$$S[f] = \int_A f_A (1 - \ln f_A), \quad (117)$$

(neglecting, for simplicity, quantum statistics). As observed recently in Ref.¹³⁵, maximizing $S[f]$, subject to the constraints on f_A imposed by conservation laws, produces the well-known Cooper-Frye freeze-out equation for particle phase-space distributions, which is widely and successfully used for describing experimental data for the last fifty or so years (see Section 2.3).

In order to apply the maximum entropy approach to fluctuation freeze-out, one needs the entropy of fluctuations as a functional of f_A as well as correlators $G_{AB\dots}$. Conceptually, this entropy, $S[f, G_{AB}, \dots]$ represents the (logarithm) of the number of the microscopic states in the resonance gas ensemble with the given set of correlators. The single particle entropy $S[f]$ is the value of $S[f, G_{AB}, \dots]$ when all correlators $G_{AB\dots}$ are given by their values in the equilibrium resonance gas.

The expression for the functional $S[f, G_{AB}, \dots]$ was found in Ref.⁴⁹⁶ For example, keeping only terms with out-of-equilibrium two-point correlators it reads

$$S_2[f, G] = S[f] + \frac{1}{2} \text{Tr} [\log(-CG) + CG + 1]. \quad (118)$$

The last term is always negative except for $G = C^{-1} \equiv \bar{G}$ which is the equilibrium value of the correlator G , where $C_{AB} = \delta^2 S[f] / (\delta f_A \delta f_B)$. When $G = \bar{G}$ the last term vanishes and S_2 is maximized with respect to G .

However, maximizing the entropy in Eq. (118) with respect to G under constraints in Eq. (116) gives

$$(G^{-1})^{AB} = (\bar{G}^{-1})^{AB} + (H^{-1} - \bar{H}^{-1})^{ab} P_a^A P_b^B. \quad (119)$$

In this equation and below the repeated lower case indices a, b , etc. imply summation over the set hydrodynamic variables $\Psi_a \equiv \Psi_{\bar{a}}(x_a)$ and volume integration over hydrodynamic cells at points x_a, x_b , etc. Due to the delta functions in the definition of P_a^A in Eq. (113), the integrals in Eq. (119) simply set the spatial arguments of $(G^{-1})^{AB}$ to those of $(H^{-1})^{ab}$, i.e., $x_A = x_a$ and $x_B = x_b$. When hydrodynamic correlator H equals its equilibrium value \bar{H} , so does G given by equation (119).

If deviations of fluctuations from equilibrium resonance gas are small, the equation (119) can be linearized in such deviations. The deviations

could be due to non-equilibrium effects, which have to be small for hydrodynamics to apply, or due to effects of the critical point, which could be small if we are not too close to the critical point. Linearized equation relates deviations of the particle correlators $\Delta G_{AB} = G_{AB} - \bar{G}_{AB}$ to the deviations of the hydrodynamics correlators $\Delta H_{ab} = H_{ab} - \bar{H}_{ab}$ from the resonance gas values:

$$\Delta G_{AB} = \Delta H_{ab} (\bar{H}^{-1} P \bar{G})_A^a (\bar{H}^{-1} P \bar{G})_B^b, \quad (120)$$

Similarly, the non-gaussian cumulants $G_{ABC\dots}$ of particle fluctuations can be expressed in terms of the non-gaussian cumulants of the hydrodynamic variables $H_{abc\dots}$. Such non-linear relations similar to Eq. (119) can be derived from the corresponding entropy functional found in Ref. ⁴⁹⁶ and we will not reproduce them here. Linearized relations valid for small deviations from the equilibrium resonance gas, however, are simple and instructive. The relationship is similar to Eq. (120), but instead of the “raw” deviations from equilibrium $\Delta G_{AB\dots}$ and $\Delta H_{ab\dots}$, i.e. correlations relative to equilibrium, the proportionality relation holds between *irreducible* relative correlators $\hat{\Delta} G_{AB\dots}$ defined in Ref. ⁴⁹⁶. An irreducible correlator $\hat{\Delta} G$ is different from the reducible “raw” relative correlator ΔG by subtraction of correlations involving only a smaller subset of the points $AB\dots$. The irreducible ΔH differs from ΔH similarly. The resulting linear relation generalizes Eq. (120):

$$\hat{\Delta} G_{AB\dots} = \hat{\Delta} H_{ab\dots} (\bar{H}^{-1} P \bar{G})_A^a (\bar{H}^{-1} P \bar{G})_B^b \dots, \quad (121)$$

where $\hat{\Delta} G_{AB\dots}$ and $\hat{\Delta} H_{ab\dots}$ denote *irreducible* relative correlators for particles and for hydrodynamic variables, respectively. For two-point (gaussian) correlators $\hat{\Delta} G = \Delta G$ and $\hat{\Delta} H = \Delta H$ and Eq. (119) reproduces Eq. (119).

Eq. (120) thus solves the problem of translating fluctuations in hydrodynamics into correlations between particles at freeze-out, in such a way as to obey the conservation laws on event-by-event basis. As one can see, it systematically eliminates spurious “self-correlations” discussed at the beginning of this section not only for gaussian, but also for non-gaussian cumulants.

Similarly to the way the maximum entropy approach reproduces and generalizes Cooper-Frye prescription for event *averaged* observables, the maximum entropy approach to fluctuations reproduces, justifies, and generalizes prior approaches to freezing out fluctuations, in particular, of critical fluctuations, as shown in Ref. ⁴⁹⁶. Such a prior approach involving fluctuating background field σ was introduced in Ref. ⁴⁷⁵ generalized to

non-gaussian fluctuations in Refs.,^{479,494} and then further generalized to *non-equilibrium* fluctuations in Ref.⁴⁹⁷

The σ -field approach,^{475,479,494} however, besides the knowledge of QCD EOS, requires the knowledge of the properties of the field σ such as its correlation length as well as its coupling to observed particles. These properties would depend on the nature of this field – an *a priori* unknown mixture of scalar fields such as chiral condensate, energy, and baryon number densities. It was also not clear how to deal with non-critical fluctuations or contributions of lower point correlations to higher-point correlators. All these uncertainties are absent in the maximum entropy approach. The correlations described by Eq. (121) are very similar to the correlations induced by the σ field given by a mixture of hydrodynamic fields determined by the QCD EOS itself.

The maximum entropy approach thus provides a direct connection between the fluctuations of the hydrodynamic quantities and the observed particle multiplicities, with their fluctuations. This connection is determined by the EOS of QCD in the resonance gas phase where the freeze-out occurs. The effects of the critical point and non-equilibrium are encoded in the non-trivial correlations described quantitatively by Eq. (121).

5. Summary and outlook

Investigations of relativistic heavy-ion collisions across a range of beam energies, and in particular in the range explored by the BES program at RHIC which covers the QCD transition region, is the primary method for systematically mapping the QCD phase diagram in controlled laboratory experiments. The significantly increased complexity of these events, compared to collisions at higher energies, is associated with non-trivial longitudinal dynamics, evolution of finite conserved charge densities, and non-equilibrium as well as potential critical phenomena, pose substantial challenges to theoretical descriptions of this compelling physics. Over the last decade, significant efforts have been dedicated to theoretical modeling and phenomenology aimed at understanding the interesting physics driving the dynamics of the created hot and dense QCD systems.

In this chapter, we adopted a pedagogical approach to reviewing theoretical descriptions of heavy-ion collision dynamics, with a particular focus on considerations at finite baryon density. These descriptions play a crucial role in model-to-data comparisons which will allow us to extract properties of QCD matter from experimental measurements. We delve into recent

developments in bulk medium dynamics, covering both multistage hydrodynamic approaches applicable for collisions at $\sqrt{s_{NN}} \gtrsim 7$ GeV (Section 2) and hadronic transport descriptions suitable for collisions at $\sqrt{s_{NN}} \lesssim 7$ GeV (Section 3). These recent advances in modeling the bulk evolution lay the foundation for studying fluctuations and their dynamics near the QCD critical point, and we provide an overview of recent developments in this intriguing area (Section 4).

Being a review of a rapidly developing research direction, this chapter can only hope to provide a snapshot of the current state of the art. Some questions still require more careful analyses while some theoretical tools, for example, those dealing with fluctuations, still need to be incorporated into a fully-fledged description of heavy-ion collisions before comparison with the experiment. Naturally, much of the future development of the field will be informed by the experimental data from the BES-II program at RHIC as well as from experiments at planned future heavy-ion collision facilities.⁴⁹⁸

Acknowledgments

This work was partly supported by the Natural Sciences and Engineering Research Council of Canada (L.D.), and partly by the U.S. Department of Energy, Office of Science, Office of Nuclear Physics, under Grants No. DE-FG02-00ER41132 (A.S.) and No. DE-FG0201ER41195 (M.S.). L.D. acknowledges C. Chattopadhyay, C. Gale, U. Heinz, S. Jaiswal, S. Jeon, B. Schenke, and C. Shen for useful comments on the manuscript. A.S. wants to thank Jan Steinheimer for helpful discussions, and Manjunath Omana Kuttan for sharing data tables.

References

1. C. Ratti, Lattice QCD and heavy ion collisions: a review of recent progress, *Rept. Prog. Phys.* **81**(8), 084301 (2018). doi: 10.1088/1361-6633/aabb97.
2. W.-j. Fu, QCD at finite temperature and density within the fRG approach: an overview, *Commun. Theor. Phys.* **74**(9), 097304 (2022). doi: 10.1088/1572-9494/ac86be.
3. A. M. Halasz, A. D. Jackson, R. E. Shrock, M. A. Stephanov, and J. J. M. Verbaarschot, On the phase diagram of QCD, *Phys. Rev.* **D58**, 096007 (1998). doi: 10.1103/PhysRevD.58.096007.
4. J. Berges and K. Rajagopal, Color superconductivity and chiral symmetry restoration at nonzero baryon density and temperature, *Nucl. Phys.* **B538**, 215–232 (1999). doi: 10.1016/S0550-3213(98)00620-8.

5. M. A. Stephanov, QCD Phase Diagram and the Critical Point, *Prog. Theor. Phys. Suppl.* **153**, 139–156 (2004). doi: 10.1143/PTPS.153.139.
6. M. Hippert, J. Grefa, T. A. Manning, J. Noronha, J. Noronha-Hostler, I. Portillo Vazquez, C. Ratti, R. Rougemont, and M. Trujillo, Bayesian location of the QCD critical point from a holographic perspective (9, 2023).
7. A. Bzdak, S. Esumi, V. Koch, J. Liao, M. Stephanov, and N. Xu, Mapping the Phases of Quantum Chromodynamics with Beam Energy Scan, *Phys. Rept.* **853**, 1–87 (2020). doi: 10.1016/j.physrep.2020.01.005.
8. D. Radice, S. Bernuzzi, and A. Perego, The Dynamics of Binary Neutron Star Mergers and GW170817, *Ann. Rev. Nucl. Part. Sci.* **70**, 95–119 (2020). doi: 10.1146/annurev-nucl-013120-114541.
9. V. Dexheimer, J. Noronha, J. Noronha-Hostler, C. Ratti, and N. Yunes, Future physics perspectives on the equation of state from heavy ion collisions to neutron stars, *J. Phys. G.* **48**(7), 073001 (2021). doi: 10.1088/1361-6471/abe104.
10. X. An et al., The BEST framework for the search for the QCD critical point and the chiral magnetic effect, *Nucl. Phys. A.* **1017**, 122343 (2022). doi: 10.1016/j.nuclphysa.2021.122343.
11. S. A. Bass and A. Dumitru, Dynamics of hot bulk QCD matter: From the quark gluon plasma to hadronic freezeout, *Phys. Rev. C.* **61**, 064909 (2000). doi: 10.1103/PhysRevC.61.064909.
12. D. Teaney, J. Lauret, and E. V. Shuryak, A Hydrodynamic Description of Heavy Ion Collisions at the SPS and RHIC (10, 2001).
13. T. Hirano, U. W. Heinz, D. Kharzeev, R. Lacey, and Y. Nara, Hadronic dissipative effects on elliptic flow in ultrarelativistic heavy-ion collisions, *Phys. Lett. B.* **636**, 299–304 (2006). doi: 10.1016/j.physletb.2006.03.060.
14. C. Nonaka and S. A. Bass, Space-time evolution of bulk QCD matter, *Phys. Rev. C.* **75**, 014902 (2007). doi: 10.1103/PhysRevC.75.014902.
15. H. Petersen, J. Steinheimer, G. Burau, M. Bleicher, and H. Stöcker, A Fully Integrated Transport Approach to Heavy Ion Reactions with an Intermediate Hydrodynamic Stage, *Phys. Rev. C.* **78**, 044901 (2008). doi: 10.1103/PhysRevC.78.044901.
16. K. Werner, I. Karpenko, T. Pierog, M. Bleicher, and K. Mikhailov, Event-by-Event Simulation of the Three-Dimensional Hydrodynamic Evolution from Flux Tube Initial Conditions in Ultrarelativistic Heavy Ion Collisions, *Phys. Rev. C.* **82**, 044904 (2010). doi: 10.1103/PhysRevC.82.044904.
17. H. Song, S. A. Bass, U. Heinz, T. Hirano, and C. Shen, 200 A GeV Au+Au collisions serve a nearly perfect quark-gluon liquid, *Phys. Rev. Lett.* **106**, 192301 (2011). doi: 10.1103/PhysRevLett.106.192301. [Erratum: *Phys.Rev.Lett.* 109, 139904 (2012)].
18. I. A. Karpenko, Y. M. Sinyukov, and K. Werner, Uniform description of bulk observables in the hydrokinetic model of $A + A$ collisions at the BNL Relativistic Heavy Ion Collider and the CERN Large Hadron Collider, *Phys. Rev. C.* **87**(2), 024914 (2013). doi: 10.1103/PhysRevC.87.024914.
19. K. Rajagopal, G. Ridgway, R. Weller, and Y. Yin, Understanding the out-of-equilibrium dynamics near a critical point in the QCD phase diagram,

- Phys. Rev. D.* **102**(9), 094025 (2020). doi: 10.1103/PhysRevD.102.094025.
20. L. Du, U. Heinz, K. Rajagopal, and Y. Yin, Fluctuation dynamics near the QCD critical point, *Phys. Rev. C.* **102**(5), 054911 (2020). doi: 10.1103/PhysRevC.102.054911.
 21. S. Cao, A. Majumder, R. Modarresi-Yazdi, I. Soudi, and Y. Tachibana, Jet Quenching: From Theory to Simulation (1, 2024).
 22. J. Churchill, L. Du, C. Gale, G. Jackson, and S. Jeon, Dilepton production at next-to-leading order and intermediate invariant-mass observables, *Phys. Rev. C.* **109**(4), 044915 (2024). doi: 10.1103/PhysRevC.109.044915.
 23. J. Churchill, L. Du, C. Gale, G. Jackson, and S. Jeon, Virtual Photons Shed Light on the Early Temperature of Dense QCD Matter, *Phys. Rev. Lett.* **132**(17), 172301 (2024). doi: 10.1103/PhysRevLett.132.172301.
 24. J. Churchill, L. Du, B. Forster, H. Gao, G. Jackson, S. Jeon, and C. Gale. Thermal dilepton production in heavy-ion collisions at beam-energy-scan (BES) energies. In *30th International Conference on Ultrarelativistic Nucleus-Nucleus Collisions* (12, 2023).
 25. C. Gale, S. Jeon, S. McDonald, J.-F. Paquet, and C. Shen, Photon radiation from heavy-ion collisions in the $\sqrt{s_{NN}} = 19 - 200$ GeV regime, *Nucl. Phys. A.* **982**, 767–770 (2019). doi: 10.1016/j.nuclphysa.2018.08.005.
 26. C. Shen, A. Noble, J.-F. Paquet, B. Schenke, and C. Gale. Illuminating early-stage dynamics of heavy-ion collisions through photons at RHIC BES energies. In *11th International Conference on Hard and Electromagnetic Probes of High-Energy Nuclear Collisions: Hard Probes 2023* (7, 2023).
 27. T. Hirano, P. Huovinen, K. Murase, and Y. Nara, Integrated Dynamical Approach to Relativistic Heavy Ion Collisions, *Prog. Part. Nucl. Phys.* **70**, 108–158 (2013). doi: 10.1016/j.pnpnp.2013.02.002.
 28. C. Gale, S. Jeon, and B. Schenke, Hydrodynamic Modeling of Heavy-Ion Collisions, *Int. J. Mod. Phys. A.* **28**, 1340011 (2013). doi: 10.1142/S0217751X13400113.
 29. H. Petersen, Anisotropic flow in transport + hydrodynamics hybrid approaches, *J. Phys. G.* **41**(12), 124005 (2014). doi: 10.1088/0954-3899/41/12/124005.
 30. Y. Nara, N. Otuka, A. Ohnishi, K. Niita, and S. Chiba, Study of relativistic nuclear collisions at AGS energies from p + Be to Au + Au with hadronic cascade model, *Phys. Rev. C.* **61**, 024901 (2000). doi: 10.1103/PhysRevC.61.024901.
 31. W. Cassing and E. L. Bratkovskaya, Parton transport and hadronization from the dynamical quasiparticle point of view, *Phys. Rev. C.* **78**, 034919 (2008). doi: 10.1103/PhysRevC.78.034919.
 32. M. Bleicher and E. Bratkovskaya, Modelling relativistic heavy-ion collisions with dynamical transport approaches, *Prog. Part. Nucl. Phys.* **122**, 103920 (2022). doi: 10.1016/j.pnpnp.2021.103920.
 33. K. Werner, The hadronic interaction model EPOS, *Nucl. Phys. B Proc. Suppl.* **175-176**, 81–87 (2008). doi: 10.1016/j.nuclphysbps.2007.10.012.
 34. Z.-W. Lin, C. M. Ko, B.-A. Li, B. Zhang, and S. Pal, A Multi-phase transport model for relativistic heavy ion collisions, *Phys. Rev. C.* **72**, 064901

- (2005). doi: 10.1103/PhysRevC.72.064901.
35. J. Weil et al., Particle production and equilibrium properties within a new hadron transport approach for heavy-ion collisions, *Phys. Rev. C* **94**(5), 054905 (2016). doi: 10.1103/PhysRevC.94.054905.
 36. S. A. Bass et al., Microscopic models for ultrarelativistic heavy ion collisions, *Prog. Part. Nucl. Phys.* **41**, 255–369 (1998). doi: 10.1016/S0146-6410(98)00058-1.
 37. M. Bleicher et al., Relativistic hadron hadron collisions in the ultrarelativistic quantum molecular dynamics model, *J. Phys. G* **25**, 1859–1896 (1999). doi: 10.1088/0954-3899/25/9/308.
 38. J. Aichelin, E. Bratkovskaya, A. Le Fèvre, V. Kireyeu, V. Kolesnikov, Y. Leifels, V. Voronyuk, and G. Coci, Parton-hadron-quantum-molecular dynamics: A novel microscopic n -body transport approach for heavy-ion collisions, dynamical cluster formation, and hypernuclei production, *Phys. Rev. C* **101**(4), 044905 (2020). doi: 10.1103/PhysRevC.101.044905.
 39. M. Luzum and H. Petersen, Initial State Fluctuations and Final State Correlations in Relativistic Heavy-Ion Collisions, *J. Phys. G* **41**, 063102 (2014). doi: 10.1088/0954-3899/41/6/063102.
 40. M. L. Miller, K. Reygers, S. J. Sanders, and P. Steinberg, Glauber modeling in high energy nuclear collisions, *Ann. Rev. Nucl. Part. Sci.* **57**, 205–243 (2007). doi: 10.1146/annurev.nucl.57.090506.123020.
 41. J. D. Bjorken, Highly Relativistic Nucleus-Nucleus Collisions: The Central Rapidity Region, *Phys. Rev. D* **27**, 140–151 (1983). doi: 10.1103/PhysRevD.27.140.
 42. C. Shen and B. Schenke, Dynamical initial state model for relativistic heavy-ion collisions, *Phys. Rev. C* **97**(2), 024907 (2018). doi: 10.1103/PhysRevC.97.024907.
 43. I. G. Bearden et al., Nuclear stopping in Au + Au collisions at $\sqrt{s_{NN}} = 200$ -GeV, *Phys. Rev. Lett.* **93**, 102301 (2004). doi: 10.1103/PhysRevLett.93.102301.
 44. K. Morita, S. Muroya, H. Nakamura, and C. Nonaka, Numerical analysis of two pion correlation based on a hydrodynamical model, *Phys. Rev. C* **61**, 034904 (2000). doi: 10.1103/PhysRevC.61.034904.
 45. T. Hirano, K. Morita, S. Muroya, and C. Nonaka, Hydrodynamical analysis of hadronic spectra in the 130 GeV/nucleon Au+Au collisions, *Phys. Rev. C* **65**, 061902 (2002). doi: 10.1103/PhysRevC.65.061902.
 46. T. Hirano, Is early thermalization achieved only near mid-rapidity at RHIC?, *Phys. Rev. C* **65**, 011901 (2002). doi: 10.1103/PhysRevC.65.011901.
 47. K. Morita, S. Muroya, C. Nonaka, and T. Hirano, Comparison of space-time evolutions of hot / dense matter in $\sqrt{s_{NN}} = 17$ -GeV and 130-GeV relativistic heavy ion collisions based on a hydrodynamical model, *Phys. Rev. C* **66**, 054904 (2002). doi: 10.1103/PhysRevC.66.054904.
 48. T. Hirano and K. Tsuda, Collective flow and two pion correlations from a relativistic hydrodynamic model with early chemical freezeout, *Phys. Rev. C* **66**, 054905 (2002). doi: 10.1103/PhysRevC.66.054905.

49. L. M. Satarov, A. V. Merdeev, I. N. Mishustin, and H. Stoecker, Longitudinal fluid-dynamics for ultrarelativistic heavy-ion collisions, *Phys. Rev. C* **75**, 024903 (2007). doi: 10.1103/PhysRevC.75.024903.
50. P. Bozek and I. Wyskiel, Rapid hydrodynamic expansion in relativistic heavy-ion collisions, *Phys. Rev. C* **79**, 044916 (2009). doi: 10.1103/PhysRevC.79.044916.
51. P. Bozek, Viscous evolution of the rapidity distribution of matter created in relativistic heavy-ion collisions, *Phys. Rev. C* **77**, 034911 (2008). doi: 10.1103/PhysRevC.77.034911.
52. P. Bozek and I. Wyskiel, Directed flow in ultrarelativistic heavy-ion collisions, *Phys. Rev. C* **81**, 054902 (2010). doi: 10.1103/PhysRevC.81.054902.
53. C. Shen and S. Alzhani, Collision-geometry-based 3D initial condition for relativistic heavy-ion collisions, *Phys. Rev. C* **102**(1), 014909 (2020). doi: 10.1103/PhysRevC.102.014909.
54. S. Ryu, V. Jovic, and C. Shen, Probing early-time longitudinal dynamics with the Λ hyperon's spin polarization in relativistic heavy-ion collisions, *Phys. Rev. C* **104**(5), 054908 (2021). doi: 10.1103/PhysRevC.104.054908.
55. S. Alzhani, S. Ryu, and C. Shen, Λ spin polarization in event-by-event relativistic heavy-ion collisions, *Phys. Rev. C* **106**(1), 014905 (2022). doi: 10.1103/PhysRevC.106.014905.
56. L. Du, C. Shen, S. Jeon, and C. Gale, Probing initial baryon stopping and equation of state with rapidity-dependent directed flow of identified particles, *Phys. Rev. C* **108**(4), L041901 (2023). doi: 10.1103/PhysRevC.108.L041901.
57. A. Bialas and W. Czyz, Wounded nucleon model and Deuteron-Gold collisions at RHIC, *Acta Phys. Polon. B* **36**, 905–918 (2005).
58. A. Bzdak, Forward-backward multiplicity correlations in the wounded nucleon model, *Phys. Rev. C* **80**, 024906 (2009). doi: 10.1103/PhysRevC.80.024906.
59. M. Gazdzicki and M. I. Gorenstein, Transparency, mixing and reflection of initial flows in relativistic nuclear collisions, *Phys. Lett. B* **640**, 155–161 (2006). doi: 10.1016/j.physletb.2006.07.044.
60. A. Bzdak and K. Wozniak, Forward-backward multiplicity fluctuations in heavy nuclei collisions in the wounded nucleon model, *Phys. Rev. C* **81**, 034908 (2010). doi: 10.1103/PhysRevC.81.034908.
61. P. Bozek, W. Broniowski, and J. Moreira, Torqued fireballs in relativistic heavy-ion collisions, *Phys. Rev. C* **83**, 034911 (2011). doi: 10.1103/PhysRevC.83.034911.
62. P. Bozek, W. Broniowski, and A. Olszewski, Hydrodynamic modeling of pseudorapidity flow correlations in relativistic heavy-ion collisions and the torque effect, *Phys. Rev. C* **91**, 054912 (2015). doi: 10.1103/PhysRevC.91.054912.
63. P. Bozek and W. Broniowski, The torque effect and fluctuations of entropy deposition in rapidity in ultra-relativistic nuclear collisions, *Phys. Lett. B* **752**, 206–211 (2016). doi: 10.1016/j.physletb.2015.11.054.
64. S. Chatterjee and P. Bozek, Large directed flow of open charm mesons

- probes the three dimensional distribution of matter in heavy ion collisions, *Phys. Rev. Lett.* **120**(19), 192301 (2018). doi: 10.1103/PhysRevLett.120.192301.
65. P. Bozek, Splitting of proton-antiproton directed flow in relativistic heavy-ion collisions, *Phys. Rev. C.* **106**(6), L061901 (2022). doi: 10.1103/PhysRevC.106.L061901.
 66. W. Ke, J. S. Moreland, J. E. Bernhard, and S. A. Bass, Constraints on rapidity-dependent initial conditions from charged particle pseudorapidity densities and two-particle correlations, *Phys. Rev. C.* **96**(4), 044912 (2017). doi: 10.1103/PhysRevC.96.044912.
 67. D. Soeder, W. Ke, J. F. Paquet, and S. A. Bass, Bayesian parameter estimation with a new three-dimensional initial-conditions model for ultrarelativistic heavy-ion collisions (6, 2023).
 68. J. S. Moreland, J. E. Bernhard, and S. A. Bass, Alternative ansatz to wounded nucleon and binary collision scaling in high-energy nuclear collisions, *Phys. Rev. C.* **92**(1), 011901 (2015). doi:10.1103/PhysRevC.92.011901.
 69. T. Ishii and S. Muroya, Hydrodynamical model analysis of the (3+1)-dimensional cylindrical symmetric baryon rich quark - gluon plasma with phase transition, *Phys. Rev. D.* **46**, 5156–5167 (1992). doi: 10.1103/PhysRevD.46.5156.
 70. B. B. Back et al., Baryon rapidity loss in relativistic Au+Au collisions, *Phys. Rev. Lett.* **86**, 1970–1973 (2001). doi: 10.1103/PhysRevLett.86.1970.
 71. G. S. Denicol, C. Gale, S. Jeon, A. Monnai, B. Schenke, and C. Shen, Net baryon diffusion in fluid dynamic simulations of relativistic heavy-ion collisions, *Phys. Rev. C.* **98**(3), 034916 (2018). doi: 10.1103/PhysRevC.98.034916.
 72. L. Du, X. An, and U. Heinz, Baryon transport and the QCD critical point, *Phys. Rev. C.* **104**(6), 064904 (2021). doi: 10.1103/PhysRevC.104.064904.
 73. L. Du, H. Gao, S. Jeon, and C. Gale, Rapidity scan with multistage hydrodynamic and statistical thermal models, *Phys. Rev. C.* **109**(1), 014907 (2024). doi: 10.1103/PhysRevC.109.014907.
 74. D. Kharzeev, Can gluons trace baryon number?, *Phys. Lett. B.* **378**, 238–246 (1996). doi: 10.1016/0370-2693(96)00435-2.
 75. T. Sjostrand and P. Z. Skands, Baryon number violation and string topologies, *Nucl. Phys. B.* **659**, 243 (2003). doi: 10.1016/S0550-3213(03)00193-7.
 76. T. Parida and S. Chatterjee, Directed flow in a baryonic fireball (11, 2022).
 77. K. Kajantie and L. D. McLerran, Initial Conditions for Hydrodynamical Calculations of Ultrarelativistic Nuclear Collisions, *Phys. Lett. B.* **119**, 203–206 (1982). doi: 10.1016/0370-2693(82)90277-5.
 78. K. Kajantie and L. D. McLerran, Energy Densities, Initial Conditions and Hydrodynamic Equations for Ultrarelativistic Nucleus-nucleus Collisions, *Nucl. Phys. B.* **214**, 261–284 (1983). doi: 10.1016/0550-3213(83)90662-4.
 79. C. Shen and B. Schenke, Longitudinal dynamics and particle production in relativistic nuclear collisions, *Phys. Rev. C.* **105**(6), 064905 (2022). doi: 10.1103/PhysRevC.105.064905.

80. L. Du, U. Heinz, and G. Vujanovic, Hybrid model with dynamical sources for heavy-ion collisions at BES energies, *Nucl. Phys. A.* **982**, 407–410 (2019). doi: 10.1016/j.nuclphysa.2018.09.015.
81. Y. Akamatsu, M. Asakawa, T. Hirano, M. Kitazawa, K. Morita, K. Murase, Y. Nara, C. Nonaka, and A. Ohnishi, Dynamically integrated transport approach for heavy-ion collisions at high baryon density, *Phys. Rev. C.* **98** (2), 024909 (2018). doi: 10.1103/PhysRevC.98.024909.
82. A. De, J. I. Kapusta, M. Singh, and T. Welle, Comprehensive simulation of heavy-ion collisions at nonzero baryon chemical potential, *Phys. Rev. C.* **106**(5), 054906 (2022). doi: 10.1103/PhysRevC.106.054906.
83. J. Berges, M. P. Heller, A. Mazeliauskas, and R. Venugopalan, QCD thermalization: Ab initio approaches and interdisciplinary connections, *Rev. Mod. Phys.* **93**(3), 035003 (2021). doi: 10.1103/RevModPhys.93.035003.
84. S. Schlichting and D. Teaney, The First fm/c of Heavy-Ion Collisions, *Ann. Rev. Nucl. Part. Sci.* **69**, 447–476 (2019). doi: 10.1146/annurev-nucl-101918-023825.
85. A. Monnai and B. Schenke, Pseudorapidity correlations in heavy ion collisions from viscous fluid dynamics, *Phys. Lett. B.* **752**, 317–321 (2016). doi: 10.1016/j.physletb.2015.11.063.
86. L. Du. *Hydrodynamic description of the baryon-charged quark-gluon plasma*. PhD thesis, Ohio State U. (2021).
87. I. A. Karpenko, P. Huovinen, H. Petersen, and M. Bleicher, Estimation of the shear viscosity at finite net-baryon density from $A + A$ collision data at $\sqrt{s_{NN}} = 7.7 - 200$ GeV, *Phys. Rev. C.* **91**(6), 064901 (2015). doi: 10.1103/PhysRevC.91.064901.
88. A. Schäfer, I. Karpenko, X.-Y. Wu, J. Hammelmann, and H. Elfner, Particle production in a hybrid approach for a beam energy scan of Au+Au/Pb+Pb collisions between $\sqrt{s_{NN}} = 4.3$ GeV and $\sqrt{s_{NN}} = 200.0$ GeV, *Eur. Phys. J. A.* **58**(11), 230 (2022). doi: 10.1140/epja/s10050-022-00872-x.
89. L. Pang, Q. Wang, and X.-N. Wang, Effects of initial flow velocity fluctuation in event-by-event (3+1)D hydrodynamics, *Phys. Rev. C.* **86**, 024911 (2012). doi: 10.1103/PhysRevC.86.024911.
90. M. Li and J. I. Kapusta, High Baryon Densities in Heavy Ion Collisions at Energies Attainable at the BNL Relativistic Heavy Ion Collider and the CERN Large Hadron Collider, *Phys. Rev. C.* **95**(1), 011901 (2017). doi: 10.1103/PhysRevC.95.011901.
91. L. D. McLerran, S. Schlichting, and S. Sen, Spacetime picture of baryon stopping in the color-glass condensate, *Phys. Rev. D.* **99**(7), 074009 (2019). doi: 10.1103/PhysRevD.99.074009.
92. M. Li and J. I. Kapusta, Large Baryon Densities Achievable in High Energy Heavy Ion Collisions Outside the Central Rapidity Region, *Phys. Rev. C.* **99**(1), 014906 (2019). doi: 10.1103/PhysRevC.99.014906.
93. J. Casalderrey-Solana, D. Mateos, W. van der Schee, and M. Triana, Holographic heavy ion collisions with baryon charge, *JHEP.* **09**, 108 (2016). doi: 10.1007/JHEP09(2016)108.
94. W. van der Schee and B. Schenke, Rapidity dependence in holographic heavy

- ion collisions, *Phys. Rev. C* **92**(6), 064907 (2015). doi: 10.1103/PhysRevC.92.064907.
95. M. Attems, Y. Bea, J. Casalderrey-Solana, D. Mateos, M. Triana, and M. Zilhão, Holographic Collisions across a Phase Transition, *Phys. Rev. Lett.* **121**(26), 261601 (2018). doi: 10.1103/PhysRevLett.121.261601.
 96. I. Kolbé, M. Lushozi, L. D. McLerran, and G. Yu, Distribution of Nuclear Matter and Radiation in the Fragmentation Region, *Phys. Rev. C* **103**(4), 044908 (2021). doi: 10.1103/PhysRevC.103.044908.
 97. R. P. G. Andrade, F. Grassi, Y. Hama, T. Kodama, and W. L. Qian, Importance of Granular Structure in the Initial Conditions for the Elliptic Flow, *Phys. Rev. Lett.* **101**, 112301 (2008). doi: 10.1103/PhysRevLett.101.112301.
 98. H. J. Drescher, S. Ostapchenko, T. Pierog, and K. Werner, Initial condition for QGP evolution from NEXUS, *Phys. Rev. C* **65**, 054902 (2002). doi: 10.1103/PhysRevC.65.054902.
 99. Y. B. Ivanov, Alternative Scenarios of Relativistic Heavy-Ion Collisions: I. Baryon Stopping, *Phys. Rev. C* **87**(6), 064904 (2013). doi: 10.1103/PhysRevC.87.064904.
 100. Y. B. Ivanov, Alternative Scenarios of Relativistic Heavy-Ion Collisions: II. Particle Production, *Phys. Rev. C* **87**(6), 064905 (2013). doi: 10.1103/PhysRevC.87.064905.
 101. Y. B. Ivanov, Alternative Scenarios of Relativistic Heavy-Ion Collisions: III. Transverse Momentum Spectra, *Phys. Rev. C* **89**(2), 024903 (2014). doi: 10.1103/PhysRevC.89.024903.
 102. J. Cimerman, I. Karpenko, B. Tomasik, and P. Huovinen, Next-generation multifluid hydrodynamic model for nuclear collisions at $\sqrt{s_{\text{NN}}}$ from a few GeV to a hundred GeV, *Phys. Rev. C* **107**(4), 044902 (2023). doi: 10.1103/PhysRevC.107.044902.
 103. Y. Kanakubo, Y. Tachibana, and T. Hirano, Unified description of hadron yield ratios from dynamical core-corona initialization, *Phys. Rev. C* **101**(2), 024912 (2020). doi: 10.1103/PhysRevC.101.024912.
 104. Y. Kanakubo, Y. Tachibana, and T. Hirano, Interplay between core and corona components in high-energy nuclear collisions, *Phys. Rev. C* **105**(2), 024905 (2022). doi: 10.1103/PhysRevC.105.024905.
 105. M. Okai, K. Kawaguchi, Y. Tachibana, and T. Hirano, New approach to initializing hydrodynamic fields and mini-jet propagation in quark-gluon fluids, *Phys. Rev. C* **95**(5), 054914 (2017). doi: 10.1103/PhysRevC.95.054914.
 106. D. Pablos, M. Singh, S. Jeon, and C. Gale, Minijet quenching in a concurrent jet+hydro evolution and the nonequilibrium quark-gluon plasma, *Phys. Rev. C* **106**(3), 034901 (2022). doi: 10.1103/PhysRevC.106.034901.
 107. A. Adil and M. Gyulassy, 3D jet tomography of twisted strongly coupled quark gluon plasmas, *Phys. Rev. C* **72**, 034907 (2005). doi: 10.1103/PhysRevC.72.034907.
 108. A. Adil, M. Gyulassy, and T. Hirano, 3D jet tomography of the twisted color glass condensate, *Phys. Rev. D* **73**, 074006 (2006). doi: 10.1103/PhysRevD.73.074006.
 109. P. Carzon, M. Martinez, M. D. Sievert, D. E. Wertepny, and J. Noronha-

- Hostler, Monte Carlo event generator for initial conditions of conserved charges in nuclear geometry, *Phys. Rev. C* **105**(3), 034908 (2022). doi: 10.1103/PhysRevC.105.034908.
110. P. Carzon, M. Martinez, J. Noronha-Hostler, P. Plaschke, S. Schlichting, and M. Sievert, Pre-equilibrium evolution of conserved charges with initial conditions in the ICCING Monte Carlo event generator, *Phys. Rev. C* **108**(6), 064905 (2023). doi: 10.1103/PhysRevC.108.064905.
 111. A. Monnai, Landau and Eckart frames for relativistic fluids in nuclear collisions, *Phys. Rev. C* **100**(1), 014901 (2019). doi: 10.1103/PhysRevC.100.014901.
 112. J. A. Fotakis, E. Molnár, H. Niemi, C. Greiner, and D. H. Rischke, Multi-component relativistic dissipative fluid dynamics from the Boltzmann equation, *Phys. Rev. D* **106**(3), 036009 (2022). doi: 10.1103/PhysRevD.106.036009.
 113. G. S. Rocha, D. Wagner, G. S. Denicol, J. Noronha, and D. H. Rischke, Theories of Relativistic Dissipative Fluid Dynamics (11, 2023).
 114. S. Jeon and U. Heinz, Introduction to Hydrodynamics, *Int. J. Mod. Phys. E* **24**(10), 1530010 (2015). doi: 10.1142/S0218301315300106.
 115. C. Chattopadhyay, U. Heinz, and T. Schaefer, Far-off-equilibrium expansion trajectories in the QCD phase diagram, *Phys. Rev. C* **107**(4), 044905 (2023). doi: 10.1103/PhysRevC.107.044905.
 116. I. Muller, Zum Paradoxon der Wärmeleitungstheorie, *Z. Phys.* **198**, 329–344 (1967). doi: 10.1007/BF01326412.
 117. W. Israel and J. M. Stewart, Transient relativistic thermodynamics and kinetic theory, *Annals Phys.* **118**, 341–372 (1979). doi: 10.1016/0003-4916(79)90130-1.
 118. G. S. Denicol, Kinetic foundations of relativistic dissipative fluid dynamics, *J. Phys. G* **41**(12), 124004 (2014). doi: 10.1088/0954-3899/41/12/124004.
 119. G. S. Denicol, H. Niemi, E. Molnar, and D. H. Rischke, Derivation of transient relativistic fluid dynamics from the Boltzmann equation, *Phys. Rev. D* **85**, 114047 (2012). doi: 10.1103/PhysRevD.85.114047. [Erratum: *Phys.Rev.D* 91, 039902 (2015)].
 120. J. Hu and S. Shi, Multicomponent second-order dissipative relativistic hydrodynamics with binary reactive collisions, *Phys. Rev. D* **106**(1), 014007 (2022). doi: 10.1103/PhysRevD.106.014007.
 121. C. V. Brito and G. S. Denicol, Linear stability of Israel-Stewart theory in the presence of net-charge diffusion, *Phys. Rev. D* **102**(11), 116009 (2020). doi: 10.1103/PhysRevD.102.116009.
 122. D. Almaalol, T. Dore, and J. Noronha-Hostler, Stability of multi-component relativistic viscous hydrodynamics from Israel-Stewart and reproducing DNMR from maximizing the entropy (9, 2022).
 123. M. Prakash, M. Prakash, R. Venugopalan, and G. Welke, Nonequilibrium properties of hadronic mixtures, *Phys. Rept.* **227**, 321–366 (1993). doi: 10.1016/0370-1573(93)90092-R.
 124. A. Monnai and T. Hirano, Relativistic Dissipative Hydrodynamic Equations at the Second Order for Multi-Component Systems with Multiple Conserved

- Currents, *Nucl. Phys. A.* **847**, 283–314 (2010). doi: 10.1016/j.nuclphysa.2010.08.002.
125. A. Monnai, Dissipative Hydrodynamic Effects on Baryon Stopping, *Phys. Rev. C.* **86**, 014908 (2012). doi: 10.1103/PhysRevC.86.014908.
 126. Y. Kikuchi, K. Tsumura, and T. Kunihiro, Derivation of second-order relativistic hydrodynamics for reactive multicomponent systems, *Phys. Rev. C.* **92**(6), 064909 (2015). doi: 10.1103/PhysRevC.92.064909.
 127. A. Jaiswal, B. Friman, and K. Redlich, Relativistic second-order dissipative hydrodynamics at finite chemical potential, *Phys. Lett. B.* **751**, 548–552 (2015). doi: 10.1016/j.physletb.2015.11.018.
 128. J. A. Fotakis, M. Greif, C. Greiner, G. S. Denicol, and H. Niemi, Diffusion processes involving multiple conserved charges: A study from kinetic theory and implications to the fluid-dynamical modeling of heavy ion collisions, *Phys. Rev. D.* **101**(7), 076007 (2020). doi: 10.1103/PhysRevD.101.076007.
 129. L. Du, X. An, and U. Heinz, Baryon diffusion near the QCD critical point, *PoS. CPOD2021*, 024 (2022). doi: 10.22323/1.400.0024.
 130. T. Dore, J. M. Karthein, I. Long, D. Mroczek, J. Noronha-Hostler, P. Parotto, C. Ratti, and Y. Yamauchi, Critical lensing and kurtosis near a critical point in the QCD phase diagram in and out of equilibrium, *Phys. Rev. D.* **106**(9), 094024 (2022). doi: 10.1103/PhysRevD.106.094024.
 131. I. Bouras, E. Molnar, H. Niemi, Z. Xu, A. El, O. Fochler, C. Greiner, and D. H. Rischke, Investigation of shock waves in the relativistic Riemann problem: A Comparison of viscous fluid dynamics to kinetic theory, *Phys. Rev. C.* **82**, 024910 (2010). doi: 10.1103/PhysRevC.82.024910.
 132. A. Jaiswal, Relativistic dissipative hydrodynamics from kinetic theory with relaxation time approximation, *Phys. Rev. C.* **87**(5), 051901 (2013). doi: 10.1103/PhysRevC.87.051901.
 133. W. Florkowski, E. Maksymiuk, and R. Ryblewski, Anisotropic-hydrodynamics approach to a quark-gluon fluid mixture, *Phys. Rev. C.* **97**(1), 014904 (2018). doi: 10.1103/PhysRevC.97.014904.
 134. D. Almaalol, M. Alqahtani, and M. Strickland, Anisotropic hydrodynamics with number-conserving kernels, *Phys. Rev. C.* **99**(1), 014903 (2019). doi: 10.1103/PhysRevC.99.014903.
 135. D. Everett, C. Chattopadhyay, and U. Heinz, Maximum entropy kinetic matching conditions for heavy-ion collisions, *Phys. Rev. C.* **103**(6), 064902 (2021). doi: 10.1103/PhysRevC.103.064902.
 136. C. Chattopadhyay, U. Heinz, and T. Schaefer, Fluid dynamics from the Boltzmann equation using a maximum entropy distribution, *Phys. Rev. C.* **108**(3), 034907 (2023). doi: 10.1103/PhysRevC.108.034907.
 137. G. S. Rocha, G. S. Denicol, and J. Noronha, Novel Relaxation Time Approximation to the Relativistic Boltzmann Equation, *Phys. Rev. Lett.* **127**(4), 042301 (2021). doi: 10.1103/PhysRevLett.127.042301.
 138. L. Du and U. Heinz, (3+1)-dimensional dissipative relativistic fluid dynamics at non-zero net baryon density, *Comput. Phys. Commun.* **251**, 107090 (2020). doi: 10.1016/j.cpc.2019.107090.
 139. I. Karpenko, P. Huovinen, and M. Bleicher, A 3+1 dimensional viscous hy-

- drodynamic code for relativistic heavy ion collisions, *Comput. Phys. Commun.* **185**, 3016–3027 (2014). doi: 10.1016/j.cpc.2014.07.010.
140. L.-G. Pang, H. Petersen, and X.-N. Wang, Pseudorapidity distribution and decorrelation of anisotropic flow within the open-computing-language implementation CLVisc hydrodynamics, *Phys. Rev. C* **97**(6), 064918 (2018). doi: 10.1103/PhysRevC.97.064918.
 141. X.-Y. Wu, G.-Y. Qin, L.-G. Pang, and X.-N. Wang, (3+1)-D viscous hydrodynamics at finite net baryon density: Identified particle spectra, anisotropic flows, and flow fluctuations across energies relevant to the beam-energy scan at RHIC, *Phys. Rev. C* **105**(3), 034909 (2022). doi: 10.1103/PhysRevC.105.034909.
 142. D. Everett et al., Multisystem Bayesian constraints on the transport coefficients of QCD matter, *Phys. Rev. C* **103**(5), 054904 (2021). doi: 10.1103/PhysRevC.103.054904.
 143. D. Everett et al., Phenomenological constraints on the transport properties of QCD matter with data-driven model averaging, *Phys. Rev. Lett.* **126**(24), 242301 (2021). doi: 10.1103/PhysRevLett.126.242301.
 144. G. Nijs, W. van der Schee, U. Gürsoy, and R. Snellings, Transverse momentum differential global analysis of heavy-ion collisions, *Phys. Rev. Lett.* **126**(20), 202301 (2021). doi: 10.1103/PhysRevLett.126.202301.
 145. G. Nijs, W. van der Schee, U. Gürsoy, and R. Snellings, Bayesian analysis of heavy ion collisions with the heavy ion computational framework Trajectum, *Phys. Rev. C* **103**(5), 054909 (2021). doi: 10.1103/PhysRevC.103.054909.
 146. G. D. Moore. Shear viscosity in QCD and why it's hard to calculate. In *Criticality in QCD and the Hadron Resonance Gas* (10, 2020).
 147. S. Gavin, Transport coefficients in ultrarelativistic heavy ion collisions, *Nucl. Phys. A* **435**, 826–843 (1985). doi: 10.1016/0375-9474(85)90190-3.
 148. S. Jeon and L. G. Yaffe, From quantum field theory to hydrodynamics: Transport coefficients and effective kinetic theory, *Phys. Rev. D* **53**, 5799–5809 (1996). doi: 10.1103/PhysRevD.53.5799.
 149. G. S. Denicol, S. Jeon, and C. Gale, Transport Coefficients of Bulk Viscous Pressure in the 14-moment approximation, *Phys. Rev. C* **90**(2), 024912 (2014). doi: 10.1103/PhysRevC.90.024912.
 150. M. Albright and J. I. Kapusta, Quasiparticle Theory of Transport Coefficients for Hadronic Matter at Finite Temperature and Baryon Density, *Phys. Rev. C* **93**(1), 014903 (2016). doi: 10.1103/PhysRevC.93.014903.
 151. S. Mitra and V. Chandra, Transport coefficients of a hot QCD medium and their relative significance in heavy-ion collisions, *Phys. Rev. D* **96**(9), 094003 (2017). doi: 10.1103/PhysRevD.96.094003.
 152. M. Greif, J. A. Fotakis, G. S. Denicol, and C. Greiner, Diffusion of conserved charges in relativistic heavy ion collisions, *Phys. Rev. Lett.* **120**(24), 242301 (2018). doi: 10.1103/PhysRevLett.120.242301.
 153. J. A. Fotakis, O. Soloveva, C. Greiner, O. Kaczmarek, and E. Bratkovskaya, Diffusion coefficient matrix of the strongly interacting quark-gluon plasma, *Phys. Rev. D* **104**(3), 034014 (2021). doi: 10.1103/PhysRevD.104.034014.
 154. P. Kovtun and A. Shukla, Kubo formulas for thermodynamic transport

- coefficients, *JHEP*. **10**, 007 (2018). doi: 10.1007/JHEP10(2018)007.
155. S. Jeon, Hydrodynamic transport coefficients in relativistic scalar field theory, *Phys. Rev. D*. **52**, 3591–3642 (1995). doi: 10.1103/PhysRevD.52.3591.
 156. M. E. Carrington, D.-f. Hou, and R. Kobes, Shear viscosity in ϕ^4 theory from an extended ladder resummation, *Phys. Rev. D*. **62**, 025010 (2000). doi: 10.1103/PhysRevD.62.025010.
 157. G. D. Moore and O. Saremi, Bulk viscosity and spectral functions in QCD, *JHEP*. **09**, 015 (2008). doi: 10.1088/1126-6708/2008/09/015.
 158. J.-B. Rose, M. Greif, J. Hammelmann, J. A. Fotakis, G. S. Denicol, H. Elfner, and C. Greiner, Cross-conductivity: novel transport coefficients to constrain the hadronic degrees of freedom of nuclear matter, *Phys. Rev. D*. **101**(11), 114028 (2020). doi: 10.1103/PhysRevD.101.114028.
 159. J. Hammelmann, J. Staudenmaier, and H. Elfner, Collision term dependence of the hadronic shear viscosity and diffusion coefficients (7, 2023).
 160. H. B. Meyer, Transport Properties of the Quark-Gluon Plasma: A Lattice QCD Perspective, *Eur. Phys. J. A*. **47**, 86 (2011). doi: 10.1140/epja/i2011-11086-3.
 161. H.-T. Ding, F. Karsch, and S. Mukherjee, Thermodynamics of strong-interaction matter from Lattice QCD, *Int. J. Mod. Phys. E*. **24**(10), 1530007 (2015). doi: 10.1142/S0218301315300076.
 162. O. Kaczmarek and H.-T. Shu, Spectral and Transport Properties from Lattice QCD, *Lect. Notes Phys.* **999**, 307–345 (2022). doi: 10.1007/978-3-030-95491-8_8.
 163. G. Aarts et al., Phase Transitions in Particle Physics: Results and Perspectives from Lattice Quantum Chromo-Dynamics, *Prog. Part. Nucl. Phys.* **133**, 104070 (2023). doi: 10.1016/j.pnpnp.2023.104070.
 164. R. Rougemont, J. Grefa, M. Hippert, J. Noronha, J. Noronha-Hostler, I. Portillo, and C. Ratti, Hot QCD phase diagram from holographic Einstein–Maxwell–Dilaton models, *Prog. Part. Nucl. Phys.* **135**, 104093 (2024). doi: 10.1016/j.pnpnp.2023.104093.
 165. P. Kovtun, D. T. Son, and A. O. Starinets, Viscosity in strongly interacting quantum field theories from black hole physics, *Phys. Rev. Lett.* **94**, 111601 (2005). doi: 10.1103/PhysRevLett.94.111601.
 166. G. Policastro, D. T. Son, and A. O. Starinets, The Shear viscosity of strongly coupled N=4 supersymmetric Yang-Mills plasma, *Phys. Rev. Lett.* **87**, 081601 (2001). doi: 10.1103/PhysRevLett.87.081601.
 167. A. Buchel, Bulk viscosity of gauge theory plasma at strong coupling, *Phys. Lett. B*. **663**, 286–289 (2008). doi: 10.1016/j.physletb.2008.03.069.
 168. A. Buchel and S. Cremonini, Viscosity Bound and Causality in Superfluid Plasma, *JHEP*. **10**, 026 (2010). doi: 10.1007/JHEP10(2010)026.
 169. S. Cremonini, U. Gursoy, and P. Szepietowski, On the Temperature Dependence of the Shear Viscosity and Holography, *JHEP*. **08**, 167 (2012). doi: 10.1007/JHEP08(2012)167.
 170. D. Li, S. He, and M. Huang, Temperature dependent transport coefficients in a dynamical holographic QCD model, *JHEP*. **06**, 046 (2015). doi: 10.1007/JHEP06(2015)046.

171. S. I. Finazzo, R. Rougemont, H. Marrochio, and J. Noronha, Hydrodynamic transport coefficients for the non-conformal quark-gluon plasma from holography, *JHEP*. **02**, 051 (2015). doi: 10.1007/JHEP02(2015)051.
172. R. Rougemont, J. Noronha, and J. Noronha-Hostler, Suppression of baryon diffusion and transport in a baryon rich strongly coupled quark-gluon plasma, *Phys. Rev. Lett.* **115**(20), 202301 (2015). doi: 10.1103/PhysRevLett.115.202301.
173. R. Rougemont, R. Critelli, J. Noronha-Hostler, J. Noronha, and C. Ratti, Dynamical versus equilibrium properties of the QCD phase transition: A holographic perspective, *Phys. Rev. D*. **96**(1), 014032 (2017). doi: 10.1103/PhysRevD.96.014032.
174. J. Casalderrey-Solana, H. Liu, D. Mateos, K. Rajagopal, and U. A. Wiedemann, *Gauge/String Duality, Hot QCD and Heavy Ion Collisions*. Cambridge University Press (2014). ISBN 978-1-00-940350-4, 978-1-00-940349-8, 978-1-00-940352-8, 978-1-139-13674-7. doi: 10.1017/9781009403504.
175. S. Cremonini, The Shear Viscosity to Entropy Ratio: A Status Report, *Mod. Phys. Lett. B*. **25**, 1867–1888 (2011). doi: 10.1142/S0217984911027315.
176. P. Romatschke and U. Romatschke, Viscosity Information from Relativistic Nuclear Collisions: How Perfect is the Fluid Observed at RHIC?, *Phys. Rev. Lett.* **99**, 172301 (2007). doi: 10.1103/PhysRevLett.99.172301.
177. H. Song and U. W. Heinz, Suppression of elliptic flow in a minimally viscous quark-gluon plasma, *Phys. Lett. B*. **658**, 279–283 (2008). doi: 10.1016/j.physletb.2007.11.019.
178. G. S. Denicol, T. Kodama, T. Koide, and P. Mota, Effect of bulk viscosity on Elliptic Flow near QCD phase transition, *Phys. Rev. C*. **80**, 064901 (2009). doi: 10.1103/PhysRevC.80.064901.
179. C. Gale, S. Jeon, B. Schenke, P. Tribedy, and R. Venugopalan, Event-by-event anisotropic flow in heavy-ion collisions from combined Yang-Mills and viscous fluid dynamics, *Phys. Rev. Lett.* **110**(1), 012302 (2013). doi: 10.1103/PhysRevLett.110.012302.
180. U. Heinz and R. Snellings, Collective flow and viscosity in relativistic heavy-ion collisions, *Ann. Rev. Nucl. Part. Sci.* **63**, 123–151 (2013). doi: 10.1146/annurev-nucl-102212-170540.
181. G. Denicol, A. Monnai, and B. Schenke, Moving forward to constrain the shear viscosity of QCD matter, *Phys. Rev. Lett.* **116**(21), 212301 (2016). doi: 10.1103/PhysRevLett.116.212301.
182. H. Niemi, K. J. Eskola, and R. Paatelainen, Event-by-event fluctuations in a perturbative QCD + saturation + hydrodynamics model: Determining QCD matter shear viscosity in ultrarelativistic heavy-ion collisions, *Phys. Rev. C*. **93**(2), 024907 (2016). doi: 10.1103/PhysRevC.93.024907.
183. S. Ryu, J. F. Paquet, C. Shen, G. S. Denicol, B. Schenke, S. Jeon, and C. Gale, Importance of the Bulk Viscosity of QCD in Ultrarelativistic Heavy-Ion Collisions, *Phys. Rev. Lett.* **115**(13), 132301 (2015). doi: 10.1103/PhysRevLett.115.132301.
184. S. Ryu, J.-F. Paquet, C. Shen, G. Denicol, B. Schenke, S. Jeon, and C. Gale, Effects of bulk viscosity and hadronic rescattering in heavy ion collisions at

- energies available at the BNL Relativistic Heavy Ion Collider and at the CERN Large Hadron Collider, *Phys. Rev. C* **97**(3), 034910 (2018). doi: 10.1103/PhysRevC.97.034910.
185. L. P. Csernai, J. I. Kapusta, and L. D. McLerran, On the Strongly-Interacting Low-Viscosity Matter Created in Relativistic Nuclear Collisions, *Phys. Rev. Lett.* **97**, 152303 (2006). doi: 10.1103/PhysRevLett.97.152303.
 186. D. Kharzeev and K. Tuchin, Bulk viscosity of QCD matter near the critical temperature, *JHEP*. **09**, 093 (2008). doi: 10.1088/1126-6708/2008/09/093.
 187. F. Karsch, D. Kharzeev, and K. Tuchin, Universal properties of bulk viscosity near the QCD phase transition, *Phys. Lett. B*. **663**, 217–221 (2008). doi: 10.1016/j.physletb.2008.01.080.
 188. J. Noronha-Hostler, J. Noronha, and C. Greiner, Transport Coefficients of Hadronic Matter near $T(c)$, *Phys. Rev. Lett.* **103**, 172302 (2009). doi: 10.1103/PhysRevLett.103.172302.
 189. P. B. Arnold, C. Dogan, and G. D. Moore, The Bulk Viscosity of High-Temperature QCD, *Phys. Rev. D*. **74**, 085021 (2006). doi: 10.1103/PhysRevD.74.085021.
 190. J. Novak, K. Novak, S. Pratt, J. Vredevoogd, C. Coleman-Smith, and R. Wolpert, Determining Fundamental Properties of Matter Created in Ultrarelativistic Heavy-Ion Collisions, *Phys. Rev. C*. **89**(3), 034917 (2014). doi: 10.1103/PhysRevC.89.034917.
 191. S. Pratt, E. Sangaline, P. Sorensen, and H. Wang, Constraining the Eq. of State of Super-Hadronic Matter from Heavy-Ion Collisions, *Phys. Rev. Lett.* **114**, 202301 (2015). doi: 10.1103/PhysRevLett.114.202301.
 192. J. E. Bernhard, P. W. Marcy, C. E. Coleman-Smith, S. Huzurbazar, R. L. Wolpert, and S. A. Bass, Quantifying properties of hot and dense QCD matter through systematic model-to-data comparison, *Phys. Rev. C*. **91**(5), 054910 (2015). doi: 10.1103/PhysRevC.91.054910.
 193. J. E. Bernhard, J. S. Moreland, S. A. Bass, J. Liu, and U. Heinz, Applying Bayesian parameter estimation to relativistic heavy-ion collisions: simultaneous characterization of the initial state and quark-gluon plasma medium, *Phys. Rev. C*. **94**(2), 024907 (2016). doi: 10.1103/PhysRevC.94.024907.
 194. J. S. Moreland, J. E. Bernhard, and S. A. Bass, Bayesian calibration of a hybrid nuclear collision model using p-Pb and Pb-Pb data at energies available at the CERN Large Hadron Collider, *Phys. Rev. C*. **101**(2), 024911 (2020). doi: 10.1103/PhysRevC.101.024911.
 195. J. E. Bernhard, J. S. Moreland, and S. A. Bass, Bayesian estimation of the specific shear and bulk viscosity of quark-gluon plasma, *Nature Phys.* **15**(11), 1113–1117 (2019). doi: 10.1038/s41567-019-0611-8.
 196. J. E. Parkkila, A. Onnerstad, and D. J. Kim, Bayesian estimation of the specific shear and bulk viscosity of the quark-gluon plasma with additional flow harmonic observables, *Phys. Rev. C*. **104**(5), 054904 (2021). doi: 10.1103/PhysRevC.104.054904.
 197. J. E. Parkkila, A. Onnerstad, S. F. Taghavi, C. Mordasini, A. Bilandzic, M. Virta, and D. J. Kim, New constraints for QCD matter from improved Bayesian parameter estimation in heavy-ion collisions at LHC, *Phys. Lett.*

- B.* **835**, 137485 (2022). doi: 10.1016/j.physletb.2022.137485.
198. M. R. Heffernan, C. Gale, S. Jeon, and J.-F. Paquet, Early-times Yang-Mills dynamics and the characterization of strongly interacting matter with statistical learning (6, 2023).
 199. M. R. Heffernan, C. Gale, S. Jeon, and J.-F. Paquet, Bayesian quantification of strongly-interacting matter with color glass condensate initial conditions (2, 2023).
 200. D. Liyanage, O. Sürer, M. Plumlee, S. M. Wild, and U. Heinz, Bayesian calibration of viscous anisotropic hydrodynamic simulations of heavy-ion collisions, *Phys. Rev. C.* **108**(5), 054905 (2023). doi: 10.1103/PhysRevC.108.054905.
 201. C. Shen and L. Yan, Recent development of hydrodynamic modeling in heavy-ion collisions, *Nucl. Sci. Tech.* **31**(12), 122 (10, 2020). doi: 10.1007/s41365-020-00829-z.
 202. J.-F. Paquet, Applications of emulation and Bayesian methods in heavy-ion physics (10, 2023).
 203. J. Liao and V. Koch, On the Fluidity and Super-Criticality of the QCD matter at RHIC, *Phys. Rev. C.* **81**, 014902 (2010). doi: 10.1103/PhysRevC.81.014902.
 204. G. S. Denicol, C. Gale, S. Jeon, and J. Noronha, Fluid behavior of a baryon-rich hadron resonance gas, *Phys. Rev. C.* **88**(6), 064901 (2013). doi: 10.1103/PhysRevC.88.064901.
 205. J. Auvinen, J. E. Bernhard, S. A. Bass, and I. Karpenko, Investigating the collision energy dependence of η/s in the beam energy scan at the BNL Relativistic Heavy Ion Collider using Bayesian statistics, *Phys. Rev. C.* **97**(4), 044905 (2018). doi: 10.1103/PhysRevC.97.044905.
 206. C. Shen, B. Schenke, and W. Zhao, Viscosities of the Baryon-Rich Quark-Gluon Plasma from Beam Energy Scan Data (10, 2023).
 207. Z. Yang, Y. Sun, and L.-W. Chen, Baryon density dependence of viscosities of the quark-gluon plasma at hadronization (10, 2023).
 208. C. Hoyos, N. Jokela, M. Jarvinen, J. G. Subils, J. Tarrío, and A. Vuorinen, Transport in strongly coupled quark matter, *Phys. Rev. Lett.* **125**, 241601 (2020). doi: 10.1103/PhysRevLett.125.241601.
 209. J. Grefa, M. Hippert, J. Noronha, J. Noronha-Hostler, I. Portillo, C. Ratti, and R. Rougemont, Transport coefficients of the quark-gluon plasma at the critical point and across the first-order line, *Phys. Rev. D.* **106**(3), 034024 (2022). doi: 10.1103/PhysRevD.106.034024.
 210. O. Soloveva, P. Moreau, and E. Bratkovskaya, Transport coefficients for the hot quark-gluon plasma at finite chemical potential μ_B , *Phys. Rev. C.* **101**(4), 045203 (2020). doi: 10.1103/PhysRevC.101.045203.
 211. O. Soloveva, D. Fuseau, J. Aichelin, and E. Bratkovskaya, Shear viscosity and electric conductivity of a hot and dense QGP with a chiral phase transition, *Phys. Rev. C.* **103**(5), 054901 (2021). doi: 10.1103/PhysRevC.103.054901.
 212. J. B. Rose, J. M. Torres-Rincon, A. Schäfer, D. R. Oliinychenko, and H. Petersen, Shear viscosity of a hadron gas and influence of resonance

- lifetimes on relaxation time, *Phys. Rev. C* **97**(5), 055204 (2018). doi: 10.1103/PhysRevC.97.055204.
213. E. McLaughlin, J. Rose, T. Dore, P. Parotto, C. Ratti, and J. Noronha-Hostler, Building a testable shear viscosity across the QCD phase diagram, *Phys. Rev. C* **105**(2), 024903 (2022). doi: 10.1103/PhysRevC.105.024903.
214. S. Mitra and V. Chandra, Thermal relaxation, electrical conductivity, and charge diffusion in a hot QCD medium, *Phys. Rev. D* **94**(3), 034025 (2016). doi: 10.1103/PhysRevD.94.034025.
215. M. Li and C. Shen, Longitudinal Dynamics of High Baryon Density Matter in High Energy Heavy-Ion Collisions, *Phys. Rev. C* **98**(6), 064908 (2018). doi: 10.1103/PhysRevC.98.064908.
216. X.-Y. Wu, C. Yi, G.-Y. Qin, and S. Pu, Local and global polarization of Λ hyperons across RHIC-BES energies: The roles of spin hall effect, initial condition, and baryon diffusion, *Phys. Rev. C* **105**(6), 064909 (2022). doi: 10.1103/PhysRevC.105.064909.
217. J. I. Kapusta and C. Plumberg, Causal Electric Charge Diffusion and Balance Functions in Relativistic Heavy Ion Collisions, *Phys. Rev. C* **97**(1), 014906 (2018). doi: 10.1103/PhysRevC.97.014906. [Erratum: *Phys. Rev. C* **102**, 019901 (2020)].
218. S. Pratt and C. Plumberg, Determining the Diffusivity for Light Quarks from Experiment, *Phys. Rev. C* **102**(4), 044909 (2020). doi: 10.1103/PhysRevC.102.044909.
219. A. De, C. Plumberg, and J. I. Kapusta, Calculating Fluctuations and Self-Correlations Numerically for Causal Charge Diffusion in Relativistic Heavy-Ion Collisions, *Phys. Rev. C* **102**(2), 024905 (2020). doi: 10.1103/PhysRevC.102.024905.
220. S. Pratt and C. Plumberg, Charge balance functions for heavy-ion collisions at energies available at the CERN Large Hadron Collider, *Phys. Rev. C* **104**(1), 014906 (2021). doi: 10.1103/PhysRevC.104.014906.
221. G. Baym, T. Hatsuda, T. Kojo, P. D. Powell, Y. Song, and T. Takatsuka, From hadrons to quarks in neutron stars: a review, *Rept. Prog. Phys.* **81**(5), 056902 (2018). doi: 10.1088/1361-6633/aaae14.
222. A. Sorensen et al., Dense nuclear matter equation of state from heavy-ion collisions, *Prog. Part. Nucl. Phys.* **134**, 104080 (2024). doi: 10.1016/j.pnpnp.2023.104080.
223. M. Bluhm, B. Kampfer, R. Schulze, D. Seipt, and U. Heinz, A family of equations of state based on lattice QCD: Impact on flow in ultrarelativistic heavy-ion collisions, *Phys. Rev. C* **76**, 034901 (2007). doi: 10.1103/PhysRevC.76.034901.
224. P. Huovinen and P. Petreczky, QCD Equation of State and Hadron Resonance Gas, *Nucl. Phys. A* **837**, 26–53 (2010). doi: 10.1016/j.nuclphysa.2010.02.015.
225. A. Monnai, B. Schenke, and C. Shen, QCD Equation of State at Finite Chemical Potentials for Relativistic Nuclear Collisions, *Int. J. Mod. Phys. A* **36**(07), 2130007 (2021). doi: 10.1142/S0217751X21300076.
226. O. Philipsen, The QCD equation of state from the lattice, *Prog. Part. Nucl.*

- Phys.* **70**, 55–107 (2013). doi: 10.1016/j.pnpnp.2012.09.003.
227. A. Bazavov et al., Skewness, kurtosis, and the fifth and sixth order cumulants of net baryon-number distributions from lattice QCD confront high-statistics STAR data, *Phys. Rev. D.* **101**(7), 074502 (2020). doi: 10.1103/PhysRevD.101.074502.
228. A. Bazavov et al., Fluctuations and Correlations of net baryon number, electric charge, and strangeness: A comparison of lattice QCD results with the hadron resonance gas model, *Phys. Rev. D.* **86**, 034509 (2012). doi: 10.1103/PhysRevD.86.034509.
229. S. Borsanyi, G. Endrodi, Z. Fodor, S. D. Katz, S. Krieg, C. Ratti, and K. K. Szabo, QCD equation of state at nonzero chemical potential: continuum results with physical quark masses at order mu^2 , *JHEP.* **08**, 053 (2012). doi: 10.1007/JHEP08(2012)053.
230. S. Borsányi, Z. Fodor, J. N. Guenther, R. Kara, S. D. Katz, P. Parotto, A. Pásztor, C. Ratti, and K. K. Szabó, Lattice QCD equation of state at finite chemical potential from an alternative expansion scheme, *Phys. Rev. Lett.* **126**(23), 232001 (2021). doi: 10.1103/PhysRevLett.126.232001.
231. R. A. Soltz, C. DeTar, F. Karsch, S. Mukherjee, and P. Vranas, Lattice QCD Thermodynamics with Physical Quark Masses, *Ann. Rev. Nucl. Part. Sci.* **65**, 379–402 (2015). doi: 10.1146/annurev-nucl-102014-022157.
232. R. Critelli, J. Noronha, J. Noronha-Hostler, I. Portillo, C. Ratti, and R. Rougemont, Critical point in the phase diagram of primordial quark-gluon matter from black hole physics, *Phys. Rev. D.* **96**(9), 096026 (2017). doi: 10.1103/PhysRevD.96.096026.
233. J. Noronha-Hostler, P. Parotto, C. Ratti, and J. M. Stafford, Lattice-based equation of state at finite baryon number, electric charge and strangeness chemical potentials, *Phys. Rev. C.* **100**(6), 064910 (2019). doi: 10.1103/PhysRevC.100.064910.
234. A. Monnai, B. Schenke, and C. Shen, Equation of state at finite densities for QCD matter in nuclear collisions, *Phys. Rev. C.* **100**(2), 024907 (2019). doi: 10.1103/PhysRevC.100.024907.
235. S. Borsanyi, Z. Fodor, S. D. Katz, S. Krieg, C. Ratti, and K. Szabo, Fluctuations of conserved charges at finite temperature from lattice QCD, *JHEP.* **01**, 138 (2012). doi: 10.1007/JHEP01(2012)138.
236. V. Vovchenko, M. I. Gorenstein, and H. Stoecker, van der Waals Interactions in Hadron Resonance Gas: From Nuclear Matter to Lattice QCD, *Phys. Rev. Lett.* **118**(18), 182301 (2017). doi: 10.1103/PhysRevLett.118.182301.
237. V. Vovchenko, Hadron resonance gas with van der Waals interactions, *Int. J. Mod. Phys. E.* **29**(05), 2040002 (2020). doi: 10.1142/S0218301320400029.
238. P. Alba, V. Mantovani Sarti, J. Noronha, J. Noronha-Hostler, P. Parotto, I. Portillo Vazquez, and C. Ratti, Effect of the QCD equation of state and strange hadronic resonances on multiparticle correlations in heavy ion collisions, *Phys. Rev. C.* **98**(3), 034909 (2018). doi: 10.1103/PhysRevC.98.034909.
239. L. Du, Bulk medium properties of heavy-ion collisions at beam energy scan with a multistage hydrodynamic model (12, 2023).

240. J. Auvinen, K. J. Eskola, P. Huovinen, H. Niemi, R. Paatelainen, and P. Petreczky, Temperature dependence of η/s of strongly interacting matter: Effects of the equation of state and the parametric form of $(\eta/s)(T)$, *Phys. Rev. C* **102**(4), 044911 (2020). doi: 10.1103/PhysRevC.102.044911.
241. J. Steinheimer, A. Motornenko, A. Sorensen, Y. Nara, V. Koch, and M. Bleicher, The high-density equation of state in heavy-ion collisions: constraints from proton flow, *Eur. Phys. J. C* **82**(10), 911 (2022). doi: 10.1140/epjc/s10052-022-10894-w.
242. J. S. Moreland and R. A. Soltz, Hydrodynamic simulations of relativistic heavy-ion collisions with different lattice quantum chromodynamics calculations of the equation of state, *Phys. Rev. C* **93**(4), 044913 (2016). doi: 10.1103/PhysRevC.93.044913.
243. D. Oliinychenko, A. Sorensen, V. Koch, and L. McLerran, Sensitivity of Au+Au collisions to the symmetric nuclear matter equation of state at 2–5 nuclear saturation densities, *Phys. Rev. C* **108**(3), 034908 (2023). doi: 10.1103/PhysRevC.108.034908.
244. M. Omana Kuttan, J. Steinheimer, K. Zhou, and H. Stoecker, QCD Equation of State of Dense Nuclear Matter from a Bayesian Analysis of Heavy-Ion Collision Data, *Phys. Rev. Lett.* **131**(20), 202303 (2023). doi: 10.1103/PhysRevLett.131.202303.
245. L.-G. Pang, K. Zhou, N. Su, H. Petersen, H. Stöcker, and X.-N. Wang, An equation-of-state-meter of quantum chromodynamics transition from deep learning, *Nature Commun.* **9**(1), 210 (2018). doi: 10.1038/s41467-017-02726-3.
246. R. Wang, Y.-G. Ma, R. Wada, L.-W. Chen, W.-B. He, H.-L. Liu, and K.-J. Sun, Nuclear liquid-gas phase transition with machine learning, *Phys. Rev. Res.* **2**(4), 043202 (2020). doi: 10.1103/PhysRevResearch.2.043202.
247. K. Zhou, L. Wang, L.-G. Pang, and S. Shi, Exploring QCD matter in extreme conditions with Machine Learning, *Prog. Part. Nucl. Phys.* **104084**, 2023 (3, 2023). doi: 10.1016/j.ppnp.2023.104084.
248. R. Guida and J. Zinn-Justin, 3-D Ising model: The scaling equation of state, *Nucl. Phys. B* **489**, 626–652 (1997). doi: 10.1016/S0550-3213(96)00704-3.
249. C. Nonaka and M. Asakawa, Hydrodynamical evolution near the QCD critical end point, *Phys. Rev. C* **71**, 044904 (2005). doi: 10.1103/PhysRevC.71.044904.
250. P. Parotto, M. Bluhm, D. Mroczek, M. Nahrgang, J. Noronha-Hostler, K. Rajagopal, C. Ratti, T. Schäfer, and M. Stephanov, QCD equation of state matched to lattice data and exhibiting a critical point singularity, *Phys. Rev. C* **101**(3), 034901 (2020). doi: 10.1103/PhysRevC.101.034901.
251. J. M. Karthein, D. Mroczek, A. R. Nava Acuna, J. Noronha-Hostler, P. Parotto, D. R. P. Price, and C. Ratti, Strangeness-neutral equation of state for QCD with a critical point, *Eur. Phys. J. Plus.* **136**(6), 621 (2021). doi: 10.1140/epjp/s13360-021-01615-5.
252. M. S. Pradeep and M. Stephanov, Universality of the critical point mapping between Ising model and QCD at small quark mass, *Phys. Rev. D* **100**(5), 056003 (2019). doi: 10.1103/PhysRevD.100.056003.

253. J. I. Kapusta and T. Welle, Extending a scaling equation of state to QCD, *Phys. Rev. C* **106**(4), 044901 (2022). doi: 10.1103/PhysRevC.106.044901.
254. T. Dore, J. Noronha-Hostler, and E. McLaughlin, Far-from-equilibrium search for the QCD critical point, *Phys. Rev. D* **102**(7), 074017 (2020). doi: 10.1103/PhysRevD.102.074017.
255. S. Ahmad, H. Holopainen, and P. Huovinen, Dynamical freeze-out criterion in a hydrodynamical description of Au + Au collisions at $\sqrt{s_{\text{NN}}} = 200$ GeV and Pb + Pb collisions at $\sqrt{s_{\text{NN}}} = 2760$ GeV, *Phys. Rev. C* **95**(5), 054911 (2017). doi: 10.1103/PhysRevC.95.054911.
256. P. Huovinen and H. Petersen, Particlization in hybrid models, *Eur. Phys. J. A* **48**, 171 (2012). doi: 10.1140/epja/i2012-12171-9.
257. F. Cooper and G. Frye, Single Particle Distribution in the Hydrodynamic and Statistical Thermodynamic Models of Multiparticle Production, *Phys. Rev. D* **10**, 186 (1974). doi: 10.1103/PhysRevD.10.186.
258. F. Cooper, G. Frye, and E. Schonberg, Landau's hydrodynamic model of particle production and electron-positron annihilation into hadrons, *Phys. Rev. D* **11**, 192–213 (Jan, 1975). doi: 10.1103/PhysRevD.11.192.
259. H. Grad, On the kinetic theory of rarefied gases, *Commun. Pure Appl. Math.* **2**(4), 331–407 (1949). doi: 10.1002/cpa.3160020403.
260. D. Teaney, The Effects of viscosity on spectra, elliptic flow, and HBT radii, *Phys. Rev. C* **68**, 034913 (2003). doi: 10.1103/PhysRevC.68.034913.
261. J. L. Anderson and H. R. Witting, A relativistic relaxation-time model for the Boltzmann equation, *Physica* **74**(3), 466–488 (1974). doi: 10.1016/0031-8914(74)90355-3.
262. A. Jaiswal, R. Ryblewski, and M. Strickland, Transport coefficients for bulk viscous evolution in the relaxation time approximation, *Phys. Rev. C* **90**(4), 044908 (2014). doi: 10.1103/PhysRevC.90.044908.
263. S. Pratt and G. Torrieri, Coupling Relativistic Viscous Hydrodynamics to Boltzmann Descriptions, *Phys. Rev. C* **82**, 044901 (2010). doi: 10.1103/PhysRevC.82.044901.
264. M. McNelis, D. Everett, and U. Heinz, Particlization in fluid dynamical simulations of heavy-ion collisions: The iS3D module, *Comput. Phys. Commun.* **258**, 107604 (2021). doi: 10.1016/j.cpc.2020.107604.
265. M. McNelis and U. Heinz, Modified equilibrium distributions for Cooper–Frye particlization, *Phys. Rev. C* **103**(6), 064903 (2021). doi: 10.1103/PhysRevC.103.064903.
266. S. Pratt, Accounting for backflow in hydrodynamic-Boltzmann interfaces, *Phys. Rev. C* **89**(2), 024910 (2014). doi: 10.1103/PhysRevC.89.024910.
267. S. Pratt and J. Vredevoogd, Femtoscopy in Relativistic Heavy Ion Collisions and its Relation to Bulk Properties of QCD Matter, *Phys. Rev. C* **78**, 054906 (2008). doi: 10.1103/PhysRevC.79.069901. [Erratum: *Phys. Rev. C* **79**, 069901 (2009)].
268. D. Oliinychenko, P. Huovinen, and H. Petersen, Systematic Investigation of Negative Cooper-Frye Contributions in Heavy Ion Collisions Using Coarse-grained Molecular Dynamics, *Phys. Rev. C* **91**(2), 024906 (2015). doi: 10.1103/PhysRevC.91.024906.

269. D. Oliinychenko, S. Shi, and V. Koch, Effects of local event-by-event conservation laws in ultrarelativistic heavy-ion collisions at particlization, *Phys. Rev. C* **102**(3), 034904 (2020). doi: 10.1103/PhysRevC.102.034904.
270. A. Kisiel, T. Taluc, W. Broniowski, and W. Florkowski, THERMINATOR: THERMal heavy-IoN generATOR, *Comput. Phys. Commun.* **174**, 669–687 (2006). doi: 10.1016/j.cpc.2005.11.010.
271. C. Shen, Z. Qiu, H. Song, J. Bernhard, S. Bass, and U. Heinz, The iEBE-VISHNU code package for relativistic heavy-ion collisions, *Comput. Phys. Commun.* **199**, 61–85 (2016). doi: 10.1016/j.cpc.2015.08.039.
272. D. Oliinychenko and V. Koch, Microcanonical Particlization with Local Conservation Laws, *Phys. Rev. Lett.* **123**(18), 182302 (2019). doi: 10.1103/PhysRevLett.123.182302.
273. V. Vovchenko, Cooper-Frye sampling with short-range repulsion, *Phys. Rev. C* **106**(6), 064906 (2022). doi: 10.1103/PhysRevC.106.064906.
274. C. Schwarz, D. Oliinychenko, L. G. Pang, S. Ryu, and H. Petersen, Different realizations of Cooper–Frye sampling with conservation laws, *J. Phys. G* **45**(1), 015001 (2018). doi: 10.1088/1361-6471/aa90eb.
275. D. Oliinychenko and H. Petersen, Forced canonical thermalization in a hadronic transport approach at high density, *J. Phys. G* **44**(3), 034001 (2017). doi: 10.1088/1361-6471/aa528c.
276. J. Steinheimer and V. Koch, Effect of finite particle number sampling on baryon number fluctuations, *Phys. Rev. C* **96**(3), 034907 (2017). doi: 10.1103/PhysRevC.96.034907.
277. V. Vovchenko and V. Koch, Particlization of an interacting hadron resonance gas with global conservation laws for event-by-event fluctuations in heavy-ion collisions, *Phys. Rev. C* **103**(4), 044903 (2021). doi: 10.1103/PhysRevC.103.044903.
278. J. B. Rose, J. M. Torres-Rincon, and H. Elfner, Inclusive and effective bulk viscosities in the hadron gas, *J. Phys. G* **48**(1), 015005 (2020). doi: 10.1088/1361-6471/abbc5c.
279. K. Adcox et al., Formation of dense partonic matter in relativistic nucleus-nucleus collisions at RHIC: Experimental evaluation by the PHENIX collaboration, *Nucl. Phys. A* **757**, 184–283 (2005). doi: 10.1016/j.nuclphysa.2005.03.086.
280. D. Teaney, J. Lauret, and E. V. Shuryak, Flow at the SPS and RHIC as a quark gluon plasma signature, *Phys. Rev. Lett.* **86**, 4783–4786 (2001). doi: 10.1103/PhysRevLett.86.4783.
281. P. Huovinen, P. F. Kolb, U. W. Heinz, P. V. Ruuskanen, and S. A. Voloshin, Radial and elliptic flow at RHIC: Further predictions, *Phys. Lett. B* **503**, 58–64 (2001). doi: 10.1016/S0370-2693(01)00219-2.
282. P. F. Kolb and R. Rapp, Transverse flow and hadrochemistry in Au+Au collisions at $\sqrt{s_{NN}} = 200$ -GeV, *Phys. Rev. C* **67**, 044903 (2003). doi: 10.1103/PhysRevC.67.044903.
283. T. Hirano and Y. Nara, Hydrodynamic afterburner for the color glass condensate and the parton energy loss, *Nucl. Phys. A* **743**, 305–328 (2004). doi: 10.1016/j.nuclphysa.2004.08.003.

284. P. Sorensen, *Elliptic Flow: A Study of Space-Momentum Correlations In Relativistic Nuclear Collisions*, In eds. R. C. Hwa and X.-N. Wang, *Quark-gluon plasma 4*, pp. 323–374. (2010). doi: 10.1142/9789814293297_0006.
285. J. Adams et al., Experimental and theoretical challenges in the search for the quark gluon plasma: The STAR Collaboration’s critical assessment of the evidence from RHIC collisions, *Nucl. Phys. A.* **757**, 102–183 (2005). doi: 10.1016/j.nuclphysa.2005.03.085.
286. B. Abelev et al., Centrality dependence of π , K, p production in Pb-Pb collisions at $\sqrt{s_{NN}} = 2.76$ TeV, *Phys. Rev. C.* **88**, 044910 (2013). doi: 10.1103/PhysRevC.88.044910.
287. S. S. Adler et al., Identified charged particle spectra and yields in Au+Au collisions at $\sqrt{s_{NN}} = 200$ -GeV, *Phys. Rev. C.* **69**, 034909 (2004). doi: 10.1103/PhysRevC.69.034909.
288. H. Elfner and B. Müller, The exploration of hot and dense nuclear matter: introduction to relativistic heavy-ion physics, *J. Phys. G.* **50**(10), 103001 (2023). doi: 10.1088/1361-6471/ace824.
289. J. Adams et al., Azimuthal anisotropy in Au+Au collisions at $\sqrt{s_{NN}} = 200$ -GeV, *Phys. Rev. C.* **72**, 014904 (2005). doi: 10.1103/PhysRevC.72.014904.
290. J. Steinheimer, J. Aichelin, and M. Bleicher, Nonthermal p/ π Ratio at LHC as a Consequence of Hadronic Final State Interactions, *Phys. Rev. Lett.* **110**(4), 042501 (2013). doi: 10.1103/PhysRevLett.110.042501.
291. J. Hammelmann and H. Elfner, Impact of hadronic interactions and conservation laws on cumulants of conserved charges in a dynamical model, *Phys. Rev. C.* **107**(4), 044910 (2023). doi: 10.1103/PhysRevC.107.044910.
292. J. Hammelmann, M. Bluhm, M. Nohrang, and H. Elfner, Fate of critical fluctuations in an interacting hadronic medium using maximum entropy distributions (10, 2023).
293. O. Savchuk, R. V. Poberezhnyuk, A. Motornenko, J. Steinheimer, M. I. Gorenstein, and V. Vovchenko, Phase transition amplification of proton number fluctuations in nuclear collisions from a transport model approach, *Phys. Rev. C.* **107**(2), 024913 (2023). doi: 10.1103/PhysRevC.107.024913.
294. G. Baym, RHIC: From dreams to beams in two decades, *Nucl. Phys. A.* **698**, XXIII–XXXII (2002). doi: 10.1016/S0375-9474(01)01342-2.
295. L. Lederman and J. Weneser, *Report of the Workshop on BEV/NUCLEON COLLISIONS OF HEAVY IONS — HOW AND WHY*. Brookhaven National Laboratory, Associated Universities, Inc. (1974). Accessed: 2024-01-31.
296. D. J. Gross and F. Wilczek, Ultraviolet Behavior of Nonabelian Gauge Theories, *Phys. Rev. Lett.* **30**, 1343–1346 (1973). doi: 10.1103/PhysRevLett.30.1343.
297. H. D. Politzer, Reliable Perturbative Results for Strong Interactions?, *Phys. Rev. Lett.* **30**, 1346–1349 (1973). doi: 10.1103/PhysRevLett.30.1346.
298. J. C. Collins and M. J. Perry, Superdense Matter: Neutrons Or Asymptotically Free Quarks?, *Phys. Rev. Lett.* **34**, 1353 (1975). doi: 10.1103/PhysRevLett.34.1353.
299. G. Chapline, Jr. and M. Nauenberg, Phase Transition from Baryon to Quark

- Matter, *Nature*. **264**, 235–236 (1976). doi: 10.1038/264235a0.
300. G. F. Chapline, M. H. Johnson, E. Teller, and M. S. Weiss, Highly excited nuclear matter, *Phys. Rev. D*. **8**, 4302–4308 (1973). doi: 10.1103/PhysRevD.8.4302.
 301. R. Hagedorn, Statistical thermodynamics of strong interactions at high-energies, *Nuovo Cim. Suppl.* **3**, 147–186 (1965).
 302. N. Cabibbo and G. Parisi, Exponential Hadronic Spectrum and Quark Liberation, *Phys. Lett. B*. **59**, 67–69 (1975). doi: 10.1016/0370-2693(75)90158-6.
 303. G. F. Chapline and A. K. Kerman, On the Possibility of Making Quark Matter in Nuclear Collisions (1978).
 304. S. A. Chin, Transition to Hot Quark Matter in Relativistic Heavy Ion Collision, *Phys. Lett. B*. **78**, 552–555 (1978). doi: 10.1016/0370-2693(78)90637-8.
 305. E. V. Shuryak, Theory of Hadronic Plasma, *Sov. Phys. JETP*. **47**, 212–219 (1978).
 306. E. V. Shuryak, Quark-Gluon Plasma and Hadronic Production of Leptons, Photons and Psions, *Phys. Lett. B*. **78**, 150 (1978). doi: 10.1016/0370-2693(78)90370-2.
 307. E. Epelbaum, H.-W. Hammer, and U.-G. Meissner, Modern Theory of Nuclear Forces, *Rev. Mod. Phys.* **81**, 1773–1825 (2009). doi: 10.1103/RevModPhys.81.1773.
 308. R. Machleidt and D. R. Entem, Chiral effective field theory and nuclear forces, *Phys. Rept.* **503**, 1–75 (2011). doi: 10.1016/j.physrep.2011.02.001.
 309. C. Drischler, J. W. Holt, and C. Wellenhofer, Chiral Effective Field Theory and the High-Density Nuclear Equation of State, *Ann. Rev. Nucl. Part. Sci.* **71**, 403–432 (2021). doi: 10.1146/annurev-nucl-102419-041903.
 310. R. Kumar et al., Theoretical and Experimental Constraints for the Equation of State of Dense and Hot Matter (3, 2023).
 311. F. Özel and P. Freire, Masses, Radii, and the Equation of State of Neutron Stars, *Ann. Rev. Astron. Astrophys.* **54**, 401–440 (2016). doi: 10.1146/annurev-astro-081915-023322.
 312. I. Legred, K. Chatziioannou, R. Essick, S. Han, and P. Landry, Impact of the PSR J0740+6620 radius constraint on the properties of high-density matter, *Phys. Rev. D*. **104**(6), 063003 (2021). doi: 10.1103/PhysRevD.104.063003.
 313. M. C. Miller, C. Chirenti, and F. K. Lamb, Constraining the equation of state of high-density cold matter using nuclear and astronomical measurements (4, 2019). doi: 10.3847/1538-4357/ab4ef9.
 314. I. C. Arsene, L. V. Bravina, W. Cassing, Y. B. Ivanov, A. Larionov, J. Randrup, V. N. Russkikh, V. D. Toneev, G. Zeeb, and D. Zschesche, Dynamical phase trajectories for relativistic nuclear collisions, *Phys. Rev. C*. **75**, 034902 (2007). doi: 10.1103/PhysRevC.75.034902.
 315. FRIB Science Community. *FRIB400: The Scientific Case for the 400 MeV/u Energy Upgrade of FRIB*. https://frib.msu.edu/_files/pdfs/frib400_final.pdf (2019, updated February 2023). Accessed: 2023-07-16.
 316. X. G. Cao, G. Q. Zhang, X. Z. Cai, Y. G. Ma, W. Guo, J. G. Chen, W. D. Tian, D. Q. Fang, and H. W. Wang, The roles of deformation and orienta-

- tion in heavy-ion collisions induced by light deformed nuclei at intermediate energy, *Phys. Rev. C* **81**, 061603 (2010). doi: 10.1103/PhysRevC.81.061603.
317. B. Bally et al., Imaging the initial condition of heavy-ion collisions and nuclear structure across the nuclide chart (9, 2022).
318. E. Sangaline and S. Pratt, Toward a deeper understanding of how experiments constrain the underlying physics of heavy-ion collisions, *Phys. Rev. C* **93**(2), 024908 (2016). doi: 10.1103/PhysRevC.93.024908.
319. H. Wolter et al., Transport model comparison studies of intermediate-energy heavy-ion collisions, *Prog. Part. Nucl. Phys.* **125**, 103962 (2022). doi: 10.1016/j.pnpnp.2022.103962.
320. H. Stoecker, J. A. Maruhn, and W. Greiner, Collective sideward flow of nuclear matter in violent high-energy heavy ion collisions, *Phys. Rev. Lett.* **44**, 725 (1980). doi: 10.1103/PhysRevLett.44.725.
321. J.-Y. Ollitrault, Anisotropy as a signature of transverse collective flow, *Phys. Rev. D* **46**, 229–245 (1992). doi: 10.1103/PhysRevD.46.229.
322. D. H. Rischke, Y. Pürsün, J. A. Maruhn, H. Stoecker, and W. Greiner, The Phase transition to the quark - gluon plasma and its effects on hydrodynamic flow, *Acta Phys. Hung. A* **1**, 309–322 (1995). doi: 10.1007/BF03053749.
323. H. Stoecker, Collective flow signals the quark gluon plasma, *Nucl. Phys. A* **750**, 121–147 (2005). doi: 10.1016/j.nuclphysa.2004.12.074.
324. J. Brachmann, S. Soff, A. Dumitru, H. Stoecker, J. A. Maruhn, W. Greiner, L. V. Bravina, and D. H. Rischke, Antiflow of nucleons at the softest point of the EoS, *Phys. Rev. C* **61**, 024909 (2000). doi: 10.1103/PhysRevC.61.024909.
325. L. P. Csernai and D. Rohrlich, Third flow component as QGP signal, *Phys. Lett. B* **458**, 454 (1999). doi: 10.1016/S0370-2693(99)00615-2.
326. Y. B. Ivanov and A. A. Soldatov, Directed flow indicates a cross-over deconfinement transition in relativistic nuclear collisions, *Phys. Rev. C* **91**(2), 024915 (2015). doi: 10.1103/PhysRevC.91.024915.
327. C. Hartnack, J. Aichelin, H. Stoecker, and W. Greiner, Out of plane squeeze of clusters in relativistic heavy ion collisions, *Phys. Lett. B* **336**, 131–135 (1994). doi: 10.1016/0370-2693(94)90237-2.
328. B.-A. Li and C. M. Ko, Probing the softest region of nuclear equation of state, *Phys. Rev. C* **58**, R1382–R1384 (1998). doi: 10.1103/PhysRevC.58.R1382.
329. P. Danielewicz, R. Lacey, and W. G. Lynch, Determination of the equation of state of dense matter, *Science* **298**, 1592–1596 (2002). doi: 10.1126/science.1078070.
330. A. Le Fèvre, Y. Leifels, W. Reisdorf, J. Aichelin, and C. Hartnack, Constraining the nuclear matter equation of state around twice saturation density, *Nucl. Phys. A* **945**, 112–133 (2016). doi: 10.1016/j.nuclphysa.2015.09.015.
331. Y. Wang, C. Guo, Q. Li, A. Le Fèvre, Y. Leifels, and W. Trautmann, Determination of the nuclear incompressibility from the rapidity-dependent elliptic flow in heavy-ion collisions at beam energies 0.4 A –1.0 A GeV, *Phys. Lett. B* **778**, 207–212 (2018). doi: 10.1016/j.physletb.2018.01.035.

332. Y. Nara and A. Ohnishi, Mean-field update in the JAM microscopic transport model: Mean-field effects on collective flow in high-energy heavy-ion collisions at $\sqrt{s_{NN}}=2\text{--}20$ GeV energies, *Phys. Rev. C* **105**(1), 014911 (2022). doi: 10.1103/PhysRevC.105.014911.
333. S. A. Voloshin, A. M. Poskanzer, and R. Snellings, Collective phenomena in non-central nuclear collisions, *Landolt-Bornstein*. **23**, 293–333 (2010). doi: 10.1007/978-3-642-01539-7_10.
334. C. Zhang, J. Chen, X. Luo, F. Liu, and Y. Nara, Beam energy dependence of the squeeze-out effect on the directed and elliptic flow in Au + Au collisions in the high baryon density region, *Phys. Rev. C* **97**(6), 064913 (2018). doi: 10.1103/PhysRevC.97.064913.
335. J. Aichelin, A. Rosenhauer, G. Peilert, H. Stoecker, and W. Greiner, Importance of Momentum Dependent Interactions for the Extraction of the Nuclear Equation of State From High-energy Heavy Ion Collisions, *Phys. Rev. Lett.* **58**, 1926–1929 (1987). doi: 10.1103/PhysRevLett.58.1926.
336. Q.-b. Pan and P. Danielewicz, From sideward flow to nuclear compressibility, *Phys. Rev. Lett.* **70**, 2062–2065 (1993). doi: 10.1103/PhysRevLett.70.2062. [Erratum: *Phys. Rev. Lett.* **70**, 3523 (1993)].
337. P. Danielewicz, Determination of the mean field momentum dependence using elliptic flow, *Nucl. Phys. A*. **673**, 375–410 (2000). doi: 10.1016/S0375-9474(00)00083-X.
338. D. Persram and C. Gale, Elliptic flow in intermediate-energy heavy ion collisions and in-medium effects, *Phys. Rev. C* **65**, 064611 (2002). doi: 10.1103/PhysRevC.65.064611.
339. H. Muther and A. Polls, Two-body correlations in nuclear systems, *Prog. Part. Nucl. Phys.* **45**, 243–334 (2000). doi: 10.1016/S0146-6410(00)00105-8.
340. V. R. Pandharipande and S. C. Pieper, Nuclear transparency to intermediate-energy nucleons from (e, e'p) reactions, *Phys. Rev. C* **45**, 791–798 (1992). doi: 10.1103/PhysRevC.45.791.
341. B.-A. Li and L.-W. Chen, Nucleon-nucleon cross sections in neutron-rich matter and isospin transport in heavy-ion reactions at intermediate energies, *Phys. Rev. C* **72**, 064611 (2005). doi: 10.1103/PhysRevC.72.064611.
342. B. Chen, F. Sammarruca, and C. A. Bertulani, Microscopic in-medium nucleon-nucleon cross sections with improved Pauli blocking effects, *Phys. Rev. C* **87**(5), 054616 (2013). doi: 10.1103/PhysRevC.87.054616.
343. F. Sammarruca and P. Krastev, More on nucleon-nucleon cross sections in symmetric and asymmetric matter, *Phys. Rev. C* **73**, 014001 (2006). doi: 10.1103/PhysRevC.73.014001.
344. G. D. Westfall et al., Mass dependence of the disappearance of flow in nuclear collisions, *Phys. Rev. Lett.* **71**, 1986–1989 (1993). doi: 10.1103/PhysRevLett.71.1986.
345. Y. Zhang, Z. Li, and P. Danielewicz, In-medium NN cross-sections determined from stopping and collective flow in intermediate-energy heavy-ion collisions, *Phys. Rev. C* **75**, 034615 (2007). doi: 10.1103/PhysRevC.75.034615.
346. P. Li, Y. Wang, Q. Li, and H. Zhang, Accessing the in-medium effects

- on nucleon-nucleon elastic cross section with collective flows and nuclear stopping, *Phys. Lett. B.* **828**, 137019 (2022). doi: 10.1016/j.physletb.2022.137019.
347. A. Hombach, W. Cassing, S. Teis, and U. Mosel, Analysis of flow effects in relativistic heavy ion collisions within the CBUU approach, *Eur. Phys. J. A.* **5**, 157–172 (1999). doi: 10.1007/s100500050272.
348. J. Mohs, M. Ege, H. Elfner, and M. Mayer, Collective flow at SIS energies within a hadronic transport approach: Influence of light nuclei formation and equation of state, *Phys. Rev. C.* **105**(3), 034906 (2022). doi: 10.1103/PhysRevC.105.034906.
349. P. Danielewicz and G. F. Bertsch, Production of deuterons and pions in a transport model of energetic heavy ion reactions, *Nucl. Phys. A.* **533**, 712–748 (1991). doi: 10.1016/0375-9474(91)90541-D.
350. Q. Li, Y. Wang, X. Wang, C. Shen, and M. Bleicher, Influence of clustering and hadron potentials on the rapidity distribution of protons from the UrQMD model (7, 2015).
351. N. Ikeno, A. Ono, Y. Nara, and A. Ohnishi, Probing neutron-proton dynamics by pions, *Phys. Rev. C.* **93**(4), 044612 (2016). doi: 10.1103/PhysRevC.93.044612. [Erratum: *Phys.Rev.C* 97, 069902 (2018)].
352. D. Oliinychenko, L.-G. Pang, H. Elfner, and V. Koch, Microscopic study of deuteron production in PbPb collisions at $\sqrt{s} = 2.76\text{TeV}$ via hydrodynamics and a hadronic afterburner, *Phys. Rev. C.* **99**(4), 044907 (2019). doi: 10.1103/PhysRevC.99.044907.
353. A. Ono, Dynamics of clusters and fragments in heavy-ion collisions, *Prog. Part. Nucl. Phys.* **105**, 139–179 (2019). doi: 10.1016/j.pnpnp.2018.11.001.
354. J. Staudenmaier, D. Oliinychenko, J. M. Torres-Rincon, and H. Elfner, Deuteron production in relativistic heavy ion collisions via stochastic multiparticle reactions, *Phys. Rev. C.* **104**(3), 034908 (2021). doi: 10.1103/PhysRevC.104.034908.
355. K.-J. Sun, L.-W. Chen, C. M. Ko, and Z. Xu, Probing QCD critical fluctuations from light nuclei production in relativistic heavy-ion collisions, *Phys. Lett. B.* **774**, 103–107 (2017). doi: 10.1016/j.physletb.2017.09.056.
356. K.-J. Sun, L.-W. Chen, C. M. Ko, J. Pu, and Z. Xu, Light nuclei production as a probe of the QCD phase diagram, *Phys. Lett. B.* **781**, 499–504 (2018). doi: 10.1016/j.physletb.2018.04.035.
357. T. Anticic et al., Centrality dependence of proton and antiproton spectra in Pb+Pb collisions at 40A GeV and 158A GeV measured at the CERN SPS, *Phys. Rev. C.* **83**, 014901 (2011). doi: 10.1103/PhysRevC.83.014901.
358. C. Blume, Centrality and energy dependence of proton, light fragment and hyperon production, *J. Phys. G.* **34**, S951–954 (2007). doi: 10.1088/0954-3899/34/8/S133.
359. T. Anticic et al., Production of deuterium, tritium, and He3 in central Pb + Pb collisions at 20A,30A,40A,80A , and 158A GeV at the CERN Super Proton Synchrotron, *Phys. Rev. C.* **94**(4), 044906 (2016). doi: 10.1103/PhysRevC.94.044906.
360. M. Abdulhamid et al., Beam Energy Dependence of Triton Production and

- Yield Ratio ($N_t \times N_p / N_d^2$) in Au+Au Collisions at RHIC, *Phys. Rev. Lett.* **130**, 202301 (2023). doi: 10.1103/PhysRevLett.130.202301.
361. Production of Protons and Light Nuclei in Au+Au Collisions at $\sqrt{s_{NN}} = 3$ GeV with the STAR Detector (11, 2023).
362. K.-J. Sun and C. M. Ko, Light nuclei production in a multiphase transport model for relativistic heavy ion collisions, *Phys. Rev. C.* **103**(6), 064909 (2021). doi: 10.1103/PhysRevC.103.064909.
363. P. Hillmann, K. Käfer, J. Steinheimer, V. Vovchenko, and M. Bleicher, Coalescence, the thermal model and multi-fragmentation: the energy and volume dependence of light nuclei production in heavy ion collisions, *J. Phys. G.* **49**(5), 055107 (2022). doi: 10.1088/1361-6471/ac5dfc.
364. K.-J. Sun, W.-H. Zhou, L.-W. Chen, C. M. Ko, F. Li, R. Wang, and J. Xu, Spinodal Enhancement of Light Nuclei Yield Ratio in Relativistic Heavy Ion Collisions (5, 2022).
365. U. W. Heinz and B. V. Jacak, Two particle correlations in relativistic heavy ion collisions, *Ann. Rev. Nucl. Part. Sci.* **49**, 529–579 (1999). doi: 10.1146/annurev.nucl.49.1.529.
366. S. Pratt, Pion Interferometry of Quark-Gluon Plasma, *Phys. Rev. D.* **33**, 1314–1327 (1986). doi: 10.1103/PhysRevD.33.1314.
367. G. Bertsch, M. Gong, and M. Tohyama, Pion Interferometry in Ultrarelativistic Heavy Ion Collisions, *Phys. Rev. C.* **37**, 1896–1900 (1988). doi: 10.1103/PhysRevC.37.1896.
368. D. H. Rischke and M. Gyulassy, The Time delay signature of quark - gluon plasma formation in relativistic nuclear collisions, *Nucl. Phys. A.* **608**, 479–512 (1996). doi: 10.1016/0375-9474(96)00259-X.
369. G. F. Bertsch, Pion Interferometry as a Probe of the Plasma, *Nucl. Phys. A.* **498**, 173C–180C (1989). doi: 10.1016/0375-9474(89)90597-6.
370. S. Pratt, T. Csorgo, and J. Zimanyi, Detailed predictions for two pion correlations in ultrarelativistic heavy ion collisions, *Phys. Rev. C.* **42**, 2646–2652 (1990). doi: 10.1103/PhysRevC.42.2646.
371. U. W. Heinz, B. Tomasik, U. A. Wiedemann, and Y. F. Wu, Lifetimes and sizes from two particle correlation functions, *Phys. Lett. B.* **382**, 181–188 (1996). doi: 10.1016/0370-2693(96)00657-0.
372. M. A. Lisa, S. Pratt, R. Soltz, and U. Wiedemann, Femtoscopy in relativistic heavy ion collisions, *Ann. Rev. Nucl. Part. Sci.* **55**, 357–402 (2005). doi: 10.1146/annurev.nucl.55.090704.151533.
373. L. Adamczyk et al., Beam-energy-dependent two-pion interferometry and the freeze-out eccentricity of pions measured in heavy ion collisions at the STAR detector, *Phys. Rev. C.* **92**(1), 014904 (2015). doi: 10.1103/PhysRevC.92.014904.
374. F. Retiere and M. A. Lisa, Observable implications of geometrical and dynamical aspects of freeze out in heavy ion collisions, *Phys. Rev. C.* **70**, 044907 (2004). doi: 10.1103/PhysRevC.70.044907.
375. P. Li, J. Steinheimer, T. Reichert, A. Kittiratpattana, M. Bleicher, and Q. Li, Effects of a phase transition on two-pion interferometry in heavy ion

- collisions at $\sqrt{s_{NN}} = 2.4 - 7.7$ GeV, *Sci. China Phys. Mech. Astron.* **66**(3), 232011 (2023). doi: 10.1007/s11433-022-2041-8.
376. M. A. Lisa et al., Bombarding energy dependence of pi-minus interferometry at the Brookhaven AGS, *Phys. Rev. Lett.* **84**, 2798–2802 (2000). doi: 10.1103/PhysRevLett.84.2798.
377. K. Aamodt et al., Two-pion Bose-Einstein correlations in central Pb-Pb collisions at $\sqrt{s_{NN}} = 2.76$ TeV, *Phys. Lett. B.* **696**, 328–337 (2011). doi: 10.1016/j.physletb.2010.12.053.
378. J. Adamczewski-Musch et al., Identical pion intensity interferometry at $\sqrt{s_{NN}} = 2.4$ GeV: HADES collaboration, *Eur. Phys. J. A.* **56**(5), 140 (2020). doi: 10.1140/epja/s10050-020-00116-w.
379. J. Adam et al., Flow and interferometry results from Au+Au collisions at $\sqrt{s_{NN}} = 4.5$ GeV, *Phys. Rev. C.* **103**(3), 034908 (2021). doi: 10.1103/PhysRevC.103.034908.
380. S. Siejka, Geometry and Dynamics in Heavy-Ion Collisions Seen by the Femtoscopy in the STAR Experiment, *Nucl. Phys. A.* **982**, 359–362 (2019). doi: 10.1016/j.nuclphysa.2018.10.072.
381. M. Stefaniak, Proton-cluster femtoscopy with the HADES experiment (1, 2024).
382. J. Xu, Transport approaches for the description of intermediate-energy heavy-ion collisions, *Prog. Part. Nucl. Phys.* **106**, 312–359 (2019). doi: 10.1016/j.pnpnp.2019.02.009.
383. G. F. Bertsch and S. Das Gupta, A Guide to microscopic models for intermediate-energy heavy ion collisions, *Phys. Rept.* **160**, 189–233 (1988). doi: 10.1016/0370-1573(88)90170-6.
384. N. Yao, A. Sorensen, V. Dexheimer, and J. Noronha-Hostler, Structure in the speed of sound: from neutron stars to heavy-ion collisions (11, 2023).
385. M. Kardar, *Statistical Physics of Particles*. Cambridge University Press, New York (2007).
386. S. Leupold. Test particle description of transport processes for states with a continuous mass spectrum. In *International Workshop on Kadanoff-Baym Equations: Progress and Perspectives for Many-body Physics (KB 99)* (9, 1999). doi: 10.1142/9789812793812_0028.
387. T. Kodama, S. B. Duarte, K. C. Chung, R. Donangelo, and R. A. M. S. Nazareth, Causality and relativistic effects in intranuclear cascade calculations, *Phys. Rev. C.* **29**, 2146–2152 (1984). doi: 10.1103/PhysRevC.29.2146.
388. W. Cassing, Anti-baryon production in hot and dense nuclear matter, *Nucl. Phys. A.* **700**, 618–646 (2002). doi: 10.1016/S0375-9474(01)01322-7.
389. Z. Xu and C. Greiner, Thermalization of gluons in ultrarelativistic heavy ion collisions by including three-body interactions in a parton cascade, *Phys. Rev. C.* **71**, 064901 (2005). doi: 10.1103/PhysRevC.71.064901.
390. M. Colonna et al., Comparison of heavy-ion transport simulations: Mean-field dynamics in a box, *Phys. Rev. C.* **104**(2), 024603 (2021). doi: 10.1103/PhysRevC.104.024603.
391. Y.-X. Zhang et al., Comparison of heavy-ion transport simulations: Collision integral in a box, *Phys. Rev. C.* **97**(3), 034625 (2018). doi: 10.1103/

- PhysRevC.97.034625.
392. D. Oliinychenko and H. Petersen, Deviations of the Energy-Momentum Tensor from Equilibrium in the Initial State for Hydrodynamics from Transport Approaches, *Phys. Rev. C* **93**(3), 034905 (2016). doi: 10.1103/PhysRevC.93.034905.
 393. R. J. Lenk and V. R. Pandharipande, Nuclear mean field dynamics in the lattice Hamiltonian Vlasov method, *Phys. Rev. C* **39**, 2242–2249 (1989). doi: 10.1103/PhysRevC.39.2242.
 394. R. Wang, L.-W. Chen, and Z. Zhang, Nuclear collective dynamics in the lattice Hamiltonian Vlasov method, *Phys. Rev. C* **99**(4), 044609 (2019). doi: 10.1103/PhysRevC.99.044609.
 395. A. Sorensen and V. Koch, Phase transitions and critical behavior in hadronic transport with a relativistic density functional equation of state, *Phys. Rev. C* **104**(3), 034904 (2021). doi: 10.1103/PhysRevC.104.034904.
 396. A. M. Sorensen. *Density Functional Equation of State and Its Application to the Phenomenology of Heavy-Ion Collisions*. PhD thesis, UCLA, Los Angeles (main), UCLA (2021).
 397. B. Blaettel, V. Koch, and U. Mosel, Transport theoretical analysis of relativistic heavy ion collisions, *Rept. Prog. Phys.* **56**, 1–62 (1993). doi: 10.1088/0034-4885/56/1/001.
 398. S. Cheng, S. Pratt, P. Csizmadia, Y. Nara, D. Molnar, M. Gyulassy, S. E. Vance, and B. Zhang, The Effect of finite range interactions in classical transport theory, *Phys. Rev. C* **65**, 024901 (2002). doi: 10.1103/PhysRevC.65.024901.
 399. A. Ono, Antisymmetrized molecular dynamics with quantum branching processes for collisions of heavy nuclei, *Phys. Rev. C* **59**, 853–864 (1999). doi: 10.1103/PhysRevC.59.853.
 400. J. Aichelin, 'Quantum' molecular dynamics: A Dynamical microscopic n body approach to investigate fragment formation and the nuclear equation of state in heavy ion collisions, *Phys. Rept.* **202**, 233–360 (1991). doi: 10.1016/0370-1573(91)90094-3.
 401. S. Cao, T. Luo, G.-Y. Qin, and X.-N. Wang, Linearized Boltzmann transport model for jet propagation in the quark-gluon plasma: Heavy quark evolution, *Phys. Rev. C* **94**(1), 014909 (2016). doi: 10.1103/PhysRevC.94.014909.
 402. W. Ke, Y. Xu, and S. A. Bass, Linearized Boltzmann-Langevin model for heavy quark transport in hot and dense QCD matter, *Phys. Rev. C* **98**(6), 064901 (2018). doi: 10.1103/PhysRevC.98.064901.
 403. X. Yao, W. Ke, Y. Xu, S. A. Bass, and B. Müller, Coupled Boltzmann Transport Equations of Heavy Quarks and Quarkonia in Quark-Gluon Plasma, *JHEP*. **01**, 046 (2021). doi: 10.1007/JHEP01(2021)046.
 404. J. Xu, T. Song, C. M. Ko, and F. Li, Elliptic flow splitting as a probe of the QCD phase structure at finite baryon chemical potential, *Phys. Rev. Lett.* **112**, 012301 (2014). doi: 10.1103/PhysRevLett.112.012301.
 405. O. Linnyk, E. L. Bratkovskaya, and W. Cassing, Effective QCD and transport description of dilepton and photon production in heavy-ion collisions

- and elementary processes, *Prog. Part. Nucl. Phys.* **87**, 50–115 (2016). doi: 10.1016/j.pnpnp.2015.12.003.
406. T. Sjostrand, S. Mrenna, and P. Z. Skands, PYTHIA 6.4 Physics and Manual, *JHEP.* **05**, 026 (2006). doi: 10.1088/1126-6708/2006/05/026.
407. B. Andersson, G. Gustafson, and B. Soderberg, A General Model for Jet Fragmentation, *Z. Phys. C.* **20**, 317 (1983). doi: 10.1007/BF01407824.
408. B. Andersson, G. Gustafson, G. Ingelman, and T. Sjostrand, Parton Fragmentation and String Dynamics, *Phys. Rept.* **97**, 31–145 (1983). doi: 10.1016/0370-1573(83)90080-7.
409. H. Petersen, M. Bleicher, S. A. Bass, and H. Stoecker, UrQMD v2.3: Changes and Comparisons (5, 2008).
410. D. H. Rischke, S. Bernard, and J. A. Maruhn, Relativistic hydrodynamics for heavy ion collisions. 1. General aspects and expansion into vacuum, *Nucl. Phys. A.* **595**, 346–382 (1995). doi: 10.1016/0375-9474(95)00355-1.
411. D. H. Rischke, Y. Pursun, and J. A. Maruhn, Relativistic hydrodynamics for heavy ion collisions. 2. Compression of nuclear matter and the phase transition to the quark - gluon plasma, *Nucl. Phys. A.* **595**, 383–408 (1995). doi: 10.1016/0375-9474(95)00356-3. [Erratum: *Nucl.Phys.A* 596, 717–717 (1996)].
412. W. Cassing and E. L. Bratkovskaya, Parton-Hadron-String Dynamics: an off-shell transport approach for relativistic energies, *Nucl. Phys. A.* **831**, 215–242 (2009). doi: 10.1016/j.nuclphysa.2009.09.007.
413. E. L. Bratkovskaya, W. Cassing, V. P. Konchakovski, and O. Linnyk, Parton-Hadron-String Dynamics at Relativistic Collider Energies, *Nucl. Phys. A.* **856**, 162–182 (2011). doi: 10.1016/j.nuclphysa.2011.03.003.
414. P. Moreau, O. Soloveva, L. Oliva, T. Song, W. Cassing, and E. Bratkovskaya, Exploring the partonic phase at finite chemical potential within an extended off-shell transport approach, *Phys. Rev. C.* **100**(1), 014911 (2019). doi: 10.1103/PhysRevC.100.014911.
415. W. Cassing and S. Juchem, Semiclassical transport of hadrons with dynamical spectral functions in A + A collisions at SIS / AGS energies, *Nucl. Phys. A.* **672**, 417–445 (2000). doi: 10.1016/S0375-9474(00)00050-6.
416. W. Cassing and S. Juchem, Semiclassical transport of particles with dynamical spectral functions, *Nucl. Phys. A.* **665**, 377–400 (2000). doi: 10.1016/S0375-9474(99)00393-0.
417. B. Nilsson-Almqvist and E. Stenlund, Interactions Between Hadrons and Nuclei: The Lund Monte Carlo, Fritiof Version 1.6, *Comput. Phys. Commun.* **43**, 387 (1987). doi: 10.1016/0010-4655(87)90056-7.
418. B. Andersson, G. Gustafson, and H. Pi, The FRITIOF model for very high-energy hadronic collisions, *Z. Phys. C.* **57**, 485–494 (1993). doi: 10.1007/BF01474343.
419. M. Isse, A. Ohnishi, N. Otuka, P. K. Sahu, and Y. Nara, Mean-field effects on collective flows in high-energy heavy-ion collisions from AGS to SPS energies, *Phys. Rev. C.* **72**, 064908 (2005). doi: 10.1103/PhysRevC.72.064908.
420. X.-N. Wang and M. Gyulassy, HIJING: A Monte Carlo model for multiple jet production in p p, p A and A A collisions, *Phys. Rev. D.* **44**, 3501–3516

- (1991). doi: 10.1103/PhysRevD.44.3501.
421. X.-N. Wang, pQCD based approach to parton production and equilibration in high-energy nuclear collisions, *Phys. Rept.* **280**, 287–371 (1997). doi: 10.1016/S0370-1573(96)00022-1.
 422. M. Gyulassy and X.-N. Wang, HIJING 1.0: A Monte Carlo program for parton and particle production in high-energy hadronic and nuclear collisions, *Comput. Phys. Commun.* **83**, 307 (1994). doi: 10.1016/0010-4655(94)90057-4.
 423. T. Sjostrand, High-energy physics event generation with PYTHIA 5.7 and JETSET 7.4, *Comput. Phys. Commun.* **82**, 74–90 (1994). doi: 10.1016/0010-4655(94)90132-5.
 424. B. Zhang, ZPC 1.0.1: A Parton cascade for ultrarelativistic heavy ion collisions, *Comput. Phys. Commun.* **109**, 193–206 (1998). doi: 10.1016/S0010-4655(98)00010-1.
 425. Z.-w. Lin and C. M. Ko, Partonic effects on the elliptic flow at RHIC, *Phys. Rev. C* **65**, 034904 (2002). doi: 10.1103/PhysRevC.65.034904.
 426. Z.-w. Lin, C. M. Ko, and S. Pal, Partonic effects on pion interferometry at RHIC, *Phys. Rev. Lett.* **89**, 152301 (2002). doi: 10.1103/PhysRevLett.89.152301.
 427. Z.-w. Lin and C. M. Ko, Kaon interferometry at RHIC from AMPT model, *J. Phys. G* **30**, S263–S270 (2004). doi: 10.1088/0954-3899/30/1/031.
 428. B.-A. Li and C. M. Ko, Formation of superdense hadronic matter in high-energy heavy ion collisions, *Phys. Rev. C* **52**, 2037–2063 (1995). doi: 10.1103/PhysRevC.52.2037.
 429. B. Li, A. T. Sustich, B. Zhang, and C. M. Ko, Studies of superdense hadronic matter in a relativistic transport model, *Int. J. Mod. Phys. E* **10**, 267–352 (2001). doi: 10.1142/S0218301301000575.
 430. C. M. Ko, T. Song, F. Li, V. Greco, and S. Plumari, Partonic mean-field effects on matter and antimatter elliptic flows, *Nucl. Phys. A* **928**, 234–246 (2014). doi: 10.1016/j.nuclphysa.2014.05.016.
 431. J. Xu, L.-W. Chen, C. M. Ko, and Z.-W. Lin, Effects of hadronic potentials on elliptic flows in relativistic heavy ion collisions, *Phys. Rev. C* **85**, 041901 (2012). doi: 10.1103/PhysRevC.85.041901.
 432. O. Buss, T. Gaitanos, K. Gallmeister, H. van Hees, M. Kaskulov, O. Lalakulich, A. B. Larionov, T. Leitner, J. Weil, and U. Mosel, Transport-theoretical Description of Nuclear Reactions, *Phys. Rept.* **512**, 1–124 (2012). doi: 10.1016/j.physrep.2011.12.001.
 433. A. Schäfer, J. M. Torres-Rincon, J. Rothermel, N. Ehlert, C. Gale, and H. Elfner, Benchmarking a nonequilibrium approach to photon emission in relativistic heavy-ion collisions, *Phys. Rev. D* **99**(11), 114021 (2019). doi: 10.1103/PhysRevD.99.114021.
 434. J. Staudenmaier, J. Weil, V. Steinberg, S. Endres, and H. Petersen, Dilepton production and resonance properties within a new hadronic transport approach in the context of the GSI-HADES experimental data, *Phys. Rev. C* **98**(5), 054908 (2018). doi: 10.1103/PhysRevC.98.054908.
 435. R. Hirayama, Z. Paulínyová, H. Elfner. *A dynamically initialized hybrid ap-*

- proach with varying equations of state. https://indico.cern.ch/event/1043736/contributions/5363945/attachments/2690904/4669564/Poster_IS23_Hirayama.pdf Poster contribution to Initial Stages 2023, accessed: 2024-01-31.
436. R. Hirayama, Z. Paulínyová, I. Karpenko, H. Elfner, in preparation.
 437. M. Dutra, O. Lourenco, J. S. Sa Martins, A. Delfino, J. R. Stone, and P. D. Stevenson, Skyrme Interaction and Nuclear Matter Constraints, *Phys. Rev. C* **85**, 035201 (2012). doi: 10.1103/PhysRevC.85.035201.
 438. Y. B. Zel'dovich, The equation of state at ultrahigh densities and its relativistic limitations, *Zh. Eksp. Teor. Fiz.* **41**, 1609–1615 (1961).
 439. C. Gale, G. Bertsch, and S. Das Gupta, Heavy-ion collision theory with momentum-dependent interactions, *Phys. Rev. C* **35**, 1666–1671 (1987). doi: 10.1103/PhysRevC.35.1666.
 440. G. M. Welke, M. Prakash, T. T. S. Kuo, S. Das Gupta, and C. Gale, Azimuthal distributions in heavy ion collisions and the nuclear equation of state, *Phys. Rev. C* **38**, 2101–2107 (1988). doi: 10.1103/PhysRevC.38.2101.
 441. E. D. Cooper, B. C. Clark, R. Kozack, S. Shim, S. Hama, J. I. Johansson, H. S. Sherif, R. L. Mercer, and B. D. Serot, Global Optical Potentials for Elastic $P+^{40}\text{Ca}$ Scattering Using the Dirac Equation, *Phys. Rev. C* **36**, 2170–2172 (1987). doi: 10.1103/PhysRevC.36.2170.
 442. S. Hama, B. C. Clark, E. D. Cooper, H. S. Sherif, and R. L. Mercer, Global Dirac optical potentials for elastic proton scattering from heavy nuclei, *Phys. Rev. C* **41**, 2737–2755 (1990). doi: 10.1103/PhysRevC.41.2737.
 443. W. Botermans and R. Malfliet, Quantum transport theory of nuclear matter, *Phys. Rept.* **198**, 115–194 (1990). doi: 10.1016/0370-1573(90)90174-Z.
 444. K. Weber, B. Blaettel, W. Cassing, H. C. Doenges, A. Lang, T. Maruyama, and U. Mosel, Relativistic potentials for a counterstreaming nuclear matter scenario with a covariant momentum dependent interaction, *Nucl. Phys. A* **552**, 571–590 (1993). doi: 10.1016/0375-9474(93)90286-7.
 445. G. Baym and S. A. Chin, Landau Theory of Relativistic Fermi Liquids, *Nucl. Phys. A* **262**, 527–538 (1976). doi: 10.1016/0375-9474(76)90513-3.
 446. P. Papazoglou, D. Zschesche, S. Schramm, J. Schaffner-Bielich, H. Stoecker, and W. Greiner, Nuclei in a chiral SU(3) model, *Phys. Rev. C* **59**, 411–427 (1999). doi: 10.1103/PhysRevC.59.411.
 447. J. Steinheimer, S. Schramm, and H. Stoecker, An Effective chiral Hadron-Quark Equation of State, *J. Phys. G* **38**, 035001 (2011). doi: 10.1088/0954-3899/38/3/035001.
 448. A. Motornenko, J. Steinheimer, V. Vovchenko, S. Schramm, and H. Stoecker, Equation of state for hot QCD and compact stars from a mean field approach, *Phys. Rev. C* **101**(3), 034904 (2020). doi: 10.1103/PhysRevC.101.034904.
 449. A. Motornenko, S. Pal, A. Bhattacharyya, J. Steinheimer, and H. Stoecker, Repulsive properties of hadrons in lattice QCD data and neutron stars, *Phys. Rev. C* **103**, 054908 (2021). doi: 10.1103/PhysRevC.103.054908.
 450. P. Danielewicz, P. B. Gossiaux, and R. A. Lacey, Hadronic transport model with a phase transition, *Fundam. Theor. Phys.* **95**, 69–84 (1999).

451. B. A. Brown *et al.* *Motivations for Early High-Profile FRIB Experiments in preparation.*
452. A. Lovato *et al.*, Long Range Plan: Dense matter theory for heavy-ion collisions and neutron stars (11, 2022).
453. D. Almaalol *et al.*, QCD Phase Structure and Interactions at High Baryon Density: Continuation of BES Physics Program with CBM at FAIR (9, 2022).
454. M. Baldo and G. F. Burgio, The nuclear symmetry energy, *Prog. Part. Nucl. Phys.* **91**, 203–258 (2016). doi: 10.1016/j.pnpnp.2016.06.006.
455. M. S. Abdallah *et al.*, Disappearance of partonic collectivity in sNN=3GeV Au+Au collisions at RHIC, *Phys. Lett. B.* **827**, 137003 (2022). doi: 10.1016/j.physletb.2022.137003.
456. C. Pinkenburg *et al.*, Elliptic flow: Transition from out-of-plane to in-plane emission in Au + Au collisions, *Phys. Rev. Lett.* **83**, 1295–1298 (1999). doi: 10.1103/PhysRevLett.83.1295.
457. H. Liu *et al.*, Sideward flow in Au + Au collisions between 2-A-GeV and 8-A-GeV, *Phys. Rev. Lett.* **84**, 5488–5492 (2000). doi: 10.1103/PhysRevLett.84.5488.
458. P. Chung *et al.*, Differential elliptic flow in 2-A-GeV - 6-A-GeV Au+Au collisions: A New constraint for the nuclear equation of state, *Phys. Rev. C.* **66**, 021901 (2002). doi: 10.1103/PhysRevC.66.021901.
459. J. L. Klay *et al.*, Longitudinal flow from 2-A-GeV to 8-A-GeV Au+Au collisions at the Brookhaven AGS, *Phys. Rev. Lett.* **88**, 102301 (2002). doi: 10.1103/PhysRevLett.88.102301.
460. L. Ahle *et al.*, Proton and deuteron production in Au + Au reactions at 11.6/A-GeV/c, *Phys. Rev. C.* **60**, 064901 (1999). doi: 10.1103/PhysRevC.60.064901.
461. C. Alt *et al.*, Energy and centrality dependence of anti-p and p production and the anti-Lambda/anti-p ratio in Pb+Pb collisions between 20/A-GeV and 158/A-GeV, *Phys. Rev. C.* **73**, 044910 (2006). doi: 10.1103/PhysRevC.73.044910.
462. L. Adamczyk *et al.*, Bulk Properties of the Medium Produced in Relativistic Heavy-Ion Collisions from the Beam Energy Scan Program, *Phys. Rev. C.* **96**(4), 044904 (2017). doi: 10.1103/PhysRevC.96.044904.
463. D. Adamova *et al.*, New results from CERES, *Nucl. Phys. A.* **698**, 253–260 (2002). doi: 10.1016/S0375-9474(01)01371-9.
464. A. Andronic *et al.*, Excitation function of elliptic flow in Au+Au collisions and the nuclear matter equation of state, *Phys. Lett. B.* **612**, 173–180 (2005). doi: 10.1016/j.physletb.2005.02.060.
465. L. Adamczyk *et al.*, Inclusive charged hadron elliptic flow in Au + Au collisions at $\sqrt{s_{NN}} = 7.7 - 39$ GeV, *Phys. Rev. C.* **86**, 054908 (2012). doi: 10.1103/PhysRevC.86.054908.
466. J. Adamczewski-Musch *et al.*, Directed, Elliptic, and Higher Order Flow Harmonics of Protons, Deuterons, and Tritons in Au + Au Collisions at $\sqrt{s_{NN}} = 2.4$ GeV, *Phys. Rev. Lett.* **125**, 262301 (2020). doi: 10.1103/PhysRevLett.125.262301.

467. H. A. Gustafsson, H. H. Gutbrod, J. Harris, B. V. Jacak, K. H. Kampert, B. Kolb, A. M. Poskanzer, H. G. Ritter, and H. R. Schmidt, Energy and Multiplicity Dependence of Fragment Flow in High-energy Nuclear Collisions, *Mod. Phys. Lett. A*, **3**, 1323–1332 (1988). doi: 10.1142/S0217732388001598.
468. M. D. Partlan et al., Fragment flow in Au + Au collisions, *Phys. Rev. Lett.* **75**, 2100–2103 (1995). doi: 10.1103/PhysRevLett.75.2100.
469. J. Barrette et al., Proton and pion production relative to the reaction plane in Au + Au collisions at AGS energies, *Phys. Rev. C*, **56**, 3254–3264 (1997). doi: 10.1103/PhysRevC.56.3254.
470. W. Reisdorf et al., Systematics of azimuthal asymmetries in heavy ion collisions in the 1 A GeV regime, *Nucl. Phys. A*, **876**, 1–60 (2012). doi: 10.1016/j.nuclphysa.2011.12.006.
471. C. Hartnack, R. K. Puri, J. Aichelin, J. Konopka, S. A. Bass, H. Stoecker, and W. Greiner, Modeling the many body dynamics of heavy ion collisions: Present status and future perspective, *Eur. Phys. J. A*, **1**, 151–169 (1998). doi: 10.1007/s100500050045.
472. L. Landau and E. Lifshitz, *Statistical Physics: Volume 5*. Elsevier Science (2013).
473. A. Einstein, Theorie der opaleszenz von homogenen flüssigkeiten und flüssigkeitsgemischen in der nähe des kritischen zustandes, *Annalen der Physik*, **338**(16), 1275–1298 doi: <https://doi.org/10.1002/andp.19103381612>.
474. M. A. Stephanov, K. Rajagopal, and E. V. Shuryak, Signatures of the tricritical point in QCD, *Phys. Rev. Lett.* **81**, 4816–4819 (1998). doi: 10.1103/PhysRevLett.81.4816.
475. M. A. Stephanov, K. Rajagopal, and E. V. Shuryak, Event-by-event fluctuations in heavy ion collisions and the QCD critical point, *Phys. Rev. D*, **60**, 114028 (1999). doi: 10.1103/PhysRevD.60.114028.
476. J. I. Kapusta, B. Muller, and M. Stephanov, Relativistic Theory of Hydrodynamic Fluctuations with Applications to Heavy Ion Collisions, *Phys. Rev. C*, **85**, 054906 (2012). doi: 10.1103/PhysRevC.85.054906.
477. A. Pelissetto and E. Vicari, Critical phenomena and renormalization group theory, *Phys. Rept.* **368**, 549–727 (2002). doi: 10.1016/S0370-1573(02)00219-3.
478. M. A. Stephanov, Non-Gaussian fluctuations near the QCD critical point, *Phys. Rev. Lett.* **102**, 032301 (2009). doi: 10.1103/PhysRevLett.102.032301.
479. M. A. Stephanov, On the sign of kurtosis near the QCD critical point, *Phys. Rev. Lett.* **107**, 052301 (2011). doi: 10.1103/PhysRevLett.107.052301.
480. J. Adam et al., Nonmonotonic Energy Dependence of Net-Proton Number Fluctuations, *Phys. Rev. Lett.* **126**(9), 092301 (2021). doi: 10.1103/PhysRevLett.126.092301.
481. M. Abdallah et al., Cumulants and correlation functions of net-proton, proton, and antiproton multiplicity distributions in Au+Au collisions at energies available at the BNL Relativistic Heavy Ion Collider, *Phys. Rev. C*, **104**(2), 024902 (2021). doi: 10.1103/PhysRevC.104.024902.

482. M. S. Abdallah et al., Measurements of Proton High Order Cumulants in $\sqrt{s_{NN}} = 3$ GeV Au+Au Collisions and Implications for the QCD Critical Point, *Phys. Rev. Lett.* **128**(20), 202303 (2022). doi: 10.1103/PhysRevLett.128.202303.
483. L. Landau and E. Lifshitz, *Statistical Physics, Part 2*. vol. 9, *Course of Theoretical Physics*, Elsevier Science (2013).
484. X. An, G. Basar, M. Stephanov, and H.-U. Yee, Relativistic Hydrodynamic Fluctuations, *Phys. Rev. C* **100**(2), 024910 (2019). doi: 10.1103/PhysRevC.100.024910.
485. M. Singh, C. Shen, S. McDonald, S. Jeon, and C. Gale, Hydrodynamic Fluctuations in Relativistic Heavy-Ion Collisions, *Nucl. Phys. A* **982**, 319–322 (2019). doi: 10.1016/j.nuclphysa.2018.10.061.
486. C. Chattopadhyay, J. Ott, T. Schaefer, and V. Skokov, Dynamic scaling of order parameter fluctuations in model B, *Phys. Rev. D* **108**(7), 074004 (2023). doi: 10.1103/PhysRevD.108.074004.
487. Y. Akamatsu, A. Mazeliauskas, and D. Teaney, Kinetic regime of hydrodynamic fluctuations and long time tails for a Bjorken expansion, *Phys. Rev. C* **95**, 014909 (Jan, 2017). doi: 10.1103/PhysRevC.95.014909.
488. Y. Akamatsu, A. Mazeliauskas, and D. Teaney, Bulk viscosity from hydrodynamic fluctuations with relativistic hydrokinetic theory, *Phys. Rev. C* **97**, 024902 (Feb, 2018). doi: 10.1103/PhysRevC.97.024902.
489. M. Martinez and T. Schaefer, Stochastic hydrodynamics and long time tails of an expanding conformal charged fluid (2018).
490. M. Stephanov and Y. Yin, Hydrodynamics with parametric slowing down and fluctuations near the critical point, *Phys. Rev. D* **98**(3), 036006 (2018). doi: 10.1103/PhysRevD.98.036006.
491. X. An, G. Başar, M. Stephanov, and H.-U. Yee, Fluctuation dynamics in a relativistic fluid with a critical point, *Phys. Rev. C* **102**(3), 034901 (2020). doi: 10.1103/PhysRevC.102.034901.
492. X. An, G. Başar, M. Stephanov, and H.-U. Yee, Evolution of Non-Gaussian Hydrodynamic Fluctuations, *Phys. Rev. Lett.* **127**(7), 072301 (2021). doi: 10.1103/PhysRevLett.127.072301.
493. X. An, G. Basar, M. Stephanov, and H.-U. Yee, Non-Gaussian fluctuation dynamics in relativistic fluids, *Phys. Rev. C* **108**(3), 034910 (2023). doi: 10.1103/PhysRevC.108.034910.
494. C. Athanasiou, K. Rajagopal, and M. Stephanov, Using Higher Moments of Fluctuations and their Ratios in the Search for the QCD Critical Point, *Phys. Rev. D* **82**, 074008 (2010). doi: 10.1103/PhysRevD.82.074008.
495. B. Ling, T. Springer, and M. Stephanov, Hydrodynamics of charge fluctuations and balance functions, *Phys. Rev. C* **89**(6), 064901 (2014). doi: 10.1103/PhysRevC.89.064901.
496. M. S. Pradeep and M. Stephanov, Maximum Entropy Freeze-Out of Hydrodynamic Fluctuations, *Phys. Rev. Lett.* **130**(16), 162301 (2023). doi: 10.1103/PhysRevLett.130.162301.
497. M. Pradeep, K. Rajagopal, M. Stephanov, and Y. Yin, Freezing out fluctuations in Hydro+ near the QCD critical point, *Phys. Rev. D* **106**(3),

036017 (2022). doi: 10.1103/PhysRevD.106.036017.

498. NSAC. A new era of discovery: The 2023 long range plan for nuclear science. <https://nuclearsciencefuture.org/wp-content/uploads/2023/11/NSAC-LRP-2023-v1.3.pdf> (2023).